The Dissertation Committee for Kin Wai Lei certifies that this is the approved version of the following dissertation:

Template-Assembly and Spectroscopic Study of Colloidal Quantum Dot Molecules

Committee:

Donglei Fan, Supervisor

XiaoYang Zhu, Co-Supervisor

Brian Korgel

Xiaoqin (Elaine) Li

Charles B. Mullins

Template-Assembly and Spectroscopic Study of Colloidal Quantum Dot Molecules

by

Kin Wai Lei, B.S.

Dissertation

Presented to the Faculty of the Graduate School of

The University of Texas at Austin

in Partial Fulfillment

of the Requirements

for the Degree of

Doctor of Philosophy

The University of Texas at Austin

May 2014

Dedication

This work is dedicated to my Mom, Dad, my fiancée, the rest of my family, and my larger church family.

Acknowledgements

I would like to thank my current supervisor Dr. Donglei Fan for taking me into her lab when I was in need to find a new lab at UT. She has shown a lot of grace and support to me throughout the past year and a half, and I know she has really gone out of her way to ensure that I have funding and can graduate on time. She also has been such a great mentor in research and has a lot of new research ideas. I also want to acknowledge all my colleagues in Dr. Fan's lab: Chao, Jianhe, Jing, Kwanoh, and Xiaobin. They all are very easy to work with and talk to and I particularly appreciate the supportive and personable work environment created because of that. I want to acknowledge Chao especially since we have worked together the most and he has been very willing to help me out in showing me where things were in lab when I first arrived and offering help and suggestions along the way.

I also would like to thank my co-supervisor, Dr. XiaoYang Zhu. He has shown me a lot of patience and grace as my supervisor for the first three and a half year of my graduate career, especially during the early days when I was still adjusting to the research environment and how to work efficiently with others. He has such passion and creativity in research that I rarely see in most people I have worked with. Even after his departure from UT, he continues to be mindful of my research progress and graduation. It was a pleasure to work with my colleagues from Dr. Zhu's lab. Abe had offered me a lot of help and advice as a post doc working on similar projects. Askat was my office mate

when it was just the two of us there in our office for a while. I really enjoyed the time we had talking about research and other things in life. Raluca had offered me good research suggestions and was willing to offer help. It was a pleasure to work with my labmates and a lot of us entered UT the same year: Cory, John, Josh, and Adam.

I am very grateful to the faculty members who have agreed to serve on my dissertation committee: Dr. Brian Korgel, Dr. Elaine Li, and Dr. Charles B. Mullins. Thank you for your helpful research advice during the preliminary oral exam and your patience in working with me to find a final defense time that works for everyone.

My family has been such a source of support throughout my graduate career, and my parents are the ones that make it possible in the first place by moving to the U.S. I also want to thank all my friends and my larger church family that have shown me so much support in words and actions through the ups and downs of my graduate study.

I would like to end with this proverb to acknowledge the One who has guided me throughout my time in graduate school. “Trust in the Lord with all your heart, and do not lean on your own understanding. In all your ways acknowledge him, and he will make straight your paths.” (Proverbs 3:5-6, ESV)

Template-Assembly and Spectroscopic Study of Colloidal Quantum Dot Molecules

Kin Wai Lei, Ph.D.

The University of Texas at Austin, 2014

Supervisor: Donglei Fan

Co-supervisor: XiaoYang Zhu

Block copolymer template-assembly of quantum dots and plasmonic nanostructures is developed to provide a well-controlled platform to study the electronic coupling and Förster resonance energy transfer (FRET) between quantum dots (QDs), as well as the influence of surface plasmons on energy transfer. By fine-tuning the aspect ratio of the geometric features of PS-b-PMMA copolymer template, QDs are assembled into an array of QD clusters within nanoscopic holes on the template using capillary force assembly. Coupled QD clusters, termed quantum dot molecules (QDMs), are assembled in an array to probe the local coupling within QD molecules when the native insulating ligands are exchanged with shorter ligands. From absorption measurement of 1st exciton peak position of PbSe QDMs upon ligand exchange, a larger red-shift is found for QDMs than for a close packed film of PbSe QDs with the same ligand exchange, demonstrating localized electronic coupling of these QD molecules. Template-assembly of nanoparticles is further generalized to uniformly couple QDs clusters with plasmonic nanodisks of noble metals. Using PS nanospheres as reactive ion etch mask, Au nanodisks are fabricated on CdSe/ZnS core shell QD clusters, separated by a tunable space layer of PMMA. This highly controllable surface plasmon-coupled QD system minimizes the

uncertainty in interfacial homogeneity, characterized by cross sectional scanning electron microscopy (SEM). Photoluminescence (PL) peak ratio of donor to acceptor emission and donor lifetime measurements show strong evidence of surface plasmon coupled energy transfer between donor-acceptor QDs, which depends on the position of the surface plasmon peaks as well as the separation between plasmonic structure and FRET QD clusters. The result suggests that a larger overlap of surface plasmon peak with the emission peak of acceptor leads to greater decrease in PL lifetime of donor. Donor lifetime decreases dramatically in the presence of both acceptor and surface plasmon compared to just in the presence of surface plasmon. Coupling between plasmonic nanodisks and QD clusters also decreases and results in longer donor lifetime as the thickness of PMMA separation layer increases.

Table of Contents

List of Tables

List of Figures

Chapter 1: Introduction on quantum dots and their interaction with plasmonic nanoparticles

1.1 Physical properties of quantum dots and plasmonic nanoparticles

1.1.1 Quantum dots

Semiconductor nanocrystals (NCs) have generated enormous research interest in the past decades due to their novel electronic and optical properties. The physical size of semiconductor NCs is order of magnitude larger than individual molecules but still far from size of bulk semiconductors. The electronic structure of semiconductor NCs, though distinct from either individual molecules or bulk semiconductors, bears resemblance to the discrete molecular orbital theory of individual molecule as well as the band theory of bulk semiconductors. It provides the platform to bridge our understanding of how bulk properties of materials emerged from their properties on the atomic or molecular level.[1] Semiconductor nanocrystals can be classified into two broad categories: epitaxial semiconductor nanocrystals and colloidal semiconductor nanocrystals. Epitaxial semiconductor nanocrystals are nanometer sized crystals grown on a crystalline substrate with matching crystalline structure, and typically they are made of Group III and V elements (Ga, In, P, As) that form the traditional semiconducting materials, as shown in figure 1.1B. Colloidal semiconductor nanocrystals, otherwise known as quantum dots (QDs), are nanometer-sized crystallites typically synthesized in solutions and contain some forms of surface passivation with organic or inorganic layer to stabilize these QDs

in solution. The most characterized QD systems consist of Group II (Cd, Zn) or IV (Pb) with VI elements (S, Se, Te) but QDs from IV elements (Si, Ge) have also been studied. QDs have been regarded as artificial atoms due to their discrete electronic energy levels near band edges; such electronic structure can be considered as in between the discrete energy levels of molecular orbitals and the band structures of bulk semiconductors. Figure 1.1 illustrates the typical electronic structure of molecule, semiconductor nanocrystals, and bulk semiconductors.

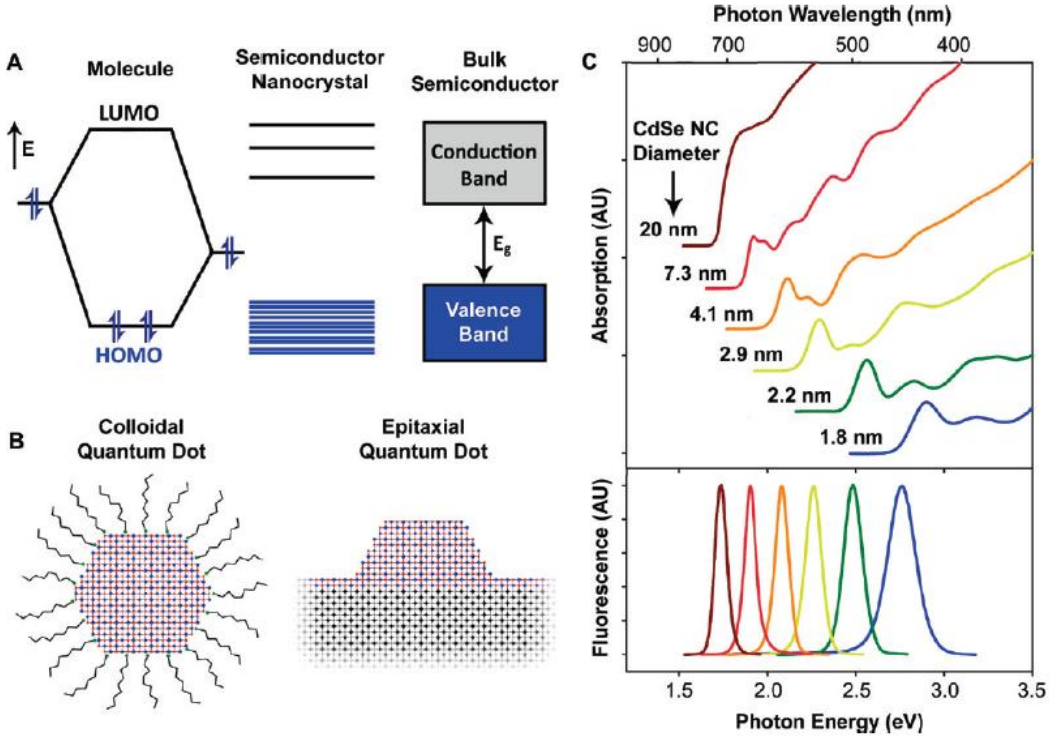

Figure 1.1 a) Electronic structure of molecule, semiconductor nanocrystals, and bulk semiconductors. b) Schematic showing the structures of colloidal quantum dots and epitaxial quantum dot. c) Absorption and fluorescence spectra demonstrating the size tunable electronic structure of CdSe nanocrystals. Reprinted with permission from ref [1]. Copyright 2009, American Chemical Society.

When a ground state electron of QDs is excited by a photon to an energy level in the conduction band and leaves a hole behind in the valence band, it forms what is called an exciton, an electrostatically bound electron-hole pair. The most dominant effect on the electronic properties of QDs is the quantum confinement of exciton wavefunction imposed by the physical size of QDs. A QD is considered to be quantum confined when the physical size of the QD is smaller than its exciton Bohr radius, a quantity that characterizes the size of the exciton wavefunction. Common size of QDs ranges from a few nanometers to tens of nanometers. The Bohr radius of QDs can be more than a hundred nm depending on the composition.[1] Quantum confinement introduces a confinement energy that widens the energy gap between the valence and conduction band. The degree of confinement is directly related to the size of QDs given the same composition of materials, which results in size-tunable electronic and optical properties for QDs. One clear demonstration of the size-tunability of QDs is changing the absorption and emission spectra of Cadmium Selenide (CdSe) QDs across the entire visible range of the electromagnetic(EM) spectrum by changing the diameter of CdSe QDs.[2] Figure 1.1C shows the absorption and fluorescence spectra for CdSe QDs ranging from 1.8nm to 20nm.

Due to its small size QDs have higher proportion of atoms on the surface than bulk materials. Therefore, the chemical environment on surface of QDs plays an important role in determining the properties of QDs. Atoms on the surface of QD are not able to satisfy their full valency compared to atoms in the core, resulting in “dangling bonds” on the surface of QDs. Dangling bonds and defects in the crystalline structure on

surface of QDs produce energy states within the energy gap between valence and conduction bands. These surface states can trap electrons or holes as they relax to their ground states and lead to reduced photoluminescence or carrier mobility.[3] To eliminate these surface states, an inorganic shell of a different material was grown over the core QD to form a core-shell QD.[4][5] Based on the size of the band gap of the core and shell materials, core-shell QDs are classified into type I or II QDs. For type I core-shell QDs, the band gap of the shell material is higher than the core material, resulting in a confinement of the excitons in the core because of the energy barrier. This core confinement increases quantum efficiency because electron-hole recombination becomes more likely as both are confined in the core. For type II core-shell QDs, the conduction band edge of the shell material has lower energy than that of the core material. An excited electron from the core is transferred to a lower energy state of the shell while the hole remains in the core. As a result, emission from the QD is red-shifted and the spatial separation of electron and hole leads to a longer recombination time.

Colloidal QDs are not stable against aggregation with each other because surface energy is reduced as a result of smaller QDs aggregating to form bigger nanoparticles. To prevent aggregation, surface of QDs are typically passivated during synthesis with long-chain organic ligand with a functional group that can bind to the surface of QDs. The long organic chains are distributed over the surface of QDs and provide the steric hindrance against aggregation. The organic layer increases the closest distance QDs can approach each other and most organic chains are insulating. Ligand exchange from a long

insulating ligand to a shorter ligand allows for stronger interaction between QDs and lowers the barrier for charge transfer between QDs.

1.1.2 Plasmonic nanoparticles

Plasmonic nanoparticles (NPs) are made of noble metals (Au, Ag) and exhibit localized surface plasmon resonance (LSPR). LSPR is the collective oscillation of free electrons in the metal NPs under the influence of an oscillating electromagnetic (EM) field.[6] The oscillating electrons also generate electromagnetic field with same frequency as incident EM field near the surface of the NPs, which constitutes an elastic scattering of incident EM field. Light can also be absorbed by metal NPs. Absorption leads to an excited electron-hole pair either through intra-band transition, e.g. conduction band, or inter-band transition e.g. between conduction band and d-bands. The extinction of light by either absorption or scattering can be described by the Mie theory.[7] For a metal nanospheres with particle radius R much larger than incident light with wavelength λ, the extinction cross section in the quasi-static and dipole limit is given by[8]:

$$C_{ext} = \frac{24\pi^2 R^3 \varepsilon_m^{3/2}}{\lambda} \frac{\varepsilon_i}{(\varepsilon_r + 2\varepsilon_m)^2 + \varepsilon_i^2}$$

where ε_r and ε_i are the real and imaginary part of the frequency-dependent dielectric function of nanospheres and ε_m are the dielectric constant of the surrounding medium. In the nanometer scale, LSPR of NPs typically is found in the optical and near IR range of the EM spectrum, depending on the shape and the composition of noble metals. However, the physical size of the metal NPs can be much smaller than the wavelength of their

LSPR. This property of LSPR from NPs breaks the diffraction limit of light by localizing EM field down to the size of the metal NPs, which could be as small as just a few nanometers. EM field not only can be localized but concentrated on certain area of the NPs, particularly region with small surface area. This effect of concentrating a portion of the incident EM wave by the LSPR on the surface of plasmonic NPs is called field enhancement

In addition to the localized surface plasmons, the oscillation of free electrons of noble metal can also be travelling through the medium, which is known as the propagating surface plasmon resonance (SPR). It occurs in medium like nanowire or film where SPR can travel along the length of the wire or can propagate across the surface of the film. A large variety of size and shape of plasmonic NPs have been made and studied[9][10][11] to gain a better understanding of how size and shape affect surface plasmon.

1.2 Applications of quantum dots and plasmonic nanoparticles

1.2.1 Biological applications

Because of the size tunable band gap and high quantum yield of QDs, the electronic and optical properties of QDs have found many applications in bio-labeling and biosensing. As a label, QDs can reveal the location of a specific biological species that has been tagged under a fluorescence microscope[12], or conduct *in vivo* imaging of targeted cancerous cells.[13] QDs have advantages over other fluorophores in having higher photostability and the surface of QDs can readily be functionalized with biological

moieties like DNAs or peptides. QDs as a biosensor can also be used to detect binding events[14][15] or enzyme activity with proteins[16] in biological systems via Förster resonance energy transfer (FRET). The idea is to tag the two species involved, one with donor and one with acceptor fluorophores. As a biological event like the conjugation of biotin-streptavidin happens, the attached donor and acceptor will be brought in close proximity and excitation can be transferred from donor to acceptor nonradiatively, quenching emission from the donor QDs. Evidence of FRET can be measured using both intensity and lifetime, as FRET will lead to a shorter donor lifetime.

Plasmonic NPs have also found a large variety of applications in labeling, detection and photothermal therapy. The scattering of white light from surface plasmon of metal NPs can be strong enough to serve as a biomarker that does not suffer from photobleaching in dark field illumination.[17] Metal NPs with different surface plasmon peaks will show up with different color in a dark background. Similar to QDs, plasmonic NPs can also be functionalized with DNA, antibody, or enzymes to specifically target certain biological species.[18] LSPR of Au NPs can be converted to heat via electron-electron and electron-phonon couplings. Small Au NPs functionalized with antibodies are used to target cancer cell and provide local heating to specifically destroy cancer cell.[19] The Au NPs are exposed to illumination with strong spectral overlap with the absorption of the Au NPs, such as a laser source. Other shapes of Au NPs like nanorods have been employed to tune the resonance frequency maximum to the Near IR region, which is the more transparent spectral region for biological tissues than visible light. The spectral position of surface plasmon peak of metal NPs are dependent on the dielectric

environment surrounding the metal NPs.[20] A change in the dielectric environment causes a spectral shift of the surface plasmon resonance. The binding of different biological molecules on surface of metal NPs functionalized with binding sites causes a change in the dielectric environment and produce a shift of the surface plasmon peak, making metal NPs a sensitive biosensor particularly in dark field illumination.

Local field enhancement from metal NPs has revolutionized Raman scattering measurement, leading to a widely popular spectroscopic technique known as Surface Enhanced Raman Scattering (SERS).[21][22] SERS relies on the presence of hotspots near surface of metal NPs, which are areas with concentrated electric (E) field as a result of surface plasmon resonance. Usually hotspots are created in confined regions of metal NPs, such as the tip of triangles, rods, or the junction of dimers. Both the incident light and Raman signals are amplified by E field from surface plasmon, and single molecule detection has been demonstrated at the junction of Ag NPs.[23][24]

1.2.2 Light harvesting and optoelectronic applications

The brightness and size tunability of QD emission makes QDs a prominent candidate as light emitting diodes (LEDs). QDs can be employed as the direct light emitting medium or supplement existing LED technology. Currently, a common way to make white LEDs is to combine blue Indium Gallium Nitride (InGaN) LEDs with a yellow phosphor. It has been demonstrated that red and green QDs can be combined with the blue LED to form white QD-LED[25].

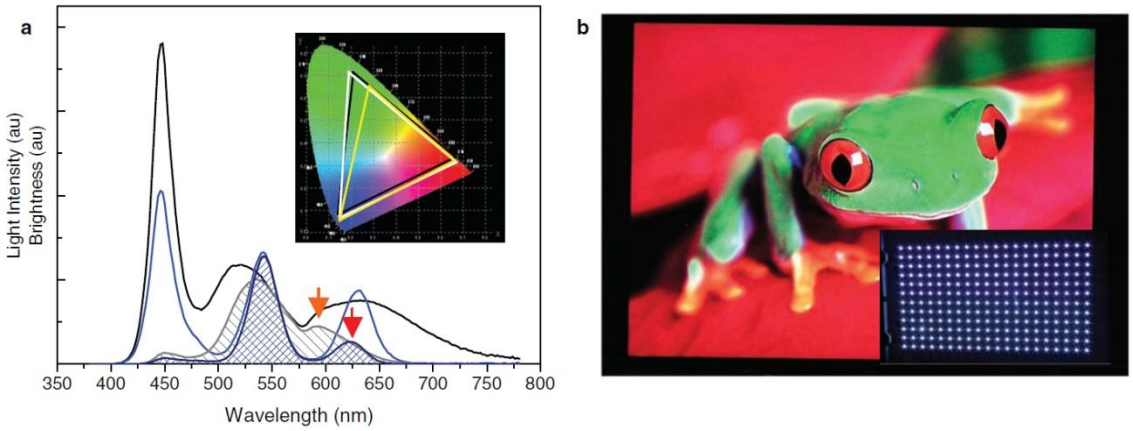

Figure 1.2 a) Light intensity (solid) and brightness (hatched) of phosphor-LED (grey) and QD-LED (blue). Inset: color triangles of phosphor-LED (yellow) and QD-LED (white). b) display image of a 46inch LCD TV with white QD-LED backlights (inset). Reprinted with permission from ref [25]. Copyright 2010, John Wiley and Sons.

The advantages of using QDs over phosphor are the stability and narrow spectral emission of QDs compared with phosphor. Figure 1.2a shows the narrower red, green, and blue emission intensity from QD-LED (blue solid line) comparing with the broader intensity peaks from phosphor-LED (black solid line). The white QD-LED can be incorporated into existing LCD display to produce a broader color gamut than phosphor based LEDs, which comes from the narrow spectral emission of red and green QDs. Figure 1.2b demonstrates the incorporation of white QD-LED as backlight with existing LCD display technology. Complete QD-based electroluminescence is also explored in the area of display technology to generate the three primary colors, red, green, and blue, for a complete QD based color display[26]. Instead of using the blue light from solid state LEDs as the source of excitation for red and green QDs, all three of the colors would be generated by QDs with the corresponding emission as electrons and holes are injected

and radiatively recombine. Such structure holds the promise to fabricate displays with higher color purity, higher stability on flat as well as on flexible substrate. Dense films of QDs have been used as the active material in field effect transistor (FET) to study and optimize carrier mobilities within this QD solid film[27][28], which is vital for the development of total QD-based LED.

Several properties of QDs make them a promising material for next-generation photovoltaics, in particular to break the Shockley-Queisser limit[29] for single junction solar cell. This theoretical limit on efficiency of single p-n junction solar cell is about 30% at band gap of 1.1eV. QDs have been employed in photovoltaics as QD-sensitized solar cell with TiO_2 nanoparticles, hybrid solar cell involving QDs and organic semiconductor, or semiconductor heterojunction solar cell. QDs have high absorption cross section, a wide and tunable absorption range, and greater resistance to photodegradation than organic molecules[30]. In addition, utilizing higher energy photons from the solar spectrum, multiple exctions can be generated from a single photon to boost power conversion efficiency of QD solar cell. Multiple exciton generation[31] (MEG) is an Auger-type process that converts an exciton with higher energy into two or more excitons with lower energy, thus boosting the power conversion efficiency of the solar cell. Figure 1.3 shows the relaxation pathways of a highly excited electron through a) generation of phonons, or lattice vibration of QD and b) generation of another exciton. The exciton multiplication process is also known as impact ionization.

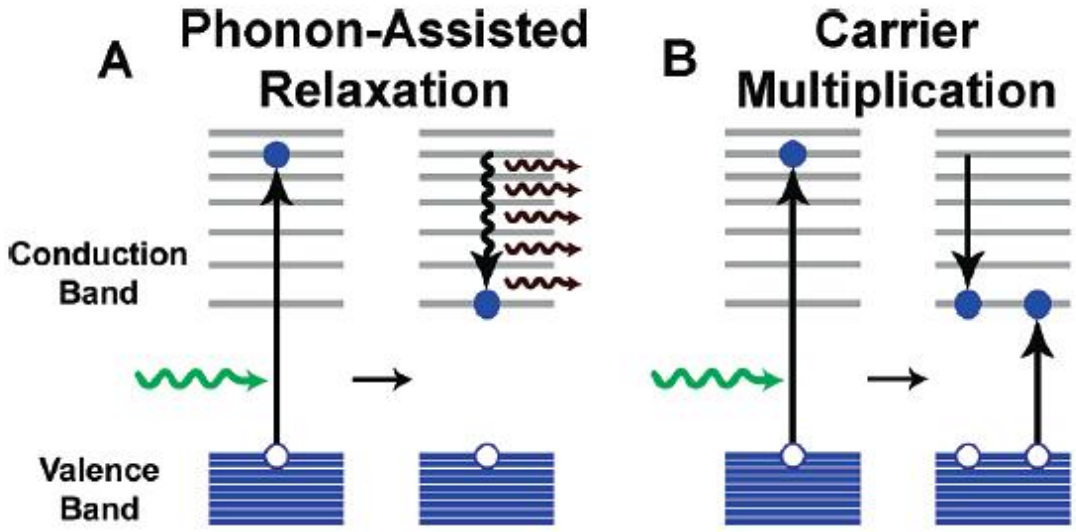

Figure 1.3 a) phonon-assisted relaxation of an excited electron. b) multiplication of exciton through an Auger-type process known as impact ionization. Reprinted with permission from ref [1]. Copyright 2009, American Chemical Society.

Without MEG, an electron excited high above the 1st exciton level will quickly thermalize and lose its energy to the QD lattice as it relaxes to a lower energy excited state. MEG is a process that can capture this energy that would otherwise be lost. Combining plasmonic nanoparticles with QDs in a solar cell, it is possible to increase light absorption through the surface plasmons of metal nanoparticles. The local field enhancement effect can also help direct energy to QDs when they are placed near the metal nanoparticles. Being a conductor, metal nanoparticles can also play a direct role in charge extraction and transport. All these properties make QDs and plasmonic nanoparticles attractive materials for fabricating solar cell.

1.3 Synthesis of colloidal quantum dots and plasmonic nanoparticles

1.3.1 Colloidal quantum dots

Synthesis of colloidal QDs generally follows the kinetics of rapid nucleation, then slow and uniform growth in a high temperature solution.[32] Nucleation is controlled such that it only happens once in the beginning stage, so all the QD nuclei would experience similar growth rate as reagents are added. Nucleation can be initiated when reagents are rapidly injected into a hot coordinating solvent containing the organometallic precursor and stabilizing ligand. The solution becomes supersaturated with reagents and nucleation is initiated, which rapidly decreases the concentration of reagents below the critical concentration for nucleation. The QD nuclei are allowed to grow as reagents are consumed but no further nucleation event would happen. Solution is cooled to stop QD growth when the desired growth time is reached. A solvent miscible with the QD solution but interacts unfavorably with the ligand-capped QDs is added to induce flocculation of QDs, and the resulting QD precipitate is collected by centrifugation and decanting of the solution. The collected QD solid is redispersed in solution, and the precipitation and re-dispersion process is repeated a few times to remove unreacted reagents and purify the sample. This hot injection method has become the standard method to synthesize QD with narrow size distribution. An alternative synthetic approach involves properly controlling the temperature of the solution to induce nucleation and to control growth of QD nuclei. All the reagents are mixed in a solution at temperature low enough such that there is no appreciable reaction. The solution is then heated up to reach critical reagent

concentrations for nucleation, and the temperature is set such that the rate at which reagents are consumed is less than or equal to the rate at which the nuclei grows. This prevents new nuclei from forming when most of the reagents consumed are directed towards the growth of existing nuclei. A phenomenon known as Ostwald ripening also affects the growth process of QDs. Ostwald ripening is the dissolution of smaller QDs and their re-deposition to larger QDs. The process is driven by an overall decrease of surface energy as smaller QDs have higher surface energy. The average QD size increases while the number of QDs decreases during Ostwald ripening.

The growth of QD size is primarily controlled by the growth time, but other factors like growth temperature, size and affinity of stabilizing ligand to QDs, and ratio of reagents to stabilizing ligand. A higher ligand to reagent ratio produces nuclei with smaller diameter and a smaller averaged QD size. Ligands with strong affinity to QD surface slow down the deposition of reagents on QD surface, and thus lower the growth rate of QDs. For example, ligands with carboxylate group like oleate (OA) have higher affinity to Pb or Cd atoms on QD surface then ligands with alkylphosphine group like trioctylphosphine (TOP). The steric hindrance imposed by the size of ligands would also inhibit addition of reagents to QD surface, i.e. trioctylphosphine with the bulkier octyl groups provides more steric hindrance than the smaller butyl groups on tributylphosphine.

1.3.2 Plasmonic nanoparticles

While colloidal QDs are synthesized with bottom-up approach, plasmonic NPs can be synthesized with both bottom-up and top-down approaches. Bottom-up approaches generally provide more uniform surface and produce NPs with lower averaged size. Top-down approaches allow the fabrication of highly-ordered periodic array of NPs and the size and shape of NPs can be controlled through different lithographic masks. It is beyond the scope of this introduction to cover all the methods that have been developed, either bottom-up or top down. Only certain well-developed methods are covered to give a broad survey given the large variety of plasmonic NPs that have been developed. Common bottom up methods involve the reduction of noble metal precursors by organic reducing agent in the presence of stabilizing ligands. A classic example is the reduction of Chloroauric acid, $HAuCl_4$, by sodium citrate in boiling aqueous solution[33][34]. Usually another stabilizing agent is needed to prevent agglomeration of Au NPs but citrate ions also act as a stabilizing agent in this case. There are many other bottom-up methods developed to synthesize Au NPs with different surface ligands. The Brust-Schiffrin method[35] uses the strong affinity of thiol group (-SH) in alkylthiols to Au as the stabilizing agent in a bi-phasic reduction of Au precursors. Many other thiol-functionalized molecules, DNA, and polymers had been used as the stabilizing ligands. Amphiphilic systems like microemulsions, micelles, or reverse micelles, are also used to create a microenvironment to capture Au ions from the aqueous phase to form Au NPs in the organic phase[36-38]. Metal NPs can also be synthesized in

various biological systems[39] like bacteria, fungi, yeasts, algae, and viruses when they are exposed to the proper environment containing the metal precursors.

In the top-down approach, various lithographic techniques have been used to create ordered array of metal nanowires or NPs with different size and shape. Nanosphere lithography (NSL)[21] utilizes a close packed layer of nanospheres as a lift off mask. Typically the close packed layer is formed by spin-coating on the target substrate a solution containing polystyrene (PS) nanospheres with the appropriate concentration of surfactants. The surfactant is used to improve wetting between the aqueous solution and substrate. Noble metals are then deposited on the substrate containing the nanospheres layer. The hexagonally close packed layer contains gaps between the nanospheres and metal is deposited on the substrate through these gaps while most metal is deposited on the nanospheres. The PS nanospheres are subsequently dissolved by sonication in dichloromethane (CH_2Cl_2). By using a more concentrated PS nanospheres solution, a double layer close packed film of PS nanospheres can be formed on the substrate to create a different periodic array of NPs using the same technique. PS nanospheres have also been used as an etch mask to create nanodisks[10] or nanorings[9]. Instead of a close packed film, PS nanospheres can be deposited with spacing between each other with the aid of polyelectrolyte layers. To create nanorings, PS nanospheres are first deposited, followed by metal deposition on the substrate, except for area that is in direct contact with the nanospheres. The substrate is argon ion etched and all the deposited metal is etched away except for metal on the area shadowed by PS nanospheres, forming an array of nanorings. To form nanodisks, metal is deposited on substrate first, followed by PS

spheres as argon etch mask. Only area shadowed by PS spheres remains after argon etch, forming an array of nanodisks. Figure 1.4 shows the SEM images of array of nanodisks and nanorings fabricated using PS spheres as mask.

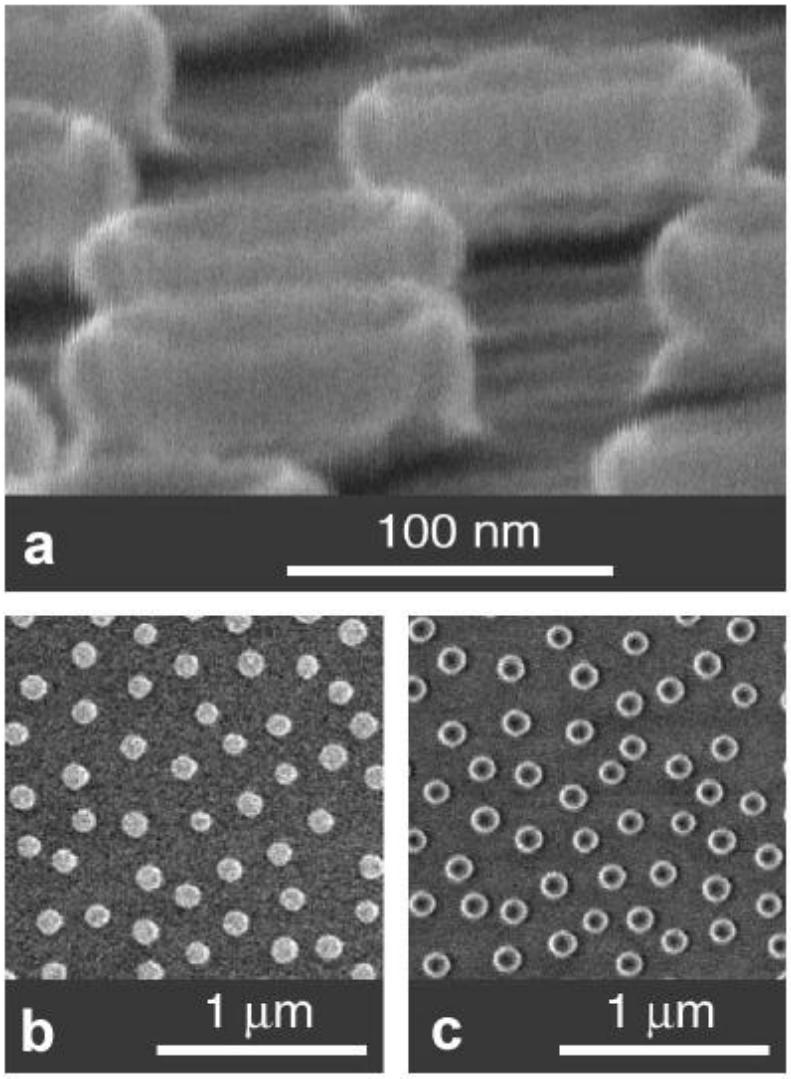

Figure 1.4 a) SEM images of gold nanorings. Top view of b) gold nanodisks and c) nanorings. Reprinted with permission from ref [9]. Copyright 2003, American Physical Society.

Template-based fabrication[40] is another general category of top down approach. Nanorods or nanowires are often electrochemically deposited within the pores of anodized aluminum oxide (AAO) template, which contains hexagonal array of hollow cylindrical pores. Using this approach, nanowires with segments containing different metals can be made. On wire lithography[41] (OWL) is a technique built upon the electrochemically deposited nanowire to create gap structure on nanowires. Sacrificial layer is deposited as a segment along the nanowire within the AAO template. The nanowires are then removed from the template and put on a substrate, after which a backing material is deposited on top side of the nanowires. The sacrificial layer is etched away to form the gap. The backing material holds the disjointed nanowire segments together with gaps size defined by thickness of sacrificial layer.

1.4 Previous work on the assembly of quantum dots and their interaction with plasmonic nanoparticles

1.4.1 Assembly of quantum dot films and superlattices

With the advancement of QD synthesis, highly monodisperse QDs can be synthesized relatively easily. Using these monodisperse QDs as building blocks, higher order nanostructure can be assembled in multiple length scale, much like the way atoms can be assembled into molecules and crystalline solids. On a flat substrate or at the air-liquid interface, close packed films of QD are formed through a combination of intrinsic attractive van der Waals force between QDs and proper balance of surface energy between QDs and the surface in contact. A common way to form a close packed QD film

is using a Langmuir-Blodgett (LB) trough.[42][43] A non-miscible organic solvent containing QDs is dispersed on the aqueous surface of the LB trough. As the organic solvent evaporates, the surfactant-capped QDs remain close to the air-water interface to minimize unfavorable interaction between the non-polar tails and the aqueous phase. A barrier is moved across the aqueous surface to apply pressure to the QDs and they are compressed into a close packed monolayer film. A substrate is mechanically dipped into the aqueous solution and the monolayer is deposited on the substrate as it is withdrawn from the aqueous surface under constant surface pressure applied by the barrier. Other commonly used methods to form QD thin film on a substrate involve spin-coating or dip-coating substrate into a QD solution with the proper concentration. Thin film of QDs is a model system to study optoelectronic properties of coupled QDs. To increase inter-QD electronic interaction, one can remove or replace the long and insulating capping molecules by shorter or conjugated ones, but this approach leads to formation of QD clusters with random size distribution and cracks within the QD film[44]. While exchange to shorter ligands can improve electronic coupling between QDs and carrier transport of QD film, formation of trap states from QD surface defects and cracks within the QD film provide their own limitations to carrier transport across the QD film.

The self assembly of CdSe QDs into three dimensional superlattices is demonstrated through controlled evaporation of a mixed solvent system.[45] One component of the mixed solvent system does not interact favorably with QDs. In a typical assembly, CdSe QDs capped with trioctylphosphine chalcogenide are dispersed in a 90% octane and 10% octanol mixture at 80^{o}C and pressure is slowly reduced to control the

evaporation of the mixture. As the more volatile component, octane evaporates faster than octanol. The composition of the solvent mixture becomes more octanol rich and induces nucleation of QDs to minimize unfavorable interaction. The monodisperse QDs self-organize into a face-centered cubic (fcc) lattice.

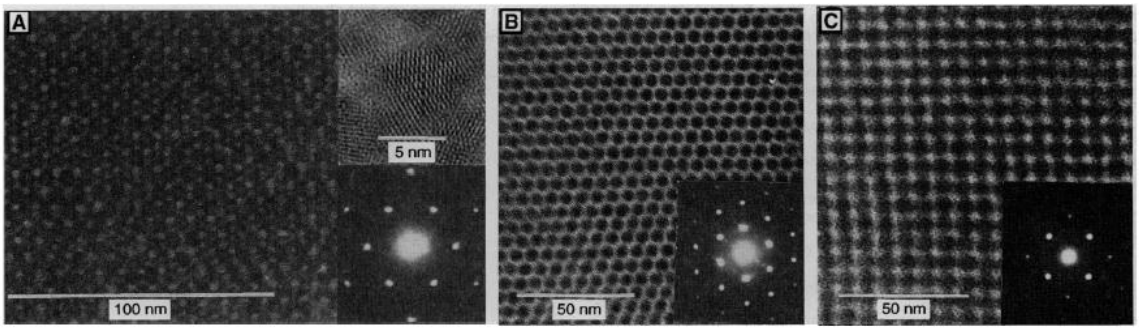

Figure 1.5 HRTEM images and ED patterns (inset) showing different orientation of the QD superlattice showing the characteristic a) (111) plane, b) (101) plane, and c) (100) plane of the fcc lattice. Reprinted with permission from ref [45]. Copyright 1995, AAAS.

Illumination with polarized light with crossed polarizer under an optical microscope shows the expected features of a crystal such as depolarized luminescence and scattering from grain boundaries. High resolution transmission electron microscope (HRTEM) reveals the actual morphology of the QD superlattice, and electron diffraction (ED) measurement reveals the characteristic diffraction patterns of (100), (101) and (111) planes (figure 1.5) as found in a fcc lattice, confirming the crystalline nature of these QD superlattices. More complex superlattices have also been formed using binary nanoparticle system with opposite charges[46] and different sizes[47][48]. Au NPs functionalized with negatively charged carboxylate group and Ag NPs functionalized with positively charged tetramethylammonium group self-assemble into a diamond like

superlattice due to electrostatic interaction between the NPs. Binary NP systems containing Fe_2O_3, Au, Pd, PbS, or PbSe NPs with various sizes have demonstrated self assembly into even more complex superlattices.

1.4.2 Fabrication and properties of quantum dots molecules

Analogous to the formation of molecules from atoms, QDs as artificial atoms have also been assembled into quantum dot molecules (QDMs) with different inter-QD coupling[49]. Alivisatos and co-workers[50][51] have synthesized QDMs with epitaxially grown inorganic interconnections at linear or branched junctions. Some examples of these QDMs are CdSe tetrapods, branched rods and branched tetrapods with CdS/CdSe/CdTe segments. Metal and magnetic NPs with inorganic connections are also synthesized to build more complex nanostructure[52]. An interesting property from the tetrapods consisting of a CdSe core and CdS arms is the formation of a higher energy emissive state with electron and hole being spatially confined at the arms and core respectively[53]. However, bonding between QDs in these QDMs is very specific to the system itself and cannot be easily generalized to other kinds of nanoparticles. A more general approach is to spatially arrange QDs into clusters with controlled size and morphology. Using a template to assemble QDs into small clusters has demonstrated to be a promising and broadly applicable strategy to assemble QDMs. Cui et al.[54] used templates with lithographically defined patterns and capillary force to assemble NPs with defined cluster size and location. Arrays of holes, trenches, with defined position and orientation have been fabricated on a polymer resist through electron beam lithography

(EBL), and 50 nm diameter Au and 60nm Ag nanoparticles are successfully assembled only in the predefined holes or trenches. It becomes more difficult to assemble ordered structure within the patterns as particle size decreases to 8nm and even 2nm.

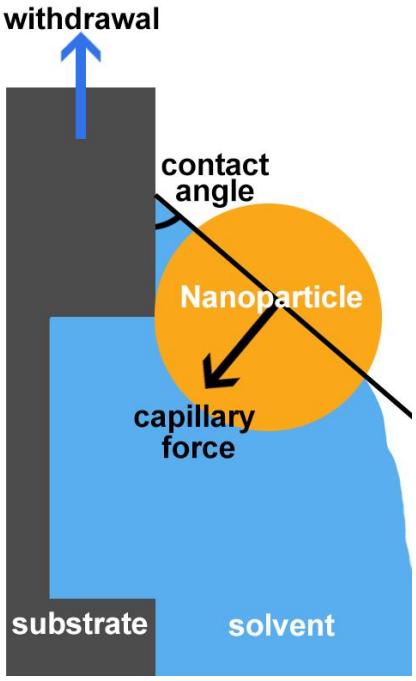

Figure 1.6 Schematic showing the direction of capillary force exerted on nanoparticle based on contact angle between solvent front and substrate as solvent evaporates. In the presence of a geometric feature on substrate (hole), capillary force can assemble NP into the hole.

In capillary force assembly, a substrate is dipped into a solution containing the NPs to be assembled and is withdrawn with controlled velocity. Capillary force assembly utilizes the capillary force that a NP experiences as it approaches the interface where solvent, substrate, and air meet, an interface known as the three-phase contact line. As the contact line moves across the substrate, NPs at the contact line are trapped and become

immobile when the solvent evaporates. The solvent evaporation exerts a capillary force pushing the NPs onto the substrate, and the direction of the force exerted depends on the contact angle of the solvent with the substrate. When the substrate contains geometric features like holes or trenches, capillary force from solvent evaporation pushes the NPs into these geometric features, provided that the NPs are not interacting strongly and being mobilized on other areas of the substrate.

Overall, EBL is not an efficient way to fabricate wafer scale substrates with geometric features less than 20nm. An ideal system to fabricate wafer-scale substrates with dense arrays of holes in the range of 20nm in diameter is block copolymer thin film. Within a block copolymer chain, there are two sub-chains, each containing its own monomer units. These two sub-chains form the two blocks of the entire polymer chain and the two blocks are joined covalently. A well-characterized block copolymer system is polystyrene-block-polymethylmethacrylate (PS-b-PMMA)[55-59], which form well-organized, nano-sized domains with a variety of morphology based on the volume ratio of the PS block to the PMMA block. Typically a solution with block copolymer dissolved is spin-coated on a substrate and the substrate is thermally annealed at a temperature above the block copolymer's glass transition temperature, which allows the polymer chains to phase separate and self assemble into nano-sized domains. Using PS-b-PMMA block copolymer with around 70% volume of PS, Misner[60] et al. formed PMMA cylinders within a PS matrix. The PMMA cylinders can be etched away by UV and remove with acetic acid to generate a template with nanoscopic holes of around 20nm in diameter. The nanoporous template is dipped into a very dilute heptane solution with 5nm

CdSe QDs. There is evidence of QDs filling the holes but the filling is sparse and random across the surface of the template. Figure 1.7 shows the deposition result using various concentrations of 5nm CdSe QD solution.

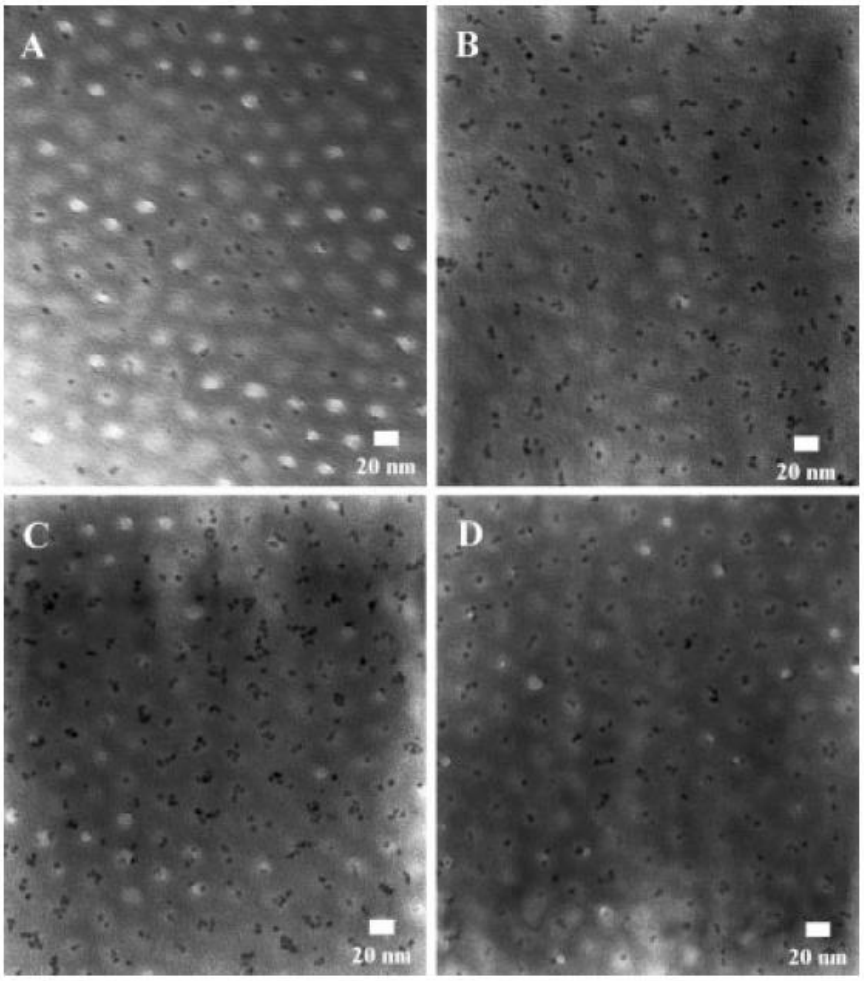

Figure 1.7 SEM images of 5nm CdSe QDs deposited in PS-b-PMMA template at different concentrations using capillary force assembly. a) 65 µg/mL, b) 130 µg/mL, c) 240 µg/mL, and d) 130 µg/mL with lower withdrawal speed. Reprinted with permission from ref [60]. Copyright 2003, John Wiley and Sons.

1.4.3 Plasmonic effects on photoluminescence of quantum dots

The photoluminescent properties of QDs can be strongly modified in the presence of surface plasmons from metal nanoparticles. In general, the coupling of QDs with surface plasmon is dominated by two effects – local field enhancement from local surface plasmon resonance (LSPR) and non-radiative energy transfer (NRET) from QDs to metal nanoparticles. In the photoluminescence (PL) process, local field enhancement can enhance both the excitation and emission light intensity[61]. Enhanced excitation leads to a higher excitation rate for QDs when field enhancement is present. Surface plasmon can also enhance the spectral region of the QD emission that is in resonance with the surface plasmon peak. An excited QD can also transfer energy to metal nanoparticles via NRET, which leads to quenching of PL intensity and significant decrease of total lifetime of excitons when NRET becomes the major decay process of excitons. NRET to metal nanoparticle provides another non-radiative decay channel for QD excitons but it does not alter the intrinsic radiative rate of QD emission. However, the radiative decay rate could be altered by what is known as the Purcell effect[62], caused by the increase in local density of states of electromagnetic modes due to presence of metal NPs. The influence of field enhancement and quenching on QDs depend on the degree of coupling between QDs and metal NPs. Several parameters such as the distance between QDs and metal NPs and the spectral overlap between QDs and surface plasmon can be changed to control the degree of coupling and therefore the extent of field enhancement and quenching from NRET. Many studies have been conducted to understand how varying the spectral position of surface plasmon and separation distance affect the PL intensity and lifetime of

QDs. However, the result from these studies is not consistent with each other, which could be caused by the variation in the plasmonic nanostructure under investigation and sample inhomogeneity. An earlier report from Komarala et al.[63] showed that there is not a significant decrease in lifetime for 556nm emission of CdTe QDs in resonance with surface plasmon peak from a layer of Au NPs. Subsequent study from same authors[64] showed a significant quenching effect, calculated from decrease in lifetime, when emission of QDs and surface plasmon are in resonance. However, there are some general trends that are concluded from both studies. CdTe QDs with emission red-shifted from surface plasmon peak of Au NPs layer show significant reduction in lifetime from tens of nanoseconds to a few nanoseconds. There is also a strong dependence of PL intensity enhancement on separation distance between QDs layers and Au NP layer. Quenching effect dominates in short separation and levels off as separation increases. There is an optimal separation that maximizes PL intensity with the two opposite dependence of field enhancement and quenching on separation. The inconsistency in some of the experimental results, complicated by the variety of plasmonic nanostructures and QDs studied in the literature, motivated Ratchford et al.[65] to conduct separation dependence study with a single QD near a single Au NP. This model system eliminates complexity that could come from sample inhomogeneity and complex plasmonic nanostructure. It provides a good reference point to interpret experimental results from other studies with related plasmonic nanostructure.

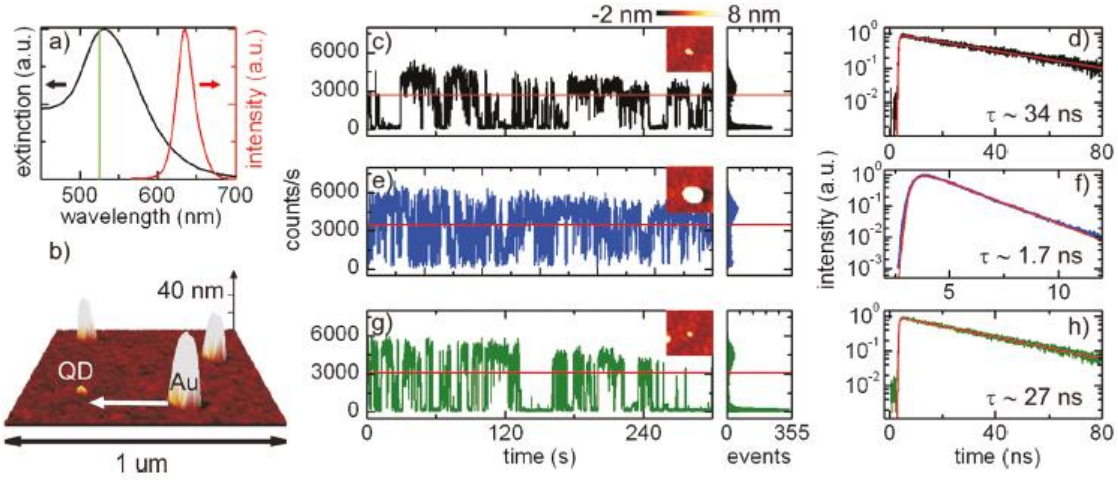

Figure 1.8 a) Ensemble optical spectra: Au NP extinction spectrum (black), QD PL spectrum (red), and excitation laser wavelength (green). b) AFM image of a QD and Au NPs with a white arrow denoting the path of the Au NP. Emission trajectories and corresponding PL decays are shown for c, d) the QD alone, e, f) the QD near the Au NP, and g, h) the QD after Au NP was pushed away. In all emission trajectories, 50 ms time bins are used, red lines denote threshold cutoffs, and AFM images (250 nm by 250 nm) of the structures are shown as insets. Reprinted with permission from ref [65]. Copyright 2011, American Chemical Society.

As shown in figure 1.8, with an atomic force microscope (AFM), the position of a single QD of ~4nm in diameter and Au NP of ~35nm in diameter are imaged. Using AFM nanomanipulation, Au NP could be brought close or away from a QD reversibly. A confocal microscope equipped with a spectrograph and an avalanche photodiode (APD) coupled to the AFM could simultaneously measure the PL intensity and lifetime of QD as an Au NP is brought close to the QD. Local field enhancement leads to increased excitation rate of QD, which decreases with increasing separation between QD and Au NP. This effect alone would have led to increase in PL intensity. However, at short distance, NRET from QD to metal, which decreases the total lifetime and PL intensity, is the dominant process and offsets the gain in intensity from increased excitation. At longer

distance, NRET becomes much less dominant and PL intensity can be enhanced compared to bare QD, despite decrease in excitation rate with distance. PL lifetime decreases monotonically with decreasing separation, while PL intensity increased and then decreased with decreasing separation.

1.4.4 Plasmonic effects on energy transfer between quantum dots

Energy transfer can occur between two QDs when they are in close proximity to each other. The process is known as Förster Resonance Energy Transfer (FRET) and is particularly efficient when the emission peak of the donor overlaps strongly with the absorption peak of the acceptor. A parameter that characterizes the effective range of FRET is called the Förster radius (R_o), the distance at which transfer efficiency is at 50% with the dipole-dipole coupling mechanism. For QDs, R_o is typically only a few nanometers. Coupling of surface plasmon with a FRET donor-acceptor pair has shown to increase R_o of the system in a study conducted by Lunz et al.[66], which includes a layer of donor QDs and a layer of acceptor QDs with a layer of Au NPs in between. The distance between donor and acceptor QDs is made large enough such that there was no FRET in a sample containing only donor and acceptor QD layers. With the insertion of a layer of Au NPs in between donor and acceptor QD layers maintained at the same separation distance, FRET is observed through the decrease of donor emission and increase of acceptor emission relative to the donor-acceptor bi-layer sample. There is a small decrease in donor decay lifetime from 0.53ns to 0.49ns for donors coupled to Au NPs only compared with donors coupled to Au NPs and acceptors QD.

Though many studies have been devoted to FRET or surface plasmon coupled fluorescence, there are relative few studies on surface plasmon coupled FRET and most dated back to only a few years ago. In a surface plasmon coupled FRET system, donor, acceptor, and the plasmonic structure can all participate in energy transfer. The degree of coupling between plasmonic NPs and QDs are influenced by the same parameters like spectral overlap and separation distance, as in FRET system or surface plasmon enhanced fluorescence. Besides the increase in $R_{o,}$ surface plasmon coupled FRET can lead to further decrease in lifetime of donor QDs. Both FRET and NRET to metal NPs contribute to decrease in lifetime of donor QDs, and the facilitation of FRET by surface plasmon can lead to a even greater decrease in lifetime than just the sum of the two effects. Su et al.[67] conducted a study on plasmonic influence of Ag NPs on a donor/acceptor QD system. A mixed donor/acceptor QD film is deposited on fused silica substrate and Ag NPs with variable thickness of silica shell are deposited on top of the mixed QD film. The authors observed a moderate increase in donor intensity and a dramatic increase in acceptor intensity when Ag NPs are present. For the PL lifetime measurement, a bi-exponential fit is used for the decay lifetime of sample with Ag NPs. The fast component shows strong separation dependence while the slow component shows little separation dependence. The authors attributed intrinsic radiative lifetime and NRET to metal to the slow component and Ag NP enhanced FRET to the fast component. However, the assignment of NRET to metal to the slow component is not consistent with results obtained from other studies[65][66] that show fast NRET from QD to metal NPs, in comparison with the intrinsic radiative decay rate.

To investigate selectively the plasmonic influence just on donor or just on acceptors in a FRET system, Ozel et al.[68] developed a multi-layer system consisted of CdTe donors, CdTe acceptors, and Au NPs, with variable layer order and separation distance between each layer. A layer of Au NPs is deposited on glass substrate, followed by polyelectrolyte bilayers of positively charged poly(diallyldimethylammoniumchloride) (PDDA) and negatively charged poly(styrene sulfonate) (PSS). In this tri-layer system of donors, acceptors, and Au NPs, by selectively depositing donor QDs or acceptor QDs as the immediate layer after the Au NP layers, a plasmon-donor coupled (pD-A) or plasmon-acceptor coupled (pA-D) FRET system is made respectively. Figure 1.9 b) and c) show the plasmon-donor coupled (pD-A) and plasmon-acceptor coupled (pA-D) FRET systems respectively.

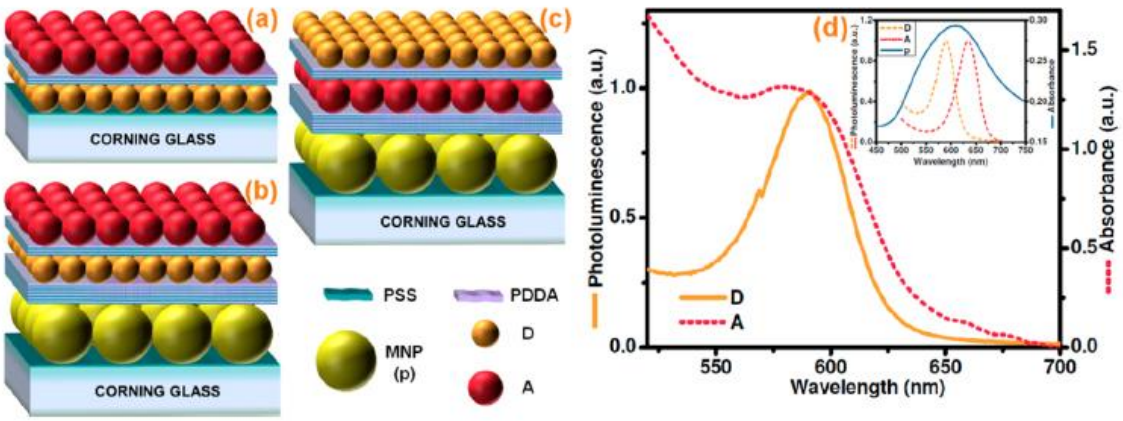

Figure 1.9 a) Layered architectures of a) FRET, represented as D-A b) plasmon coupled FRET with plasmon coupling only to the donor QDs (pD-A), and c) complementary plasmon coupled FRET with plasmon coupling only to the acceptor QDs (pA-D). d) PL spectrum of the QDs given with the optical absorption spectrum of the acceptor QDs and (inset) PL spectra of both of the QDs given with the absorption spectrum of the Au NP film. Reprinted with permission from ref [68]. Copyright 2013, American Chemical Society.

With the pD-A system, donors can either transfer energy to Au NPs via NRET or to acceptors via FRET. With the pA-D system, donor can only transfer energy to acceptor via FRET but there is no coupling between donors and Au NPs. With a multi-exponential fit, the amplitude averaged PL lifetime of donor decreases from 1.33ns to 0.62ns when only FRET to acceptor is present. Plasmonic influence on donor without FRET to acceptor decreases the lifetime from 1.33ns to 0.51ns. The lifetime of donor decreased down to 0.29ns when donors are coupled to both Au NPs and acceptors. However, in the case of pA-D system in which donors were not coupled to Au NPs but only to acceptors via FRET, the lifetime of donors was 0.67ns, which was very similar to the lifetime of donor (0.62ns) measured in a bilayers system of just donor and acceptor layers. This study demonstrates the order of surface plasmon coupling with donors (pD-A) or acceptors (pA-D) can make a significant difference in the optical properties of a surface plasmon coupled FRET system.

Using a similar tri-layer system, Zhang el al.[69] varied the thickness of the polyelectrolyte layer in between donor, acceptor, and Au NP layers to study the dependence of energy transfer rate, efficiency, and enhancement of acceptor emission on separation distance between each layer. The tri-layer structure consists of CdTe QD acceptor layer on fused silica substrate, followed by Au NP layer and CdTe QD donor layer on top. Similar to the study mentioned above, the authors demonstrated plasmon coupled FRET in enhanced acceptor emission and reduced lifetime of donor when they compared the PL intensity and lifetime measurements of FRET only, plasmon only, and plasmon coupled FRET systems. In addition, two distance dependent measurements are

conducted. One is keeping the separation between donor and Au NP layers constant while varying the separation between Au NP and acceptor layers; the other one is the opposite by varying only the separation between Au NP and donor layers. It is concluded that the coupling between Au NPs and donors is more dominant than that of Au NPs and acceptors, based on the higher sensitivity of energy transfer efficiency on separation between donor and Au NPs as well as greater increase in effective Förster radius when Au NPs are brought close to donors than when Au NPs are brought close to acceptors. The distance dependence of energy transfer efficiency of plasmon coupled FRET show the same d^{-4} dependence as in traditional FRET theory and the enhancement is expressed in the effective Förster radius term.

Chapter 2: Instrumentation for fabrication, structural characterization, and optical spectroscopy

2.1 Atomic Force Microscopy (AFM)

Atomic force microscopy (AFM) is a very versatile technique to characterize the topography of a surface. AFM falls under the general category of scanning probe microscopy (SPM), which includes scanning tunneling microscopy (STM) and many other variations that utilize a scanning probe to measure mechanical, electrical, or magnetic properties of a surface. AFM is especially useful for topographic imaging of non-conductive surface, which is generally not possible to image using STM since the technique relies on the tunneling current between STM tip and sample surface. AFM was first developed by Binnig and co-workers[70] in 1986 and much progress has been made in imaging resolution and the information that could be extracted from the AFM tip-sample interaction. Figure 2.1 shows the general concept of how morphology can be scanned with AFM. An AFM probe is attached to the scan head of an AFM and the probe is scanned across the surface line by line during imaging. An AFM probe consists of a flexible cantilever and a sharp tip at the end. Typically AFM probes are made of silicon (Si) or silicon nitride (Si_3N_4). The top of the cantilever can be coated with aluminum or gold for increased reflectivity. The diameter of the apex of the tip can range from a few nanometers to tens of nanometers. A laser beam is directed to the top of the cantilever, which reflects the beam to a four quadrant photodetector. The photodetector is able to distinguish how far the laser is off centered by comparing the laser beam intensity measured at each quadrant; when the laser beam is hitting the center of the photodetector,

each quadrant has equal laser intensity. How far the beam is off-centered is measured by a quantity called deflection. Movement of cantilever will move the position of the laser beam spot on the photodetector. As the tip is scanned across the sample surface line by line, the photodetector tracks the deflection of the cantilever as the tip responds to surface features of the sample.

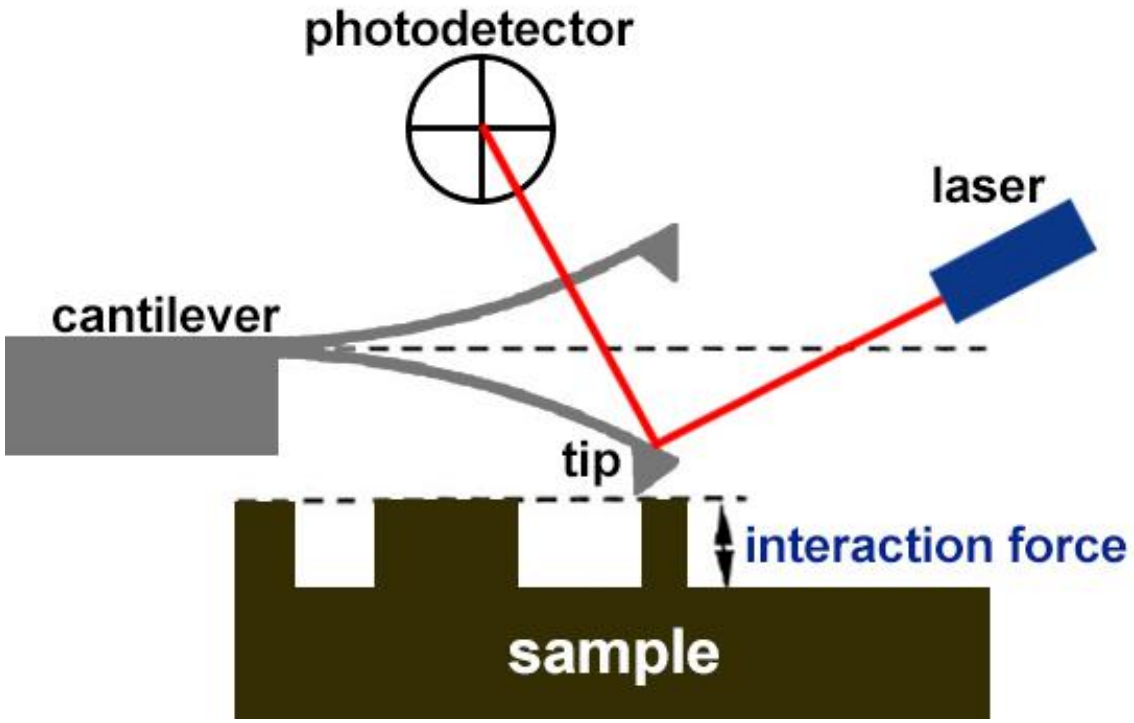

Figure 2.1 Schematics showing how surface morphology is scanned by an AFM tip based on change in the position of cantilever detected by the photodetector.

Based on the distance between the AFM tip and sample surface during imaging, AFM topographical imaging can be categories into contact mode, intermittent contact mode (tapping mode), or non-contact mode[71]. In contact mode, the tip is brought in contact with the sample surface as it moves across the surface. Height variation on the

surface will cause the cantilever to bend upward, and the force between tip and surface is repulsive. Two feedback mechanisms can be used in contact mode in response to height variation on sample surface. In constant force mode, the piezoelement that controls the height of the tip will change the height of the tip in response to the deflection of the tip. In constant height mode, the feedback mechanism of piezoelement is off and the deflection is plotted as topography as the tip is kept at a constant height. Contact mode is more suited for imaging hard and flat surface like metal or inorganic materials. In contact mode, the tip would also wear off more easily and lose resolution.

In intermittent contact or tapping mode, the AFM tip is driven to oscillate at a certain frequency and amplitude and comes in and out of contact with the surface during the cycle of oscillation. Figure 2.2 shows a force-distance curve that describes the interaction of tip and surface as a function of separation distance. Repulsion force rises up quickly as distance becomes small, corresponding to the tip pressing against the sample surface, caused by Pauli electron repulsion at the atomic level. This is the distance range in which contact mode operates. Intermittent mode operates at the distance range that involves both repulsive and attractive force. In the simplest case, the attractive force between tip and surface comes from van der Waals interactions between tip and surface as they are brought close to each other. Long range attractive force like electrostatic force and other surface forces like hydrophilic/hydrophobic forces can come into play depending on the nature of the tip and the surface.

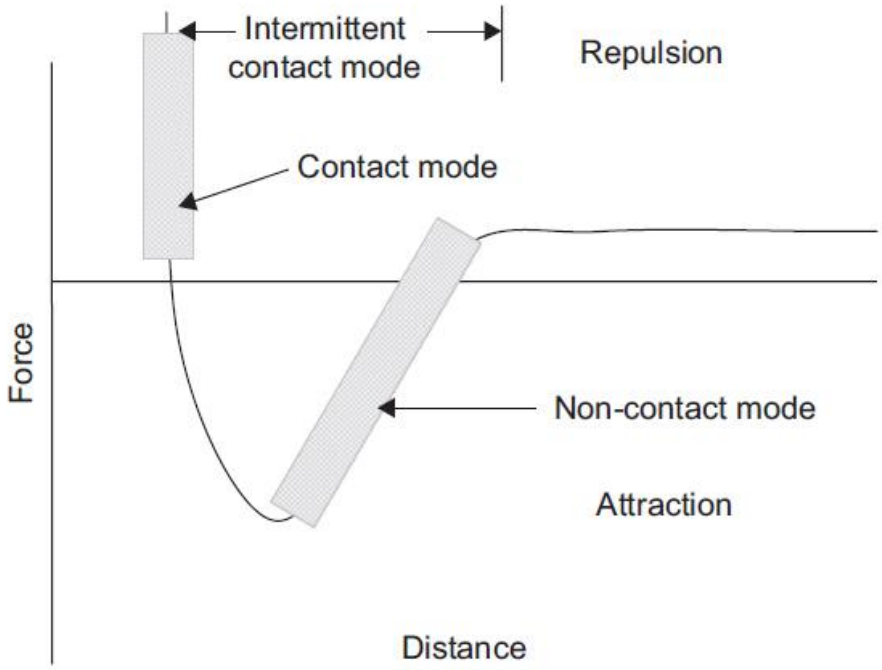

Figure 2.2 Force-distance curve between AFM tip and surface. Attractive Van der Waals force between tip and sample takes effect as they are brought close. Electron repulsion begins to increase and dominate as the distance decreases further. Reprinted with permission from ref [2]. Copyright 2009, Elsevier.

In tapping mode, the oscillation of the tip is dampened by its interaction with the surface, and the oscillation amplitude will change. The height of the tip is adjusted to maintain the amplitude at a value known as the set point as the tip encounters different topographical features of the surface. This is known as amplitude modulation AFM (AM-AFM) The height adjustment is used to construct a topographic map as the tip scans across the surface. Typically the cantilevers used for tapping mode in ambient environment need to have higher spring constant than those used in contact mode to overcome the capillary force that exists between tip and adsorbed water molecules on surface. The mechanical and surface properties of the sample will cause the actual

oscillation frequency be different from the driving frequency. This is reflected in the change of the phase of the oscillation. The changed in phase signal can be used to construct a phase image along with the topographical image in tapping mode. It is more difficult to give physical interpretation of the variation observed in phase images, but it is correlated with mechanical property like local rigidity.

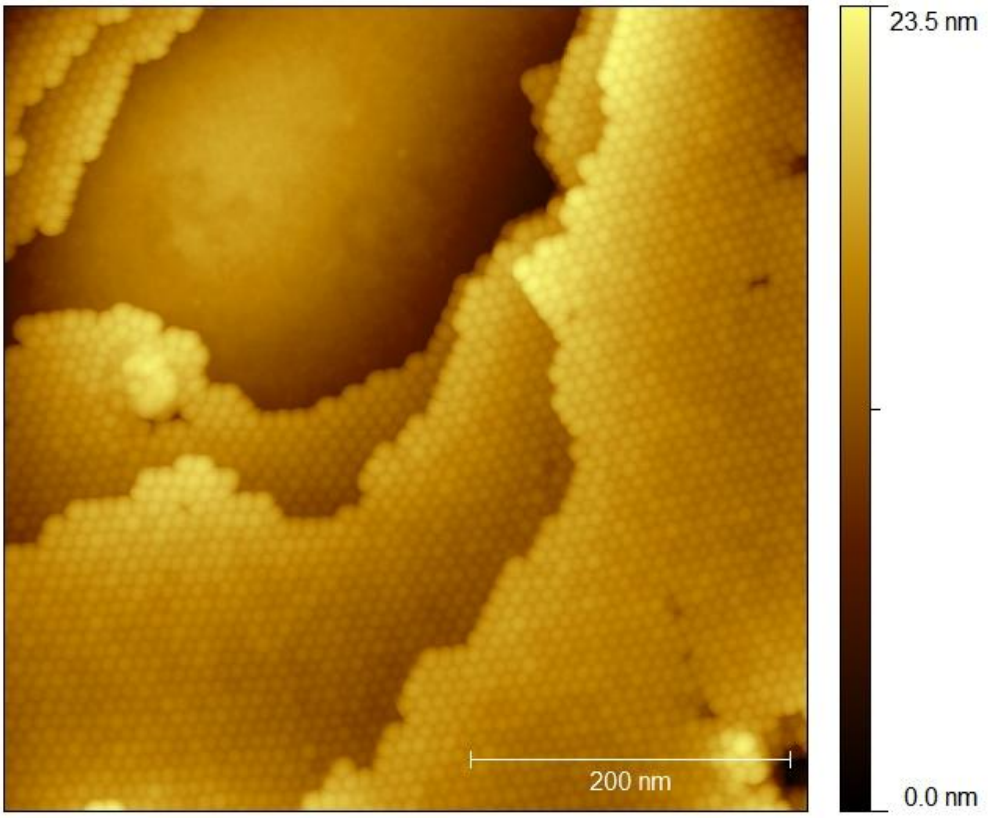

Figure 2.3 AFM topography image (tapping mode) showing three layers of Lead Selenide (PbSe) QD (5nm dia.) deposited on a fluorinated silicon substrate.

In non-contact mode, the oscillating tip never comes in contact with the sample surface as it is oscillating at small amplitude. The tip and surface interact through long-

range attractive forces like van der Waals (VDWs) forces. The height of the tip is adjusted based on changes in oscillation frequency of the tip as it interacts with surface features. This is known as frequency modulation AFM (FM-AFM). The presence of water molecules and other contaminants on surface in ambient environment can introduce other forces that strongly interfere with the VDWs forces between tip and sample surface. Capillary force can also cause the tip to stick to the sample surface given that the oscillation amplitude is small in non-contact mode. Because VDW force is short-range, non contact mode can achieve higher resolution than contact or tapping mode. Typically non-contact mode AFM is done in an ultrahigh vacuum (UHV) chamber and a suitable surface can be imaged with atomic resolution under UHV using non-contact mode AFM. There are many other imaging modes developed to probe beyond just topography of a surface. Friction force microscopy (FFM)[72] measures lateral force variation and deduce information of the local friction on the sample surface. Electric force microscopy (EFM)[73] and magnetic force microscopy (MFM)[74] use conductive and magnetized AFM tips respectively to probe and image surface charges or magnetic domains of a sample. Kelvin probe microscopy (KFM)[75] is a popular technique to measure contact potential between two surfaces, which is related to their respective work functions.

2.2 Scanning Electron Microscopy (SEM)

Conventional optical microscopy has a diffraction limit on image resolution based on the numerical aperture and wavelength of light, in the range of a few hundred nanometers. High energy electron has a de Broglie wavelength less than an angstrom and

therefore electron microscope can achieve much greater resolution than conventional optical microscope. SEM utilizes an electron beam focused with electron optics to interact with samples and collects the scattered electrons with electron detector. Figure 2.4 describes the basic components of an SEM. The electron gun[76] is the source of electron beam. There are three kinds of electron gun: thermionic, Schottky field emission, and cold field emission. Electrons need to be overcome the work function of the material in order for electron emission to occur. Thermal energy is supplied in thermionic emission to overcome the work function. Strong electric field can lower the energetic barrier to a point where electrons can tunnel out and be accelerated by the strong electric field. Schottky field emission utilizes both heat and electric field, while cold field emission uses only electric field. The brightness of cold field emission is order of magnitude higher than the other types of emission guns but also requires a much higher vacuum.

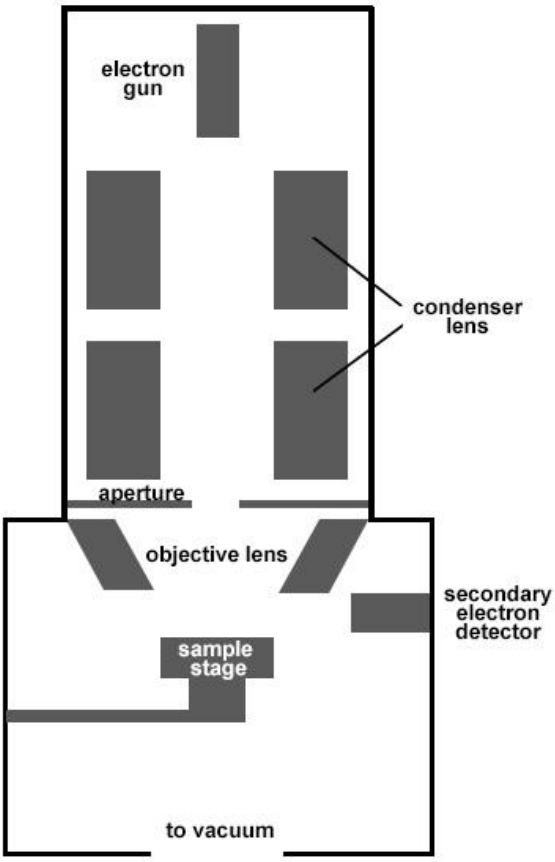

Figure 2.4 Schematic showing the basic components of an SEM

Accelerated electron beam passes through a series of condenser lens to focus the electron beam. Electron optics manipulates electrons through magnetic field. The aperture and objective lens control the spot size of electron beam and convergence angle of electron beam, which influence the final resolution and the depth of focus on the sample. As the electron beam (primary electrons) interacts with the sample, it can generate secondary electrons (SE) or backscattered electrons (BSE). Primary electrons are deflected more strongly by the nucleus than the electron cloud from the sample.

Primary electrons that go through a series of collisions with nuclei from sample could be backscattered into the direction it comes and collected by a BSE detector. Because BSE primary come from interaction with nuclei, images constructed with BSE are particularly good for samples with heavy atomic nuclei or with large mass contrast. Secondary electrons are electrons ejected from the sample due to collision with primary electrons. They are collected by the SE detector to form an SEM image. SE has smaller escape depth since generally it possess less energy than BSE. When the primary electrons excite a core electron of an atom from the sample, the relaxation of that core electron generates X-ray with wavelength characteristic to the identity of that atom. Energy dispersive spectroscopy (EDS) is an elemental analysis technique that measures the X-ray emitted from the sample to map out the chemical composition near surface of the sample.

2.3 Attenuated Total Reflection – Fourier Transform Infrared Spectroscopy (ATR-FTIR)

Attenuated total reflection-Fourier transform infrared spectroscopy (ATR-FTIR) utilizes an ATR waveguide to enhance the signal in a conventional FTIR spectrometer to measure absorption spectrum of a sample. A Michelson Interferometer[77] is used to generate an interferogram. An interferometer consists of a beam splitter that sends one beam to a fixed mirror and one beam to a moving mirror. The two beams are combined to form an interferogram, which contains information on the entire spectral range. The signal from the interferogram pass through the sample and is Fourier transformed to give

intensity over the measured spectral range. The advantage of using FTIR is that the entire spectral range is measured from one interferogram.

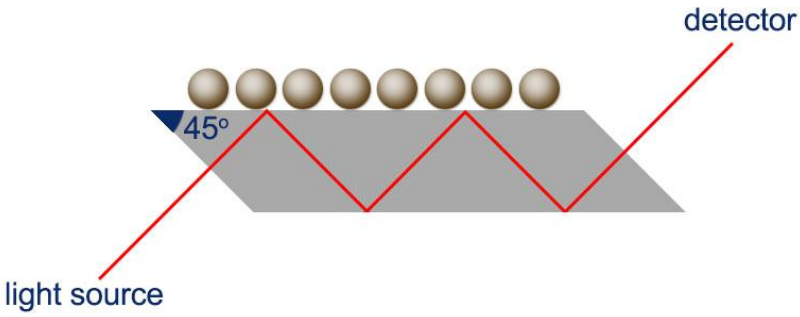

Figure 2.5 Schematic showing a monolayer of quantum dots deposited on the surface of an ATR waveguide polished with 45° bevels. Light entering from one side goes through a series of total internal reflections before exiting the waveguide and collected by the detector.

Sample is deposited on the surface of the ATR waveguide, which usually has the shape of a trapezoid or a parallelogram with 45° bevels on both sides. The ATR waveguide is made of material with high refractive index, typically a semiconductor, so that the critical angle for total internal reflection can be small at the interface. Light entering the waveguide with an angle higher than the critical angle will undergo total internal reflection along the length of the waveguide, as shown in figure 2.5. At the interface between sample and waveguide, small amount of light intensity can exist outside of the boundary of the waveguide as evanescent wave, which drops off very quickly as distance from waveguide increases. The evanescent wave is particularly suited for probing thin layer of sample on the waveguide. The ATR waveguide geometry allows multiple reflections of the incident light before it is collected, thus increasing the amount

of signal compared with a reflectance setup that only allows one reflection off of the sample. With the matching light source and detectors, spectral range from far-IR to Near IR can be measured. A Mercury Cadmium Telluride (MCT) detector is good for mid-IR and most of near IR range. Silicon detector is good for near IR to visible range.

2.4 Steady State Photoluminescence and Time Correlated Single Photon Counting (TCSPC)

When a fluorophore is excited with radiation, it can emit light at a lower energy after some vibrational relaxation. A fluorimeter has an excitation source to excite the sample and measure the emission. For steady state photoluminescence, the typical excitation source is a xenon arc lamp, which provides high and fairly uniform intensity over the entire visible range. A monochromator is used to choose the excitation wavelength and a slit is used to control the light intensity arriving at the sample. Incident light is directed away from the detector after passing through the sample. An exit monochromator picks out the wavelength collected by the detector, which could be a photodiode or a photomultiplier tube (PMT). The exit monochromator scans the entire spectral range of interest to obtain the photoluminescence spectrum. Some fluorimeter is equipped with a reference detector to monitor fluctuation in incident light intensity and the measured spectrum is scaled according to the fluctuation to provide more accurate measurement. For time correlated single photon counting (TCSPC), the same basic fluorimeter setup can be used with the addition of a few components. In TCSPC, the light source is typically a pulsed laser diode. Fluorescence decay generally ranges from micro

to nanoseconds, and the laser pulse has to have shorter duration than the decay process in order for the decay dynamics to be distinguishable. The laser pulse has a pulse shape in the time domain that is convoluted with the emission of the sample, which interferes with the counting result. Usually signal is collected with a non-emitting scattering agent to form what is known as the instrument response function (IRF). It includes the pulse shape of the laser pulse as well as any effect the optics of the instrument has on the measured signal. Signal needs to be de-convoluted with the IRF to obtain the true signal from emission. The incident laser pulse is synced with the photon counting unit of the instrument. Exit monochromator is usually set at the emission maximum of the sample. Because of the small light output intensity, a PMT is used as the detector to register each photon. PMT operates based on the photoelectric effect, in which one photon can generate one photoelectron. High voltage is applied to multiple the number of electrons to achieve a measurable signal from a single photon.

The PL lifetime decay curve is constructed by a statistical counting of the number of photons arriving at a certain time after the initial excitation. A time range of interest is binned and the number of photons are counted and added in each time bin. The result is a decay curve that reflects the dynamics of the radiative decay process. Typically exponential fit is used to fit the decay curve to obtain a decay lifetime. It might be necessarily to use a multi-exponential fit if there are several decay processes going on from the sample.

2.5 Inductively Coupled Plasma-Reactive Ion Etching (ICP-RIE)

Inductively coupled plasma-reactive ion etching is a dry etching technique that utilizes high energy plasma to etch different materials based on the processing gas used to generate the plasma. It is commonly employed in electronic processing to etch away different oxides, metals, or semiconducting materials. A variety of processing gases could be used in ICP-RIE to generate plasma: O_2, Ar, CF_4, SF_6, C_4F_8, etc. In ICP-RIE, plasma is generated in the presence of a changing magnetic field in the RF frequency, which induces an electric field that circulate the plasma in the plane parallel to the capacitive coupled plasma (CCP) plates. The CCP plates provide the forward power to drive ions to sample surface.[78] Figure 2.6 shows the schematic of an ICP-RIE system.

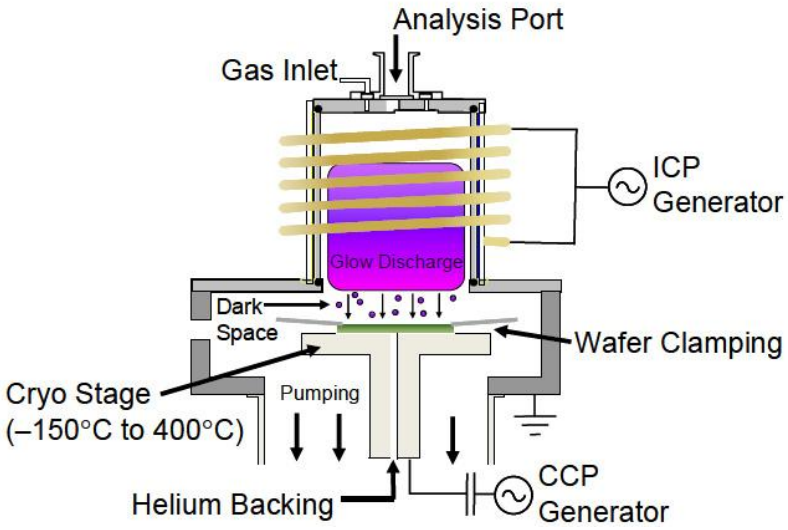

Figure 2.6 Schematic showing cross sectional view of an ICP-RIE system. Reprinted with permission from ref [9]. Copyrights 2010, CC BY-NC-SA 3.0 license.

The ICP-RIE system can have two separate chambers, one for the generation of ICP, and the other one for the CCP generator to apply forward power. This allows processing parameters such as ion density and bias voltage to be independently controlled. Parameters that could be tuned in a typical etching process the ICP generation power, forward power, processing gas flow rate, processing pressure, etch time, etc. In some system the stage is equipped to cool sample to cryogenic temperature through cooling from liquid helium. In most cases, etching anisotropy is desired when there are two or more distinct materials presented on the sample. Etching anisotropy describes how selective an etch process is towards a particular material. Oxygen plasma has high etch rate for organic materials like photoresists or polymer films because surface is being oxidized as well as bombarded by high energy ions. Argon and SF_6 etch away material by sputtering from their higher atomic mass. A combination of SF_6 and C_4F_8, known as the Bosch process, is commonly used to etch silicon. SF6 is the etching gas and C_4F_8 is the passivation gas as it both reacts with Si to form volatile compounds and forms a Teflon-like film on the silicon surface. A repeated cycle of passivation and etching can selectively etch away silicon from sample surface. Sample can heat up during etching and it can lead to inconsistent etching or structural damage of sample due to thermal expansion.

Chapter 3: Fabrication of quantum dot molecules and plasmonic nanostructures

3.1 Assembly of quantum dot molecules using block polymer template

3.1.1 Hydrophilic attraction between QDs and hydrophilic domains from amphiphilic diblock copolymer PS-b-PHEMA

Amphiphilic diblock copolymer contains two distinct segments on the polymer chain. The two segments are made of monomer units that are hydrophilic and hydrophobic respectively. Hydrophilic interactions including polar-polar attraction and hydrogen bonding are employed in chromatography to separate the more polar molecules from an organic mobile phase as they interact with a hydrophilic stationary phase.[79] The same principle of hydrophilic attraction is explored here to assemble QD molecules coated with hydrophilic ligands on the hydrophilic domains of an amphiphilic diblock copolymer thin film. Poly(styrene-block-2-hydroxyethyl methacrylate), PS-b-PHEMA, contains the hydrophobic PS block and the hydrophilic PHMEA block, which do not mix well with each other due to the unfavorable interaction between PS and PHMEA. PS-b-PHEMA with low polydispersity was purchased from Polymer Source, Inc. and 1 wt. % solution of PS-b-PHEMA in chloroform was spin coated on piranha cleaned silicon wafer at approximately 4000rpm. PS-b-PHEMA with a volume of 4:1 (PS:PHEMA) was used in order to generate PHEMA cylinders within a PS matrix.

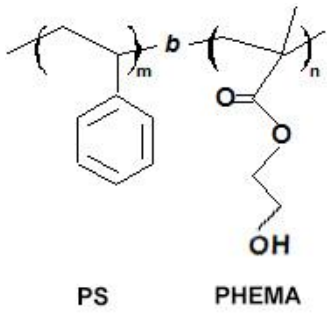

Figure 3.1 Molecular structure of PS-b-PHEMA.

PSPHEMA polymer chains were randomly mixed on as spun film and solvent annealing was used to order the PHEMA block into hexagonally organized cylinders. Annealing time, relative humidity (RH), and annealing solvent were the three parameters adjusted to optimize the morphology after annealing. As spun PS-b-PHEMA film was placed on a glass Petri dish inside a glass desiccator. At the bottom of the desiccator was the annealing solvent, which exposed PS-b-PHEMA film to only the vapor of the annealing solvent. Mixtures of chloroform and dimethylformamide (DMF) at various volume ratios were used to optimize annealing. The sealed desiccator was placed inside a customized humidity box, and the relative humidity was controlled by flowing in N_2 gas bubbled through a water reservoir. Figure 3.2a and b show the photo of the actual humidity box and a schematic showing the flow of humidified N_2 gas respectively. The chloroform vapor interacts more favorably with the PS block while DMF is the selective solvent for PHEMA. The vapor of the chloroform/DMF mixture solubilizes the copolymer chain, and the evaporation of the chloroform/DMF mixture provides a directional field that orients the domains perpendicular to the substrate. This is because solvent evaporation begins from the surface of the film and spreads into the film. If the

solvent vapor is only selective to one block, then the preferred block will tend to re-orient on the surface of the polymer film parallel to the substrate, hence a mixture of chloroform and DMF is used. For solvent annealing, the domain formation happens during the evaporation. Therefore the atmosphere surrounding the film during evaporation will also affect the final morphology. Water molecule interacts more favorably with the PHEMA block since it contains hydroxyl (-OH) group. The proper amount of humidity can promote the perpendicular orientation of PHMEA domains. The desiccator is opened slowly to slow down evaporation of solvent so that there is enough time for orientation of polymer chain to happen. The annealing results under various conditions of annealing solvent, RH, and annealing time are shown in figure 3.3. The dark spots in the AFM images correspond to PHEMA domains, the minority block, within a PS matrix (bright area) when it is aligned perpendicular to the substrate. The PHEMA cylinders are approximately 25nm in diameter.

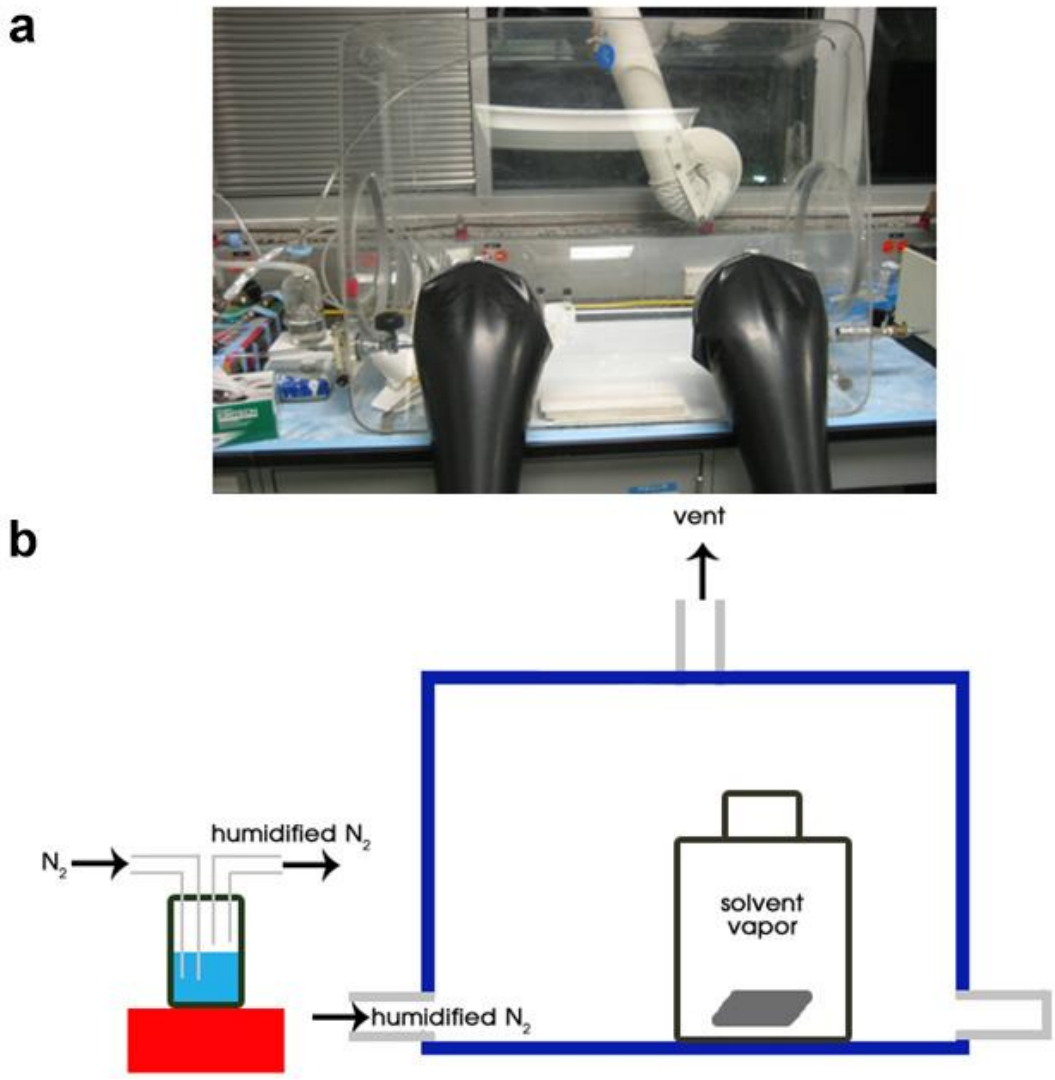

Figure 3.2 a) Photo of humidity box. b) Schematic showing how N_2 gas flows into humidity box to control humidity.

Based on the result from figure 3.3, the optimized condition is annealing PS-b-PHEMA film at a relative humidity of 70% in 1:2 ratio of DMF:chloroform for 14h. Humidity higher than 70% leads to merging of the PHEMA cylinders. When the annealing solvent has a lower ratio of DMF, the more selective solvent for PHEMA, it takes a longer annealing time to orient the PHEMA cylinders.

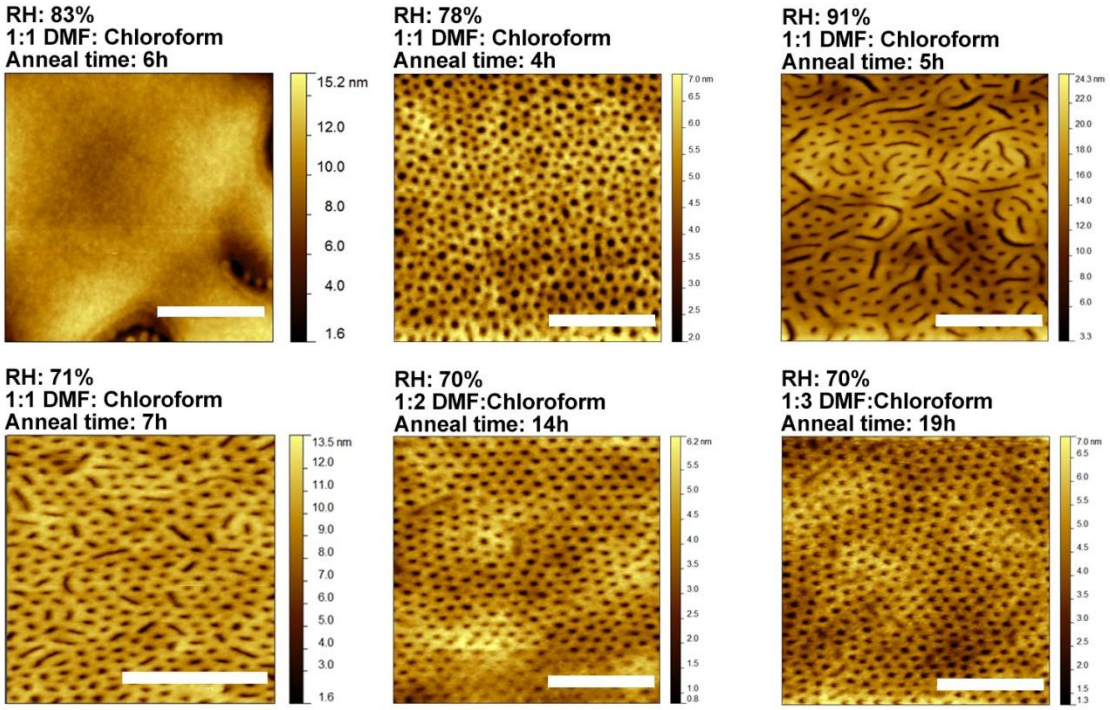

Figure 3.3 AFM topography images of annealed PS-b-PHEMA film under various annealing conditions. All scale bars are 400nm.

The hydroxyl groups on the PHEMA domains make them hydrophilic. The next step is preparing hydrophilic Lead Selenide (PbSe) QDs so that the hydrophilic attraction can assemble QDs into clusters only on the PHEMA domains. As-synthesized PbSe QD is capped with a hydrophobic ligand oleate (OA), and a ligand exchanged is performed to exchange the surface ligands from OA to 2-aminoethanthiol (AET) or 11-mercaptoundecanoic acid (MUA). These two molecules both contain a thiol group that could bind strongly to Pb atoms and a polar amino group (AET) or carboxylic acid group (MUA) for hydrophilic interaction. The ligand exchanged was performed using a bi-phasic reaction. Inside a glovebox, 50μL of PbSe (10mg/mL) stock solution in chloroform was diluted with 2mL of chloroform. 100 μL of 1M AET in methanol was

added, and the mixture was allowed to react for 15minutes. The mixture was removed quickly from the glovebox and placed inside a wet glovebox that was constantly under N_2 purge. 1.5mL of degassed DI water was added inside the wet glovebox, forming two phases with aqueous phase on top and chloroform at the bottom. Aqueous phase appeared to be brown and optically clear, as PbSe QDs capped with the polar ligands were dissolved in the aqueous phase. The mixture was centrifuged and the aqueous phase was extracted and passed through a 200 μm syringe filter to obtain water soluble PbSe QDs. In the case of ligand exchange from OA to MUA, 200μL of PbSe QDs in hexane (7mg/mL) was added to 1.0mL of MUA in chloroform (7mg/mL) in the glovebox. The solution was allowed to sit for 30 minutes and 1 mL of degassed water was added. A NaOH aqueous solution (1.2mg/mL) was added dropwise to the QD mixture until a color change happened at the aqueous phase, indicating the transfer of PbSe QDs into the aqueous phase. The purification process involved centrifugation, extraction, and syringe filter as mentioned above. Excess of ligands molecules was found to be helpful in preventing QD aggregation.

In the first attempt, freshly prepared PbSe-AET QDs solution was used for QD deposition on PS-b-PHEMA. The polymer film was submerged in the QD solution for a few seconds and the QD solution was exchanged with DI water using a pipet. The procedure of submerging in QD solution and then DI water was repeated again. Figure 3.5 shows the AFM topography images of PbSe-AET deposited on PS-b-PHEMA. The left image shows the as prepared sample. The right image shows the same sample after further rinsing in DI water. Bright spots represent the PbSe-AET QDs. While it seems

like some of the PHEMA (dark spots) are filled with QDs, there is a significant amount of bright spots remaining on the matrix. After further rinsing with DI water, less QDs remain on the matrix but they cannot be completely removed.

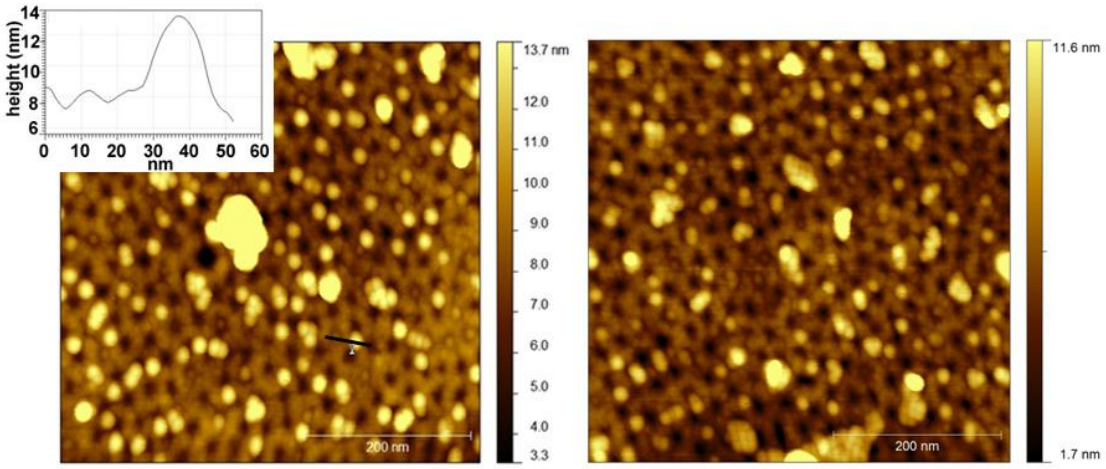

Figure 3.5 AFM images showing (left) PbSe-AET deposited on PS-b-PHEMA film (right) same film after rinsing with DI water. Inset on left shows the height line scan of one bright spot, indicated with a black line. Height is ~6nm, which is closer to diameter of PbSe QD.

The water soluble PbSe-AET QDs were not fully stable in the aqueous phase. All the PbSe-AET QDs precipitated after storing in the wet glovebox for two weeks. PbSe QDs with ligand exchange from OA to MUA was expected to be more stable than PbSe-AET since the longer alkyl chain of MUA could provide a greater steric hindrance against QD aggregation. No precipitate was observed for fresh solution of PbSe-MUA and the QDs were stable in water for about 3 weeks before showing signs of precipitation. Using fresh PbSe-MUA aqueous solution, PbSe-MUA QDs were deposit onto PS-b-PHEMA template using drop-casting and dip coating. Both approaches did not

lead to selective assembly of QD on PHEMA domains of the film, after more attempts by changing withdrawal speed from dip-coating or solution concentration and rate of evaporation of QD solutions from drop-casting. One likely reason is that there is not enough hydrophilic attraction to retain QDs only on the PHEMA domains as the interaction between QDs and PHEMA domains is weak comparing to the strong interaction between water and the substrate at the interface. At the three phase contact line, which is the interface between water, substrate, and air, the solvent front is pinned at the three phase contact line as solvent evaporates.[80] As solvent evaporates, particles dissolved in the solvent are driven to the three phase contact line and are immobilized at the contact line. When this pinning of the three phase contact line from water on PS-PHEMA is a stronger drive force than QD-PHEMA attraction, the result is a non-discriminating deposition of QDs over the surface of PS-PHEMA template.

One potential way to improve the assembly of PbSe-MUA QDs on hydrophilic domains of PS-b-PHEMA is reducing the pining of solvent with a solvent that does not interact strongly with PS-PHEMA. However, the morphology of PS-b-PHEMA, even after successful solvent annealing, is not stable in the presence of non-aqueous solvent. It is observed that the PHEMA domains could be disrupted in a 20% ethanol solution. With more non-polar solvent the morphology is disrupted even more. This restricts the QD solution to be only aqueous solution, which introduces a strong driving force to immobilize particles on the polymer surface independent of the nanodomains of PS-b-PHEMA. It was concluded that a more robust polymer template and a different

mechanism for stronger QDs-nanodomains interaction is needed to achieve the purpose of assembling arrays of QD molecules.

3.1.2 Capillary force assembly of PbSe QDs from aqueous solution on PS-b-PMMA template

Poly(styrene)-block-poly(methyl methacrylate) (PS-b-PMMA) is a well-characterized diblock copolymer system[58,81-83] that phase separates uniformly into PMMA cylinders in a PS matrix upon thermal annealing above the block copolymer's glass transition temperature. Inspired by a series of studies[84-87] that demonstrated controlled assembly of nanoparticles in aqueous solution on templates with geometric features, geometric confinement from phase separated PS-b-PMMA polymer film is explored here as a method to assemble QD molecules on nanoscopic holes of the template. The holes are formed by removing the PMMA cylinders from the film after phase separation.

As the starting points for the templates, a layer of random copolymer of styrene and methyl methacrylate (PS-r-PMMA) is spin-coated before PS-b-PMMA copolymer to provide an interfacial energy-neutral surface for the PS and PMMA block to microphase separate according to their volume ratio. The PS-r-PMMA polymer chain has a hydroxyl end that could chemically bond with the native oxide layer on silicon substrate. The spin-coated PS-r-PMMA film is annealed at 180^{o}C for 72h and then rinsed with toluene to leave a PS-r-PMMA brush layer. PS-b-PMMA is spin-coated on the brush layer and annealed at 180^{o}C for 24h. With the volume ratio of ~70% PS used here, the block-

copolymer thin film forms hexagonally packed vertical cylinders of PMMA in the PS matrix, with cylinder diameter tunable in the range of tens of nanometers (14-50nm), based on the molecular weight of the PMMA block. Figure 3.6a and b show the morphology of PS-b-PMMA film with PS:PMMA molecular weight ratio of 37.5k:18k and 68k:33.5k after thermal annealing respectively. The same film is exposed to UV irradiation to cross-link the PS block and degrade the PMMA block. The film is then washed with acetic acid to rinse away the degraded PMMA in order to form hexagonally packed holes within a PS matrix, as shown in figure 3.6c and d.

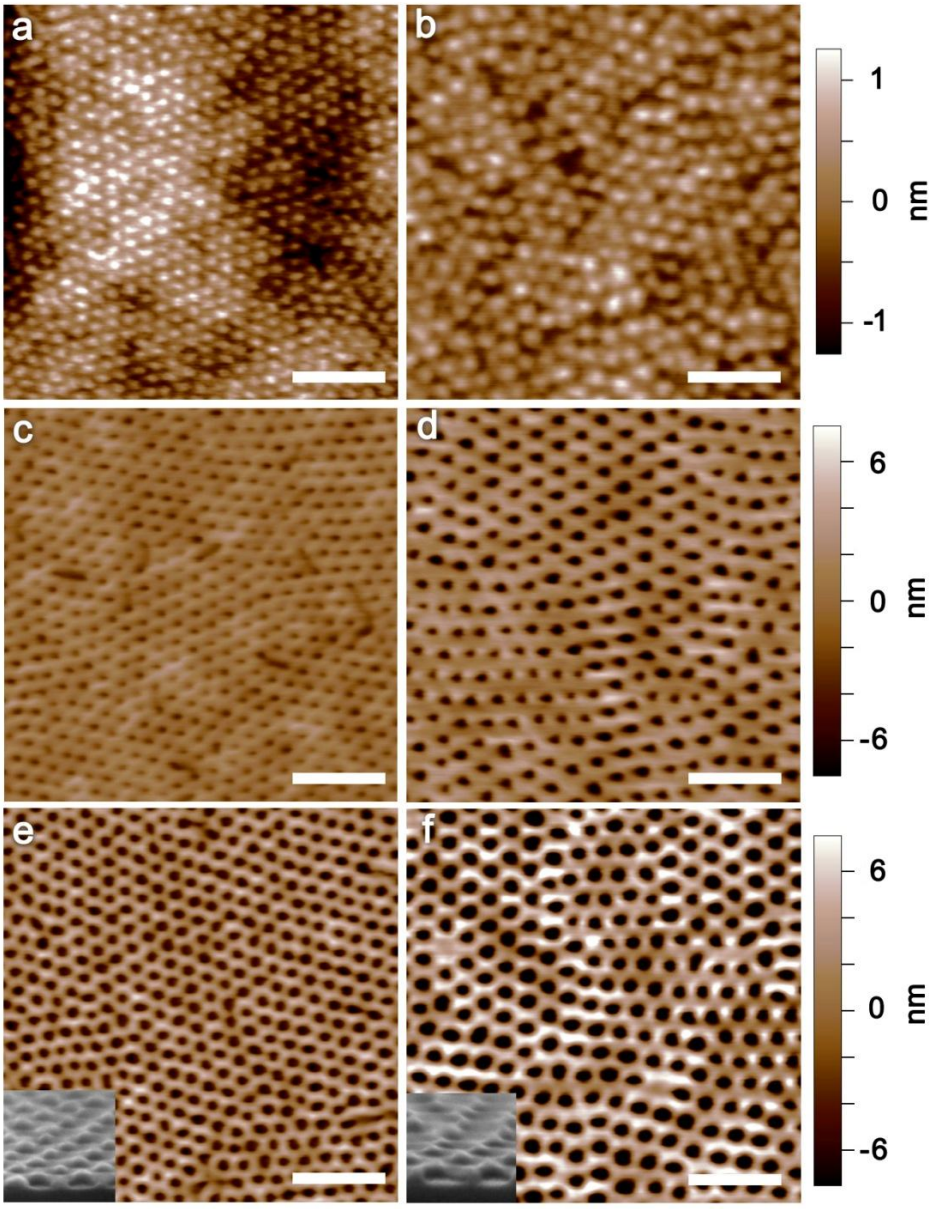

Figure 3.6 AFM topography images of PS-*b*-PMMA block-co-polymer thin films with molecular weight ratios PS:PMMA= 37.5K:18K (left) and 68K:33.5K (right), respectively. These images were obtained after spin-coating & thermal annealing (a, b), UV cross-linking and chemical etch (c, d), and O_2 plasma etch (e, f). Scale bar = 200 nm. The insets in (e) & (f) show cross sectional SEM images (100 nm x100 nm) of the films. Reprinted with permission from ref [88]. Copyright 2013, American Chemical Society.

This PS-b-PMMA template is used to assemble PbSe-MUA QDMs inside the holes of the template. A setup similar to the setup described by Wolf and co-workers[85][87] is used to carry out the assembly of QDs on PS-b-PMMA template, as shown in figure 3.7a. The motorized stage can move the substrate at speed ranges from 0.2μm/s to 1μm/s. The Peltier element controls the substrate temperature. Figure 3.7b shows a photo of PbSe-MUA aqueous solution confined between the PS-b-PMMA substrate and a fixed slide on top. The contact angle between the solution and the substrate is approximately 50^{o}. The velocity with which the three phase contact line moves across the substrate is controlled by the stage velocity, while the evaporation of the solution is controlled by stage temperature. As observed by Wolf and co-workers, conditions for successful geometric confinement of nanoparticles are matching velocities between contact line movement and solvent front evaporation, as well as a proper width to depth aspect ratio of geometric features. Stage temperature determines the solvent evaporation rate and therefore how fast the solvent front is moving due to solvent evaporation. The stage velocity can be set to match the solvent front velocity. Aspect ratio is important since with the interface of water and template, it is energetically more costly for water to have greater contact area when the holes are narrow and deep rather than wide and shallow. The holes from PS-b-PMMA after acetic acid etching are typically around 20nm in diameter and 20-25nm deep. To increase the width to depth aspect ratio, oxygen plasma etching is used to widen and also reduce the depth of the holes. Figure 3.6e and f show AFM images of 37.5k:18k and 68k:33.5k PS-b-PMMA

films after oxygen plasma etching respectively. The holes are significantly widened after oxygen plasma etching.

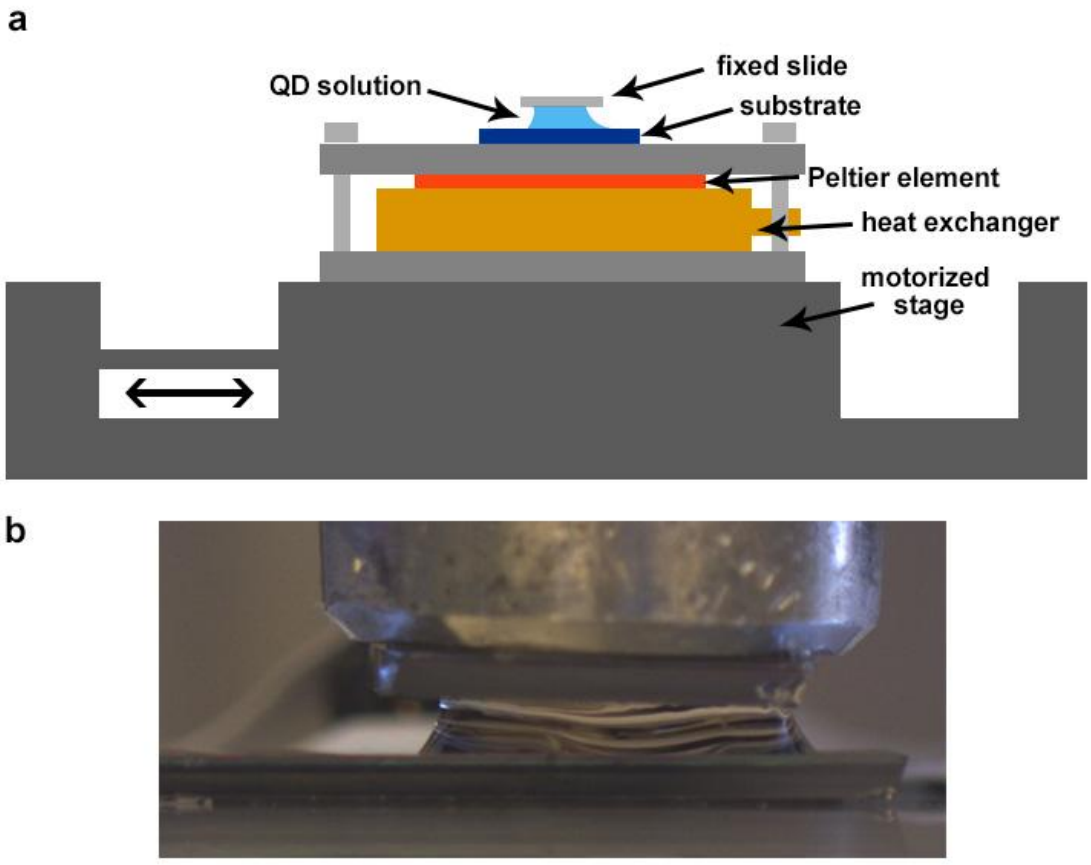

Figure 3.7 a) Schematic of the QD deposition setup. b) Photo of PbSe-MUA QD solution confined between a fixed slide and the PS-b-PMMA template on silicon substrate.

Deposition at 1μm/s stage velocity and 23°C stage temperature on a template after oxygen plasma etching shows macroscopic stripes pattern of concentrated QDs regions, this is indicative of significant pinning of the contact line, which leads to a stick-slip movement of the solvent front.[89] After oxygen plasma etching, the surface of PS-b-

PMMA becomes much more hydrophilic, and the water contact angle changes from ~75^{o} to ~20^{o} before and after oxygen etching. Figure 3.8 shows some representative PbSe-MUA aqueous phase deposition results on oxygen plasma etched PS-b-PMMA template with 1μm/s stage velocity and 23^{o}C stage temperature. In an attempt to make the surface more hydrophobic, the oxygen plasma etched PS-b-PMMA was treated with N-hydroxysuccimide (NHS), 1-(3-(dimethylamino)propyl-3-ethylcarbodiimide (EDC), and hexylamine to introduce more hydrophobic groups on the surface. The contact angle increases from ~20^{o} to ~60^{o}, but the deposition result does not show significant improvement from untreated PS-b-PMMA template.

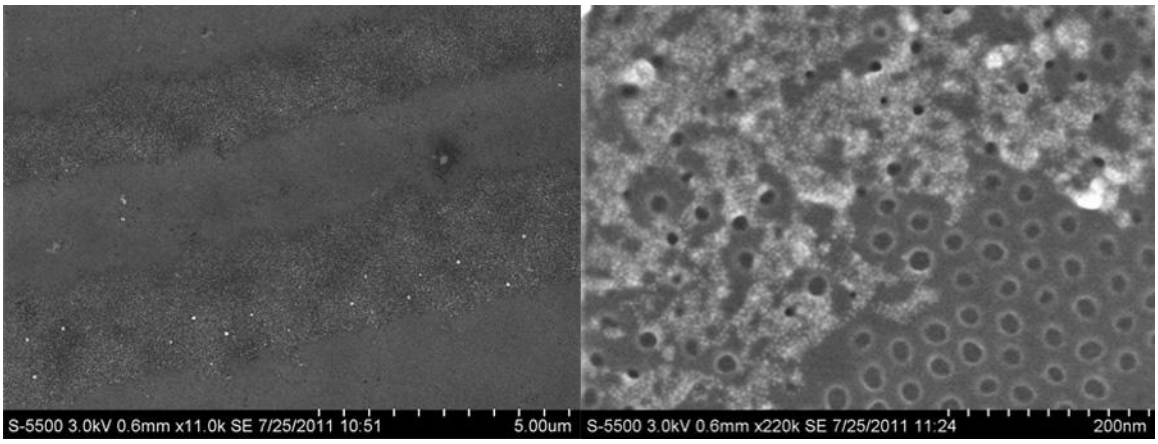

Figure 3.8 SEM images showing the stripes pattern formed during deposition of PbSe-MUA QDs on oxygen plasma etched PS-b-PMMA.

3.1.3 Capillary force assembly of PbSe QDs in organic phase on oxygen plasma-etched PS-b-PMMA template

Since pinning of water front at the three phase contact line provides a strong driving force to immobilize QDs at the contact line, deposition of PbSe QD in an organic solvent is explored here. Long term stability of PbSe-MUA in aqueous solution also becomes an issue for subsequent spectroscopic study on the optoelectronic properties of PbSe QDs. It is an additional advantage to be able to perform deposition of QDs with their native OA ligands, which could be exchanged after deposition into QDMs. PS-b-PMMA film can withstand organic solvent without significant change in surface morphology after PS-b-PMMA film is exposed to 254nm UV light for a long time in an inert environment. In the presence of oxygen gas, 254nm UV light generate ozone (O_3) and atomic oxygen radicals ($O\cdot$).[90] These two generated species are able to oxidize and etch away PS-b-PMMA layer. UV light can cause chain-scission within the PMMA block and degrade the PMMA block. The degradation process that the PS block undergoes is more complex under UV light, with cross-linking and chain scission happening all at the same times.[58] Illuminating PS-b-PMMA film with UV light in an oxygen free environment minimizes oxidation of the film so that cross-linking of PS block and chain-scission of PMMA block can become the dominant photodegradation process in each block. UV cross-linking is performed by placing the PS-b-PMMA film just 2 centimeters away from the UV lamp in a sealed glovebox under continuous N_2 flow for 9 hours.

Previous procedures of UV cross-linking and acetic acid etching developed for PMMA block removal from PS-b-PMMA film have a much shorter UV exposure time. While the exposure time is enough to degrade the PMMA block for complete removal of PMMA with acetic acid, there is not sufficient cross-linking that has happened within the PS block. Figure 3.9a and b show the morphology of PS-b-PMMA films immersed in toluene for 1 minute after a) 5 minutes, and b) 12 hours of UV cross-linking.

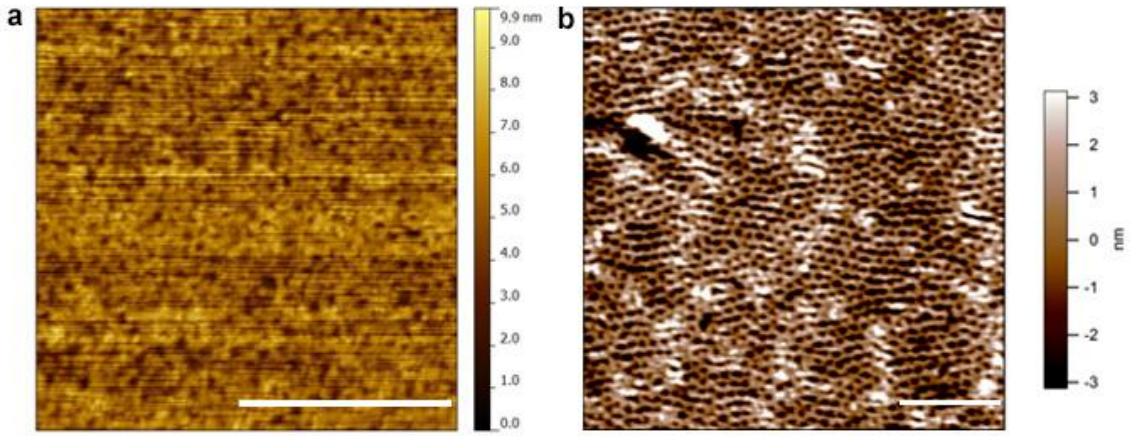

Figure 3.9 Morphology of PS-b-PMMA film with 1 minute immersion in toluene after a) 5 minutes and b) 12 hours of UV cross-linking.

As synthesized PbSe QDs are capped with oleate (OA) and dispersed in hexane. Capillary force assembly is used to deposit two different sizes of PbSe-OA QDs capped into the holes of the PS-b-PMMA films. They are identified as QD^A and QD^B with diameter of 5.0 ± 0.3 nm and 4.5 ± 0.3 nm respectively. Deposition was carried out with a QD concentration of ~10 mg/mL in hexane with a mechanical dip-coater at a withdrawing speed of 1 mm/s. This condition was found to be near optimal in filling all the holes, with a narrow distribution in the number of QDs per hole, as shown by

histograms of the two surfaces in Figures 3.10a and b for QD^A. The average number of QD^A in each cluster is 9 ± 2 and 17 ± 3 on the two surfaces, with all holes in the templates filled. The corresponding SEM images of QD clusters on the two surfaces are shown in Figure 3.10c and d, for block-copolymer nanopatterns obtained from molecular weight ratios of PS:PMMA = 37.5K:18K and 68K:33.5K, respectively. Each cluster is two-dimensional (2D), with the local arrangement of QDs in each domain near close-packing, but not highly ordered, as shown more clearly by magnified images in Figures 3.10c and d. The hexagonally packed QD clusters extend over macroscopic length scales defined by the polymer coating. Similar deposition condition was used to achieve QD^B clusters using PS:PMMA = 37.5K:18K and 68K:33.5K, with an averaged cluster size of 13 ± 2 and 19 ± 3, respectively, in accordance with the smaller diameter of QD^B.

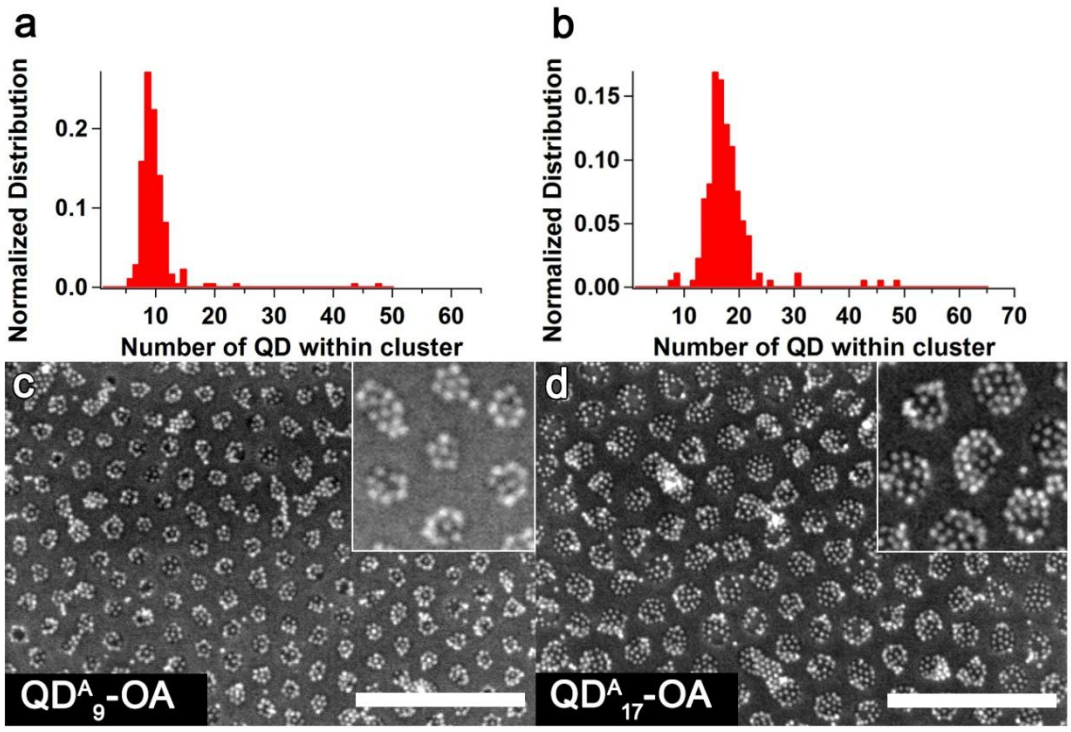

Figure 3.10 a,b) Histograms of the number of QDs within each cluster obtained from SEM images of QD^A assemblies on block-copolymer templates, with oleic acid as ligands (c,d). Images and data on left (a, c) are for QD assemblies on block-copolymer nanopatterns with molecular weight ratio of PS:PMMA = 37.5K:18K and those on the right (b, d) with PS:PMMA = 68K:33.5K. Insets in c, d) show magnified views of the same images. All scale bars = 200 nm. Reprinted with permission from ref [88]. Copyright 2013, American Chemical Society.

The results presented above are in stark contrast to previous attempts in assembling QDs into nanohole arrays formed from similar block-copolymer templates. Using the UV etched PS-b- PMMA template, Misner et al.[60] showed that, while some QDs were deposited into the holes, the process was quite random, with a large percentage of holes unfilled and a broad distribution of QDs within the holes. The correlation between the topographical features and the results of capillary force assembly for

templates with different extends (time) of reactive oxygen ion etch was investigated. Complete filling of all the holes with few QDs on the matrix only occurs when the depth of the holes is of the order of the QDs and the relative surface area of the matrix to that of the holes is small. When the template is etched for too long, the boundary that forms the hexagonal holes in the PS matrix starts to break down, leading to the formation of continuous islands of QDs. A sufficiently high concentration of QDs (10 mg/mL) is also necessary for complete hole-filling. When more dilute solutions are used on the same template, the holes are only partially filled. Figure 3.11 shows the dependence of capillary force assembly on the aspect ratio of nanoholes on PS-b-PMMA template.

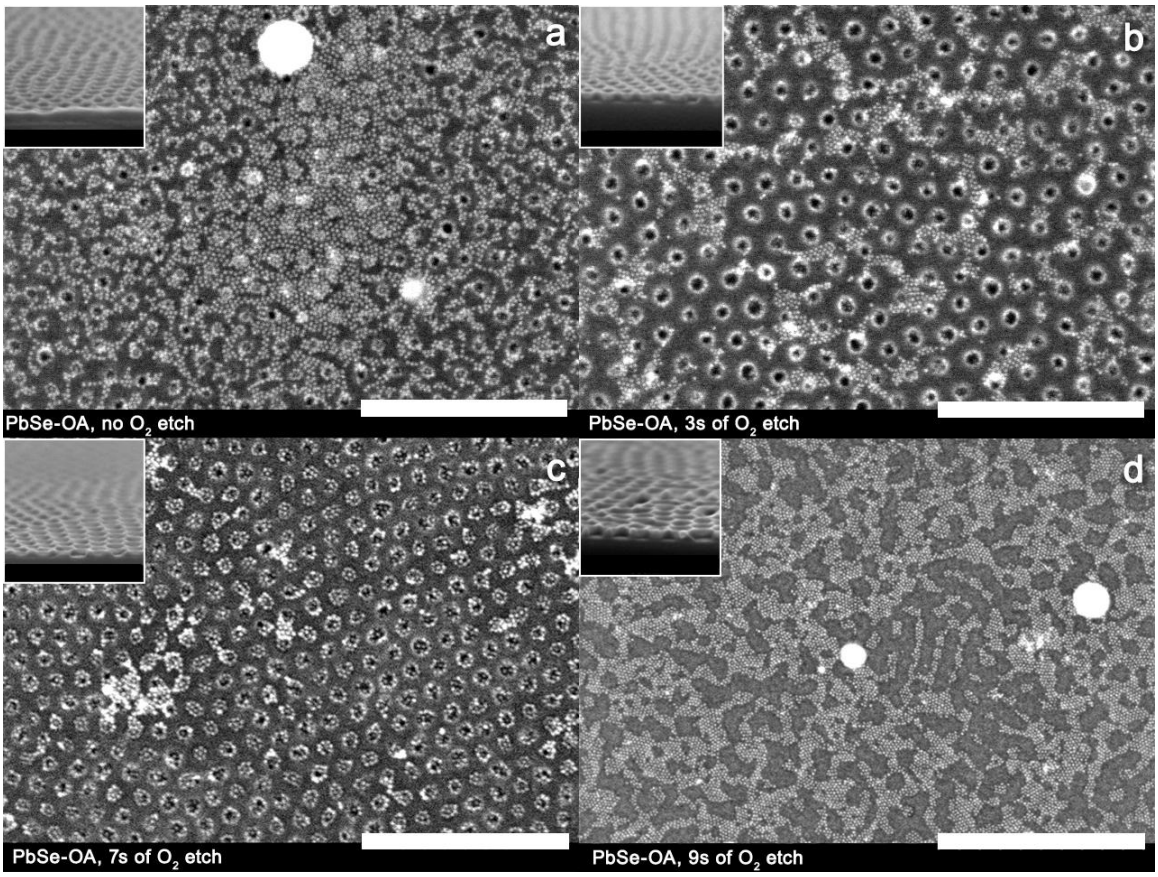

Figure 3.11 SEM images of PbSe QDs assembled onto block-copolymer templates (PS:PMMA = 37.5K:18K) with oxygen plasma etching times of (a) 0 s, (b) 3s, (c) 7s, and (d) 9s, respectively. The inset in each image shows the cross sectional views of polymer film before QD assembly. All scale bars = 300 nm. Reprinted with permission from ref [88]. Copyright 2013, American Chemical Society.

Previous studies[91][92] using X-ray photoelectron spectroscopy and friction force microscopy have shown that exposure to UV and acetic acid leaves behind −COOH functional groups on the PMMA domains. Upon O_2 plasma etching, the PMMA domains are removed while the PS matrix becomes more hydrophilic, likely terminated with −COOH groups[93][94] that may interact favorably with QDs.[95] Although the O_2 plasma treated block copolymer template shows no contrast in terms of hydrophilicity, we find

little adsorption of the QDs on the PS matrix but almost exclusive adsorption into the nanoholes. This finding highlights the critical role of aspect ratio in localizing the QD within the nanoholes of the template.

3.2 Fabrication of plasmonic metal nanodisks coupled with quantum dot clusters

3.2.1 Single-layer nanodisks

PS nanospheres with high uniformity are commercially available and have been extensively used in Nanosphere Lithography (NSL) as a lift-off mask. A different approach utilizing PS nanospheres is explored here, which uses PS nanospheres as a mask for reactive ion etching (RIE). Using a combination of positively and negatively polyelectrolyte (PE) layers, PS nanospheres can be dispersed away from each other on a substrate. The PE layers act as adhesion layers for the PS nanospheres, which also have their own surface charge based on the functional groups on the surface of nanospheres. This surface charge provides electrostatic repulsion between PS nanospheres to keep them apart, while the adhesion PE layers help to immobilize nanospheres against the attractive capillary force between nanospheres upon drying. By successively depositing metal, PS-b-PMMA, QDs, and PS nanospheres and doing argon RIE, an array of QD clusters coupled with metal nanodisks can be formed on area masked by PS nanospheres as argon RIE etch away all the materials not covered by PS nanospheres. Argon RIE is chosen as the plasma source because metal like gold cannot be etched away by reactive

ion species like oxygen plasma. Argon RIE is like a sputtering process and will etch both metal and the polymer films.

Two schemes of fabricating metal nanodisk coupled with QD clusters are illustrated in figure 3.12. In scheme A, Cr and Au are deposited on fused silica substrate first, followed by formation of QD clusters in PS-b-PMMA template and PS nanospheres. In scheme B, the deposition order is reversed, with QD clusters formed first, followed by Cr and Au. There is a layer of PMMA in each scheme deposited between QDs and metal layer, which controls the spacing between QDs and metal layer. The QDs in scheme A are not as well protected compared to the QDs in scheme B, but the deposition of metal is more straight forward since it is a hard substrate underneath. Deposition of metal on PMMA in scheme B might not result in a smooth and uniform metal surface.

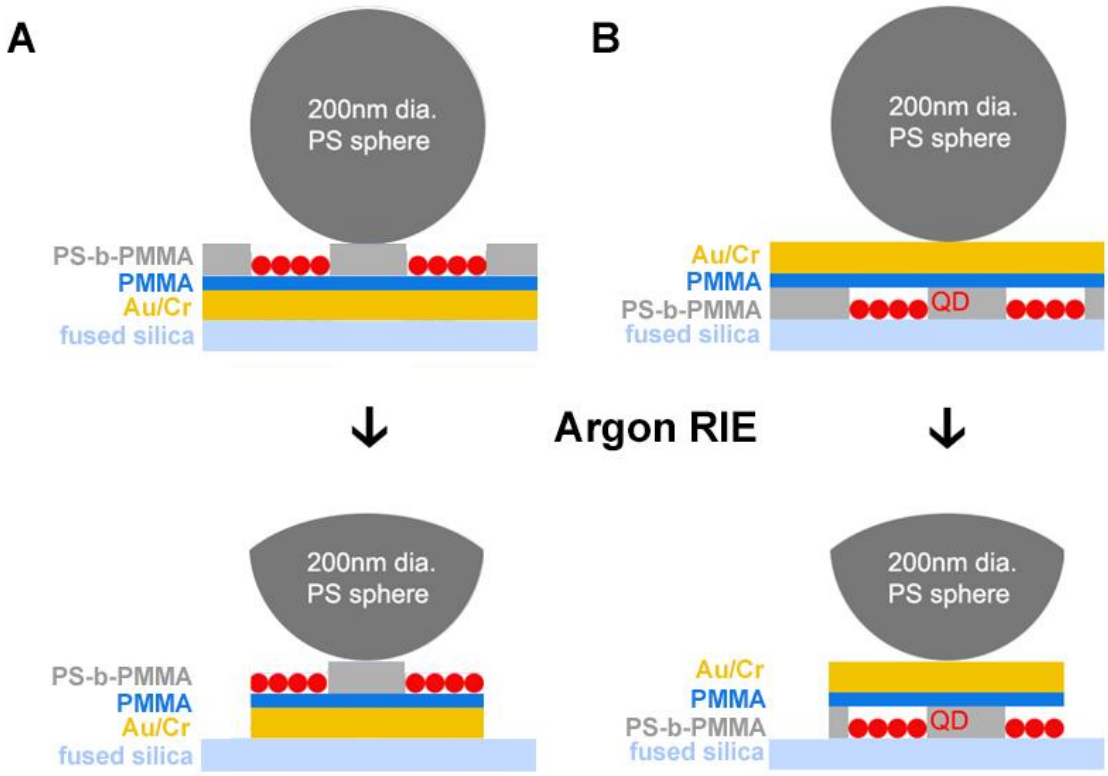

Figure 3.12. Two schemes of fabrication QD clusters coupled with Au nanodisks. Scheme B is essentially the reverse order of scheme A.

Knowing that QDs can be damaged also during argon RIE, some control experiments are done to confirm the feasibility of using PS nanospheres as argon RIE etch mask. Starting with a PS-b-PMMA template with QD clusters formed already inside the nanoholes, substrate is successively immersed in a series of three cationic and anionic polyelectrolyte solutions, poly(diallydimethylammonium chloride) (PDDA), Poly(sodium 4-styrenesulfonate (PSS), and aluminum chlorohydrate (ACH), and the substrate is rinsed with DI water after deposition of each polyelectrolyte. Sub-monolayer of negatively charged PS nanospheres is deposited onto the polyelectrolyte layers by immersing substrate in dilute solutions of PS nanospheres and dried in atmosphere. It was found that

CdSe QDs capped with octadecylamine (ODA) lose most of fluorescence intensity after PE layers are deposited on top of QDs. Control experiment is done to verify that the CdSe QDs do not lose fluorescence after exposure to water only. This suggests that the polyelectrolytes might have replaced some of the ODA on CdSe QDs and have introduced surface states that quenched the fluorescence. When a more stable CdSe/ZnS core-shell QD system capped with ODA is deposited in PS-b-PMMA template and exposed to PE layers, the fluorescence intensity is preserved.

To investigate the ability of PS nanospheres to protect area that is shadowed, Ar RIE is performed on CdSe QDs clusters formed in the PS-b-PMMA template with 200nm PS nanospheres as etch mask. Figure 3.13a and b show the SEM images of the sample before and after Ar RIE respectively. An array of PS-b-PMMA disks is formed, with diameter close to the original diameter of PS nanospheres. It is noteworthy that area closer to the center of PS nanospheres appears to be better protected. This would make sense in light of the Ar RIE process since the trajectory of Ar ions is not uni-directional. However, this means that even for area that survives the Ar RIE, there is still some damage done to the QDs, which will obscure the result from subsequent optical study from QDs that are left intact.

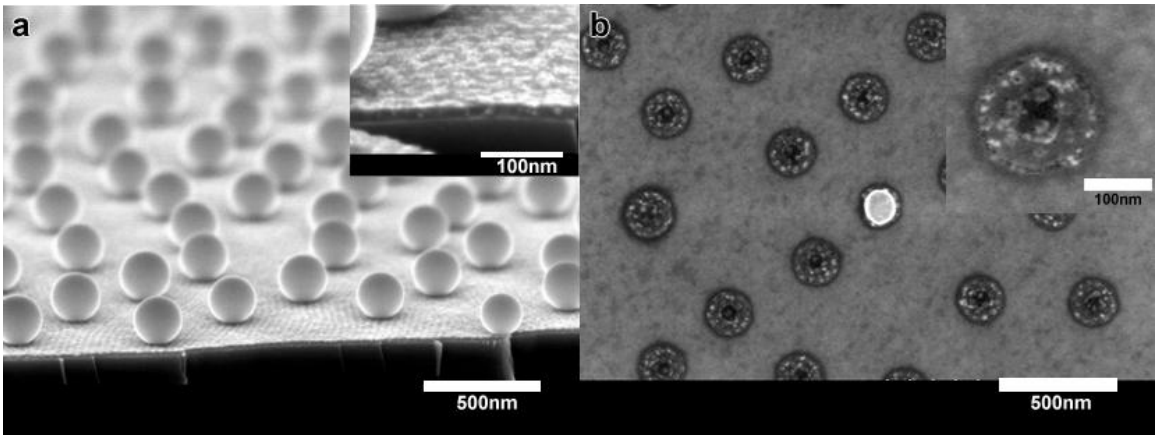

Figure 3.13 Cross-sectional view of PS nanospheres on QD clusters in PS-b-PMMA template a) before and b) after 2 mins of 50W Ar RIE. PS nanospheres are removed with scotch tape in b). Inset in b) shows area closer to center is better protected after Ar RIE.

Based on the result from the control experiments, scheme B is chosen as the method to fabricate Au nanodisks-coupled QD clusters. The PS-r-PMMA layer that provides neutral surface energy for microphase separation of PS-b-PMMA is directly spin-coated on fused silica. The same procedure of spin coating and thermal annealing of PS-r-PMMA, followed by spin-coating and thermal annealing of PS-b-PMMA, as described in section 3.1.2, is applied to the fused silica substrate. The same steps of UV cross-linking, acetic acid etching, and oxygen plasma etching produce well organized nanoholes in a PS matrix on fused silica. Capillary force assembly of CdSe/ZnS core shell QDs leads to formation of QD clusters within nanoholes of the polymer template. A layer of PMMA (Mn=6500) is spin-coated on top of the QD clusters with a 0.5 wt% solution in ethyl acetate. Ethyl acetate is used because it does not dissolve the QDs and therefore will not disrupt the arrangement of the QD clusters. A control experiment is done by spin-coating different concentrations of PMMA solutions on PS-b-PMMA

template containing QD clusters to correlate solution concentrations and spin speed with thickness of PMMA layer. The result is shown in figure 3.14.

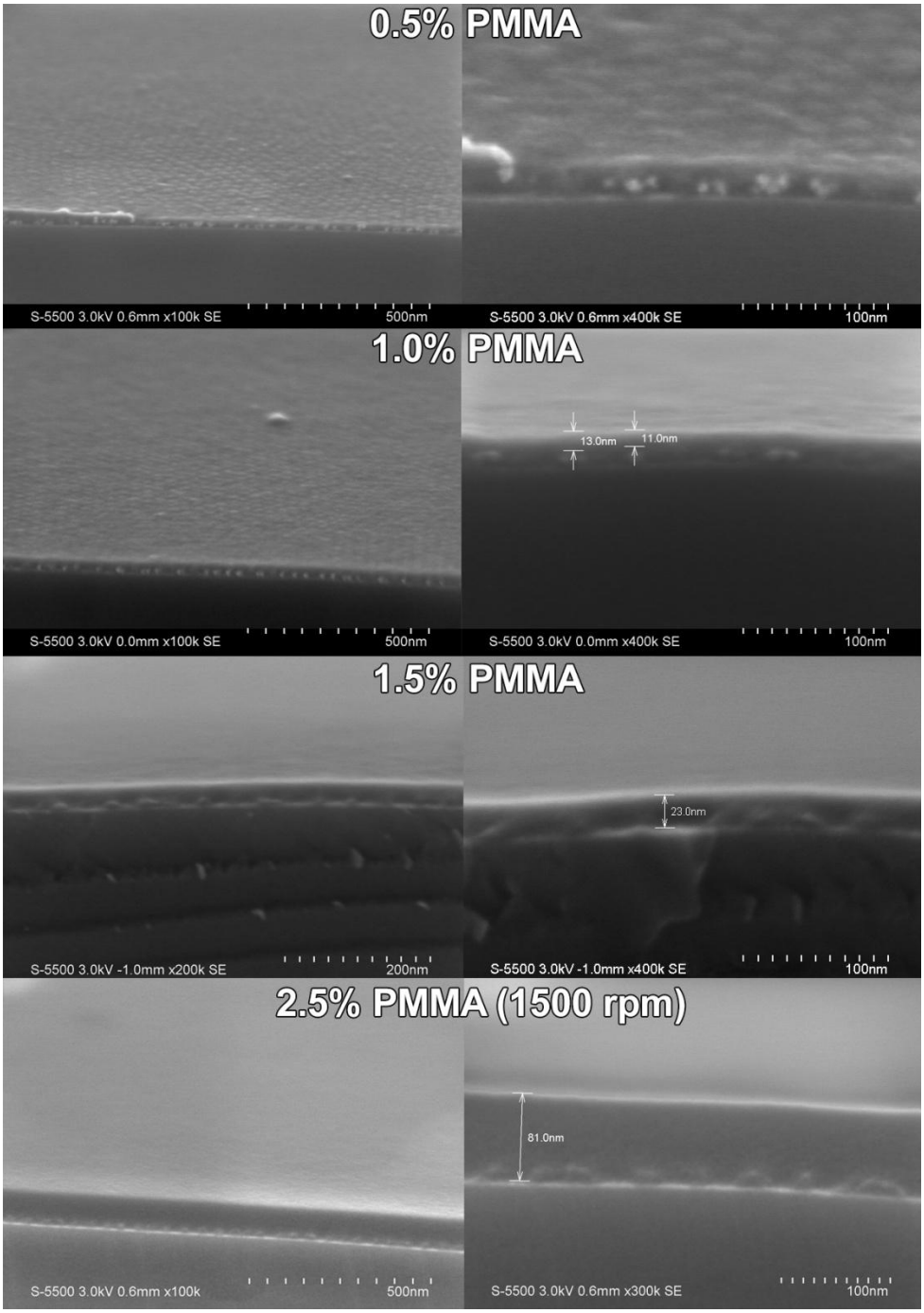

Figure 3.14 SEM images showing the cross sections of PMMA layers at various concentrations spin coated on silicon substrate. Spin speed is 4000rpm unless otherwise stated.

A 4nm layer of chromium is evaporated on spin-coated PMMA layer using ebeam deposition, followed by a 25nm Au layer. The PE layers of PDDA, PSS, and ACH are deposited on Au layer using the same procedure mentioned earlier, followed by deposition of 200nm PS nanospheres on top. The sample is etched in an Oxford Instrument Plasma Lab 80+ ICP-RIE system. Figure 3.15a and b show the result after 2 mins and 3 mins of 50W argon etch respectively. There is clear sign of nanodisk formation under the PS nanospheres, but a layer remains between the nanodisks and the QD clusters in PS-b-PMMA template. After 3 mins of argon etch, more of the PS nanospheres are etched away, but the layer above QD clusters appears to be similar in going from 2 mins to 3 mins of argon etch. Figure 3.15c and d show the result after 1 min and 3 mins of oxygen etching respectively, for a sample that has already been argon etched for 2 mins. Even in going from 1 min to 3 mins of O_2 etching, the layer above QD clusters does not appear to be further etched. This is in stark contrast to the O_2 etching result from PS-b-PMMA template since it only takes 10s at 10W to etch away most of the polymer. This indicates that the layer above QD clusters consists of Au/Cr. Given that most of Au is etched away in 2 mins but the layer looks similar with 2 mins and 3 mins of Ar etching, it is likely that the remaining layer is mostly Cr. A literature search confirms that Cr is much more resistant to Argon RIE than Au[96], and a forward power of a few hundred watts is needed to significantly etch away Cr.

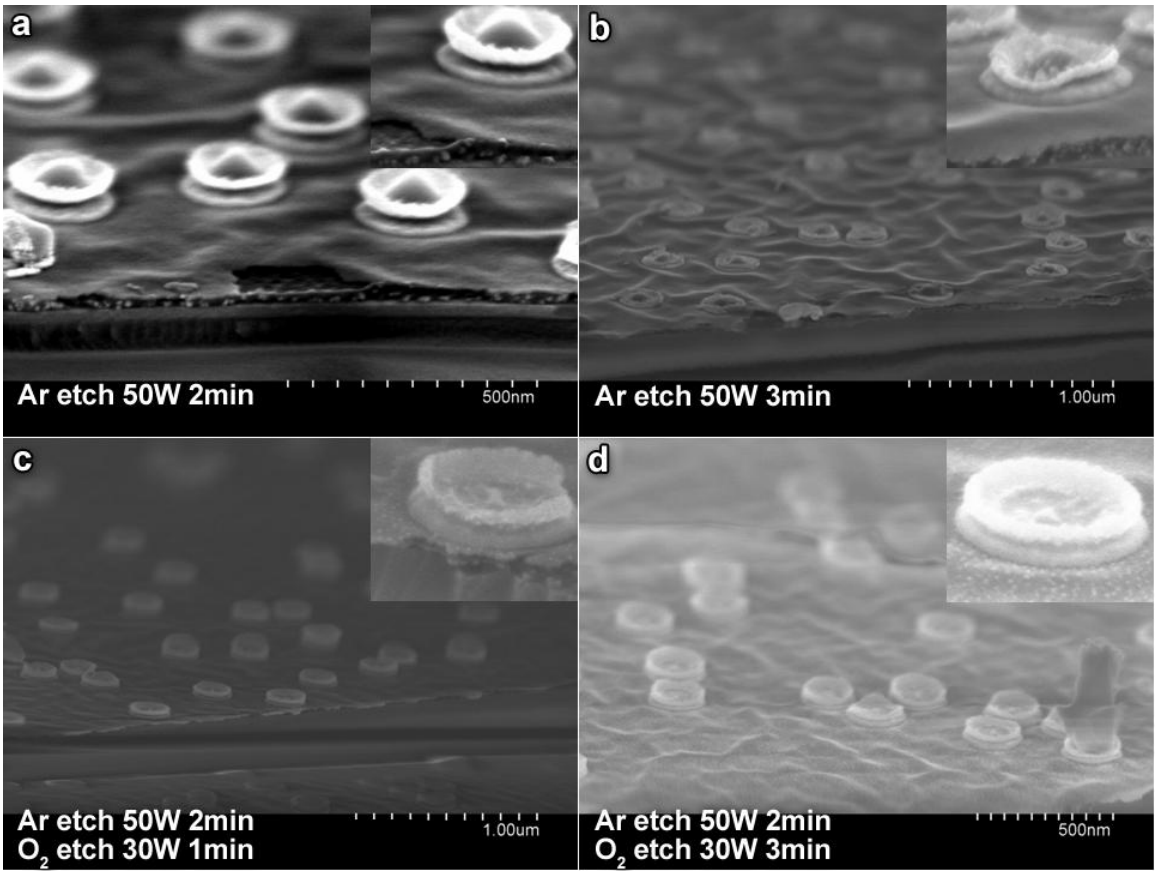

Figure 3.15 200nm PS nanospheres deposited on Au/Cr/PMMA/QD clusters after a) 2 mins of 50W Ar etch, b) 3 mins of 50W Ar etch, c) 2 min of 50W Ar etch and 1 min of 30W O_2 etch, and d) 2 mins of 50W Ar etch and 3 mins of 30W O_2 etch.

Cr layer appears to be the reason why Ar etch cannot completely remove materials on area not covered by PS nanospheres. Therefore, the same fabrication steps are repeated without Cr deposition. The schematic of the fabrication is summarized in figure 3.16a. Figure 3.16b and c show the uniform QD clusters after capillary force assembly. Figure 3.16d and e show the cross section of the sample after deposition of PS nanospheres. Going from top to bottom, figure 3.16d shows the thickness of each layer: PS spheres, Au layer, PMMA layer, PSPMMA template, and QD clusters. The

nanospheres are approximately 100-200nm apart edge to edge from each other as observed by SEM. The area not covered by PS nanospheres is etched by argon ion using with 50W forward power for 4 minutes to produce an ordered array of plasmonic Au nanodisks on QD clusters, separated by a PMMA spacer layer. Figure 3.16f and g show the cross section of samples after argon etching. The residue of un-etched PS nanospheres is visible from the SEM images for 200nm PS spheres. Figure 3.16g shows that the area not covered by PS nanospheres was removed by argon etching. The Au nanodisks fabricated after argon etching had thickness of about 20nm and diameters of approximately 210nm.

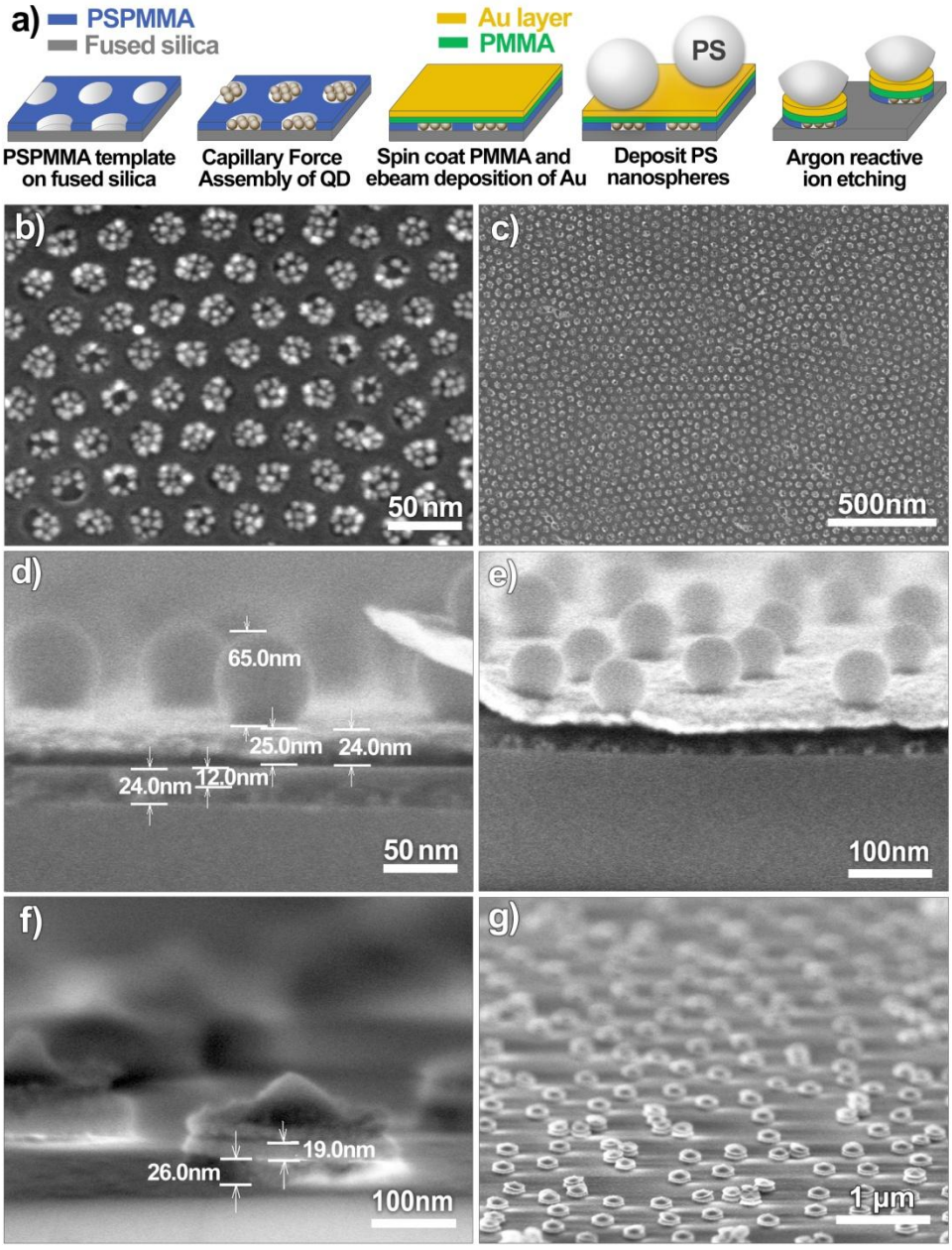

Figure 3.16 a) Step by step fabrication of Au nanodisks covered QD clusters. b), c) SEM images showing QD clusters assembled inside PSPMMA template on a silicon substrate. d, e) from top to bottom: PS nanospheres, Au layer, PMMA layer, PS-b-PMMA template and QD clusters. f) Au nanodisks (lighter) covering QDs clusters within the PS-b-PMMA template (darker), separated by a spacer layer of PMMA. PS nanospheres are not completely etched by Argon ion. g) large area SEM image showing that QDs and polymer were removed on area not covered by PS nanospheres.

3.2.2 Double-layer nanodisks

Fabrication with scheme B from figure 3.12 produces an array of Au nanodisks covering the QD clusters. It is conceptually viable to combine scheme A and B by first fabricating a layer of Au (without Cr) below QD clusters using the steps in scheme A and then follow the steps in scheme B. Here the fabrication of plasmonic double-layer nanodisks coupled with QD clusters is explored and presented. Starting with a piranha-cleaned fused silica substrate, Au is evaporated using e-beam deposition on the substrate. E-beam deposition provides a finer control on deposition rate and more uniform deposition over thermal evaporation. To achieve well phase-separated PS-b-PMMA film, a neutral surface energy layer is needed under PS-b-PMMA film. This is typically done using a random copolymer of PS and PMMA monomer units (PS-r-PMMA). A thin layer of silicon oxide (SiO_2) is deposited on Au layer in order to anchor the PS-r-PMMA layer with its hydroxyl termination. The SiO_2 layer is deposited using plasma-enhanced chemical vapor deposition (PECVD). Briefly, PECVD introduces silane (SiH_4) and nitrous oxide (N_2O) gases into the deposition chamber and their chemical reaction happened in the plasma phase. N_2O acts as the oxidant as oxygen is too aggressive as an oxidant for SiO_2 film growth. The final composition (Si:O) of the SiO_2 layer depends on the ratio of the gas mixture.[97] A few nm thick smooth film of SiO_2 is deposited at 200^{o}C on Au. From this point on, the substrate can be treated as the starting substrate for scheme B and the same procedure of spin-coating and thermal annealing of PS-r-PMMA and PS-b-PMMA produce microphase separated PMMA cylinder within a PS matrix. Figure 3.17a shows topography of SiO_2 deposited on Au. The measured root mean square (rms)

roughness is ~0.8nm. The resulting PS-b-PMMA template fabricated on SiO_2 shows minor defects but overall well phase-separated nanoholes in the PS matrix. This demonstrates the feasibility to fabricate double-layer nanodisks coupled with QD clusters, with the tunability of having different metals for the two layers.

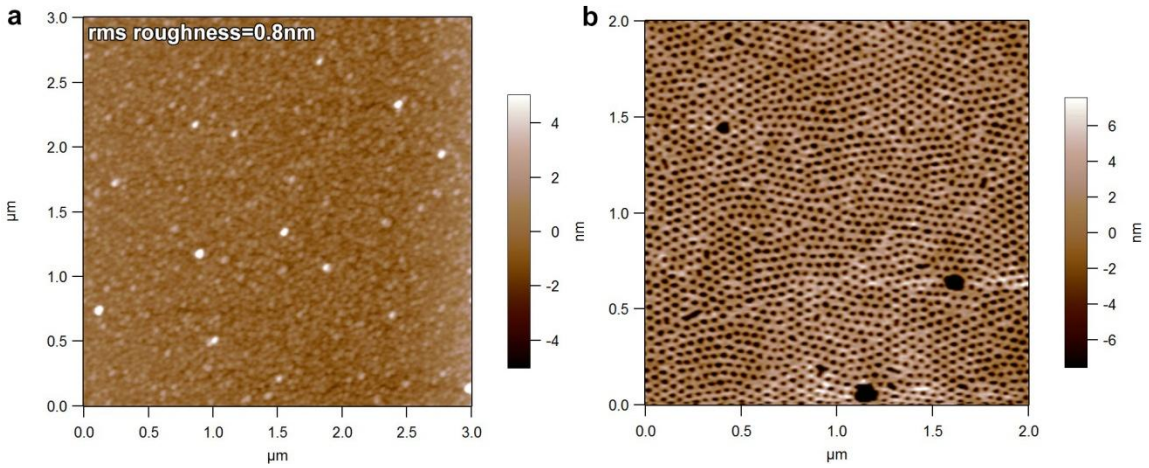

Figure 3.17 AFM images of a) SiO_2 layer on Au and b) PS-b-PMMA template on deposited SiO_2 after UV cross-linking and acetic acid etch.

Chapter 4: Anomaly large red shift of Lead Selenide quantum dots due to polarization effect

Reproduced with permission from

Wolcott, A.; Doyeux, V.; Nelson, C. A.; Gearba, R.; Lei, K. W.; Yager, K. G.; Dolocan, A. D.; Williams, K.; Nguyen, D.; Zhu, X. Y. *J. Phys. Chem. Lett.* **2011**, *2*, 795.

A. Wolcott designed the project. V. Doyeux conducted the absorption measurement. C. Nelson supplied one size of PbSe quatum dots. R. Gearba helped with the GIWAXS measurement.

Within a thin film of QDs, one can in principle control the strength of QD-QD interaction by varying the length (thus, the inter-QD distance). Colloidal QDs are usually synthesized with insulating capping molecules that lead to poor inter-QD coupling in QD solids. Removing or replacing these insulating capping molecules with short and/or conjugated ones in thin film has been shown to dramatically increase electrical conductivity. It is commonly observed that when a close-packed QD solid is formed from a colloidal QD solution, there is a red shift in the first exciton transition in the optical absorption spectra.[27-28, 44, 98-100] Further red shift of the excitonic absorption peak is also observed as the inter-QD distance decreases due to the exchange of long capping molecules by shorter ones. [27-28, 44, 98-100] While there have been attempts at correlating such red shifts with electronic coupling strength, excitonic red shifts can also result from varying polarization effects (i.e., solvatochromism) due to changes in the local dielectric

environment[101][102] and to exciton delocalization among neighboring QDs[103]; the latter is better known from studies on molecular J-aggregates.[104][105]

There have been a number of studies on the excitonic red shift in QD solids. Letherdale and Bawendi investigated CdSe QDs in solvents of different dielectric constants and in solid thin films; they attributed the small excitonic red shift (~2-4 meV) in CdSe solids to solvatochromism based on a polarization model of a core-shell-medium structure.[106] Most recently, Frederick and Weiss reported large optical shifts of up to 220 meV when they exchanged oleic acid (OA) ligands with phenyldithiocarbamate; they attributed the red shift to delocalization of the hole wave function on the QD into the ligand.[107]

A number of excitonic peak shift studies have focused on Pb-chalcogenide semiconductors, characterized by narrow band gaps, large bulk exciton Bohr radii, and large dielectric constants. Talapin and Murray studied thin films of PbSe QDs (8 nm) and showed an increase in electrical conductance by 10 orders of magnitude when they removed the insulating OA capping molecules by treatment with hydrazine.[98] The drastic increase in electrical conductivity strongly suggested inter-QD electronic coupling for the closely contacting PbSe QDs; this conclusion was also corroborated by the 20 meV red shift in the first exciton absorption peak upon the removal of OA. Nozik and co-workers examined PbSe QD thin films upon a variety of chemical treatments and correlated increased electrical conductivity and red shift in the first exciton absorption peak with decreasing inter-QD distance.[28][44] Williams et al. examined the optical red shift as a function of OA ligand removal using a hydrazine treatment in two-dimensional

(2D) PbSe QD films; they observed maximum optical shifts of 82 and 157 meV for 6 and 4 nm QDs, respectively, and attributed these to inter-QD electronic coupling.[99] Despite all of these suggestions for strong electronic coupling, the contribution of polarization effect to the excitonic red shift remains uncertain.

To quantitatively investigate the contribution of polarization, a model system of PbSe QD thin films of 0.5-2.5 monolayer thickness is used to perform a series of ligand exchange reaction with various alkanedithiol capping molecules, HS-$(CH_2)_n$-SH. Inter-QD distance in real and reciprocal space are quantified using scanning electron microscope (SEM) imaging and grazing-incidence wide-angle X-ray scattering (GIWAXS), respectively. As expected, the inter-QD distance decreases with the length of the capping molecules, while the magnitude of the red shift in optical absorption increases. A quantitative comparison of a thin film of monodispersed QDs (6.2 nm) with that consisting of isolated QDs (6.2 nm) embedded in a matrix of smaller ones (4.8 nm) at a ratio of 1:35 was carried out, and the study shows that the dominant contribution to the optical red shift following the exchange of OA capping molecules by ethanedithiols comes from polarization effects (88%), with a minority (12%) attributed to resonant electronic and exciton coupling. More importantly, this polarization effect is more than one order of magnitude larger than theoretical predictions based on the dielectric polarization effect for QDs in an idealized spherical quantum well model.

4.1 Experimental

4.1.1Synthesis of PbSe quantum dots capped with oleic acid

PbSe QDs capped with oleic acid was synthesized under air-free conditions using the hot injection method[98][108]. In a scaled down reaction, 2.5 g of Lead oxide, PbO , 35.15 mL of 1-octadecene (ODE, Fluka , 95%), and 9.05 mL of oleic acid (OA) were added to a 150 mL 3-neck flask, connected to a Schlenk line via a refluxing column and a T-bore adapter. A septum and a temperature probe were attached to the other two openings of the 3-neck flask. In a glovebox filled with nitrogen, 21 mL of trioctylphosphine (TOP) was added to 1.6581 g of 99.99 % Se shot and stirred vigorously for 24 hours. After complete dissolution of the Se/TOP solution, 0.150 μL of diphenyl phosphine (DPP) was added to the stirring solution. PbO, ODE and OA were heated to 60 °C under a N_2 atmosphere and then degassed to a pressure of ~30 mTorr for 75 minutes. Water was generated in the chelating of oleic acid with Pb atoms as oxygen atoms reacted with hydrogen atoms from OA. The temperature of the solution was raised to 295 °C under a N_2 flow and the resulting solution was optically clear and colorless. The solution was kept stirring by a magnetic stir bar in a steady laminar flow. The temperature was then lowered to 160 °C, and the Se/TOP-DPP solution was injected quickly using a glass syringe with low gauge needle through the septum; this resulted in an immediate color change to a dark solution, indicating nanoparticle nucleation and growth. Growth was stopped after 30 seconds by removal of the heating mantle, injection of 30mL of cooled octane (0 °C) and submersion of flask into an ice bath. PbSe QD

transfer was facilitated by a cannula to a Schlenk flask using positive pressure (N_2) from the Schlenk line, and immediately placed into a glove box. Purification of PbSe QDs included precipitation, decantation and re-suspension, which all took place inside the glovebox. PbSe QDs solution was split between multiple glass vials. For every 15 mL of raw PbSe QDs, 25 mL of a precipitation solution of methanol, butanol and ethanol in a 1:1:2 ratio was added. The precipitated solutions were centrifuged at 2000 rpm for 30 minutes and the supernatant was discarded. Re-suspension of the QDs was done with anhydrous hexane and the cleaning procedure was repeated twice more. PbSe QDs were then dried with a stream of N_2 and weighed to produce PbSe QD solution dispersed in hexane with known concentration. The optical absorption spectrum for PbSe QD in solution showed the first excitonic peak at 0.727 eV with a full width at half-maximum (fwhm) of 45 meV. A combination of SEM and scanning transmission electron microscopy (STEM) was used to determine the size distribution, which corresponds to an average particle diameter (D) of 5.4±0.3 nm. TEM also revealed the crystal lattice of the single crystal PbSe QDs.

4.1.2 Fabrication and ligand exchange of PbSe thin film

Oleate-capped PbSe QD thin films were prepared via a dip-coating method on oxide-terminated silicon waveguide surfaces. A desired QD coverage on the silicon oxide surface was obtained by varying the withdraw speed in the dip-coating process and verified the surface coverage by atomic force microscopy and SEM. To exchange the OA (C18) capping ligands, the QD thin film coated samples were immersed in 0.1 M

solutions of the corresponding alkanedithiol molecules in anhydrous acetonitrile for 1 min, followed by acetonitrile rinsing and drying in an inert N2 environment. The following alkanedithiols were used in this study: octanedithiol (HS-C_8H_{16}-SH, abbreviated as C8), hexanedithiol (HS-C_6H_{12}-SH, or C6), pentanedithiol (HS-C_5H_{10}-SH, or C5), butanedithiol (HS-C_4H_8-SH, or C4), propanedithiol (HS-C_3H_6-SH, or C3), and (HS-C_2H_4-SH, or C2). As a control, complete removal of capping molecules was performed with hydrazine.

4.1.3 Structural characterization of PbSe thin film using SEM and GIWAXS

The structure of PbSe QD thin films was measured in real space by SEM and those in reciprocal space by GIWAXS. Figure 4.1 shows SEM images of approximately one monolayer (ML) coverage of PbSe QDs (5.4±0.3 nm diameter) on SiO_2 substrates before and after ligand exchange reactions with alkanedithiols. The as-deposited QD film with OA capping was highly ordered in a hexagonal close packed arrangement. Replacing the OA capping molecules with alkanedithiols of decreasing length introduced more and more disorder and the breaking up of large QD islands into smaller domains. As expected, the inter-QD distance decreased as the length of the capping molecules became shorter. On the basis of autocorrelation function analysis on SEM images (figure 4.2) corresponding to the different treatments, inter-QD distance is expressed as a function of capping molecule length. The inter-QD distances were also obtained from GIWAXS analysis at both submonolayer (~0.5 ML) and multilayer (~2.5 ML) coverage.

Figure 4.3a shows, as a function of capping molecule length, the measured inter-QD distance (d), which is defined as the edge-to-edge nearest-neighbor distance based on a QD diameter of 5.4±0.3 nm. Here, the data obtained from GIWAXS analysis (0.5 and 2.5 ML) and those from autocorrelation function analysis of SEM images (0.5 ML) were in good agreement. For films of OA-capped QDs, the average inter-QD distance of d =2.6±0.3 nm was far less than the ~4 nm value expected from the sum of two completely packed OA capping layers. In contrast, the OA insulating shell on each QD is not believed to be close-packed, resulting in significant intercalation of the OA molecules between adjacent QDs. When the OA molecules were replaced by alkanedithiols, the inter-QD distance was consistently longer than the fully stretched molecular length in each case, indicating that intercalation rather than a single molecule bridge dominates. The solid line is a linear fit to the data and serves as guide to the eye. Optical red shifts as a function of capping molecule length in Figure 4.3b will be discussed later.

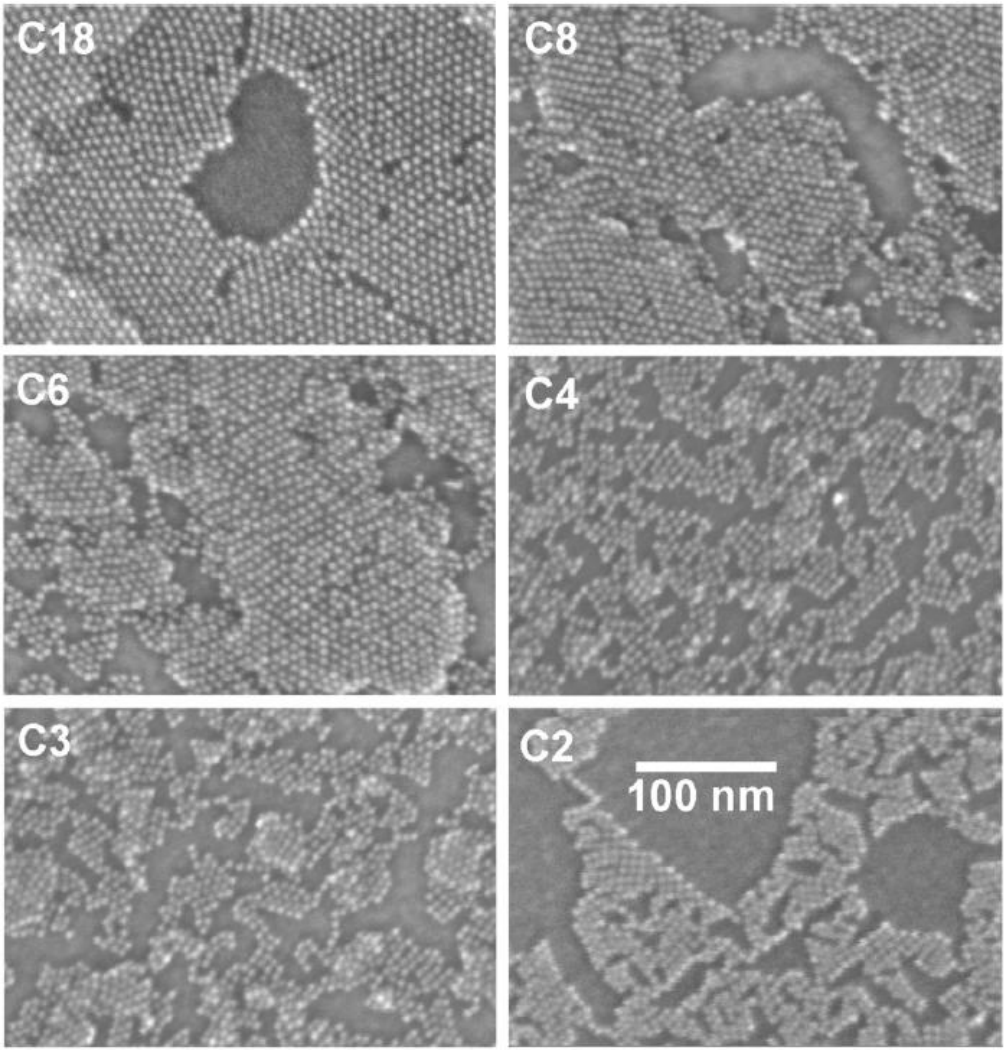

Figure 4.1 SEM images of ~1 ML of PbSe QDs (D = 5.4±0.3 nm) on SiO2 substrates. The QDs are capped with the following molecules: oleic acid (C18), octanedithiol (C8), hexanedithiol (C6), butanedithiol (C4), propanedithiol (C3), and ethanedithiol (C2).

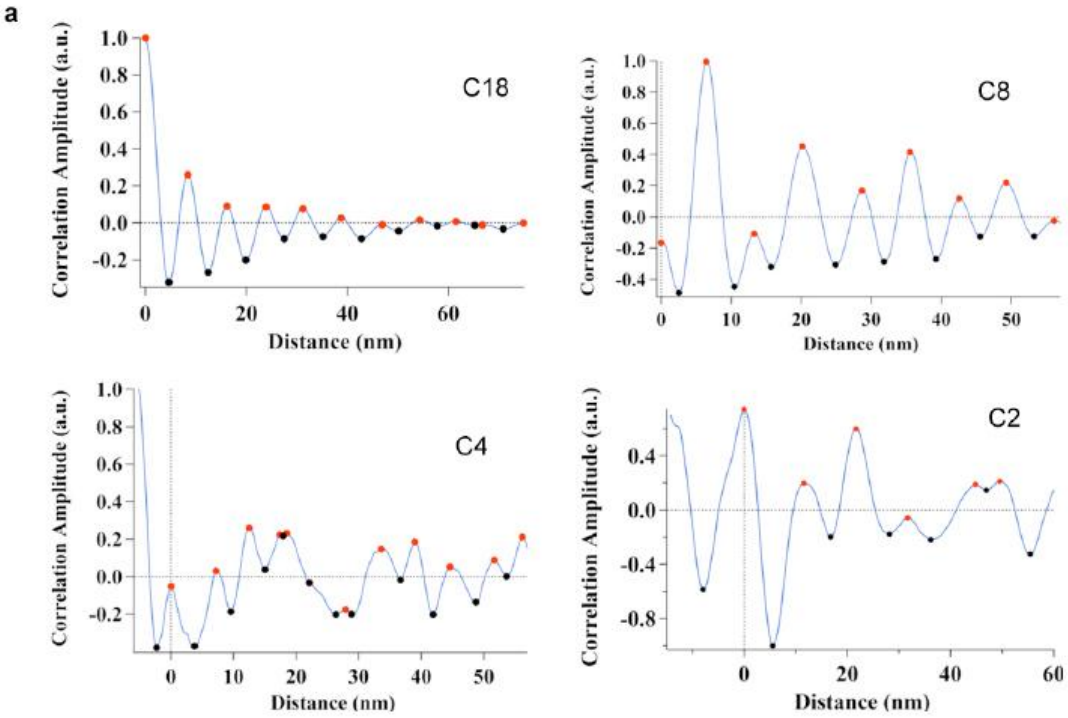

Figure 4.2 a) Correlation functions of submonolayer coverage PbSe QD films obtained from SEM images with OA (C18) and C8, C4 and C2 dithiol capping molecules.

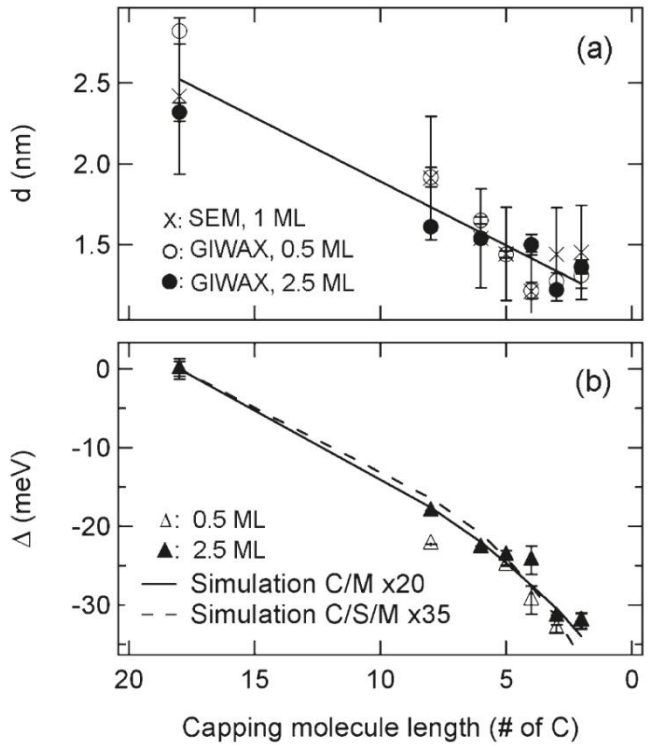

Figure 4.3 a) Inter-QD distance (edge-to-edge) as a function of capping molecule length (number of-C-units) obtained from autocorrelation functions of SEM images (crosses, submonolayer) and GIWAXS analysis (open and solid circles for 0.5 and 2.5 ML, respectively). The solid line is a linear fit; (b) red shifts in the first exciton transition with respect to the OA-capped QDs as a function of capping molecule length (number of –C-units) for 0.5 (open triangles) and 2.5 ML (solid triangles) QD coverage. The solid and dashed lines (scaled by x20 and x35, respectively) are simulations, as detailed below.

4.2 Result and discussion

4.2.1 Red shifts in optical absorption

Having established the structure and inter-QD distance in the QD thin films, the red shift in excitonic transitions can be correlated with inter-QD distance. Figure 4.4

shows the attenuated total reflectance-Fourier transform infrared (ATR-FTIR) absorption spectra of a multilayer (~2.5 ML) and a submonolayer (~0.5 ML) QD film with OA and dithiol capping molecules. The nearly complete exchange of OA molecules by alkanedithiols was verified by the decreasing C-H stretch vibrational peak area with decreasing alkanedithiol molecular length; within experimental uncertainty, the integrated C-H peak area was proportional to the number of -CH2 -repeating units in each molecule. While the first or second exciton peak of the OA-capped QDs showed little change going from the solution phase in tetrachloroethylene (TCE) to the solid film, there was an obvious red shift as the capping molecule length became shorter. Peak position and fwhm were obtained by fitting the first exciton absorption peak with a Gaussian function. As a further control, ligand exchange reactions were also carried out with 1,2-ethanedithiol and 1-ethanethiol in TCE solution and observed shifts of much smaller magnitudes. Note that there is no measurable broadening of the exciton peaks after the exchange reactions with the thin film samples.

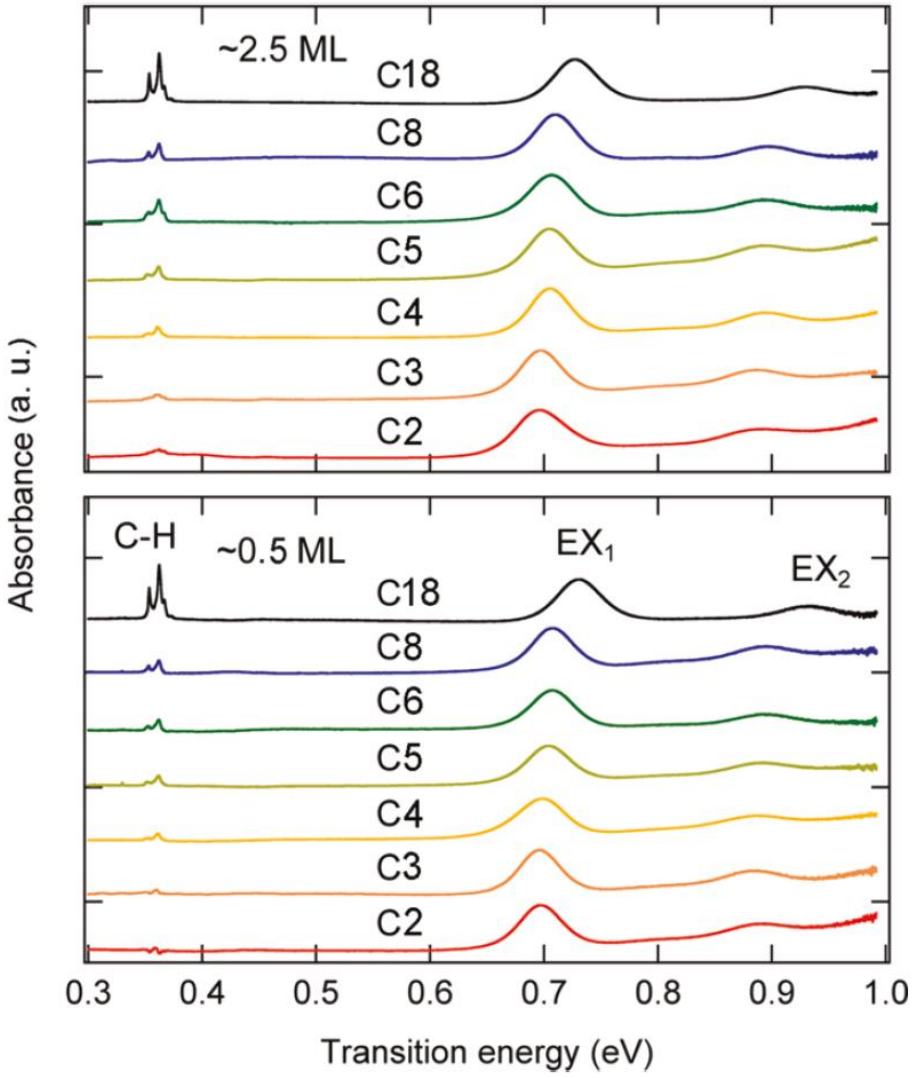

Figure 4.4 ATR-FTIR spectra for multilayer (~2.5 ML, upper) and submonolayer (~0.5 ML, lower) QD thin films with OA and various dithiol capping molecules. EX1 and EX2 denote the first and the second exciton transitions, respectively. C-H:C-H stretch vibrational transitions.

Figure 4.3b shows the measured red shift in the first exciton transition as a function of the length of the capping molecules. Within experimental uncertainty, there was no significant difference between the data set for the monolayer (open triangles) and

that of the multilayer (solid triangles). No measurable difference was found using different substrate materials (SiO_2 and TiO_2) in the magnitudes of red shift. The dashed and dotted lines are theoretical predictions, as detailed later. The magnitude of the observed red shift in submonolayer films increased linearly from -22.3±0.1 meV for 1,8-octanedithiol (C8) to -32.1±1 meV for 1,2-ethanedithiol (C2). Note that for the same ligand exchange reaction, the magnitude of excitonic red shift increases with decreasing QD size, as shown in figure 4.5.

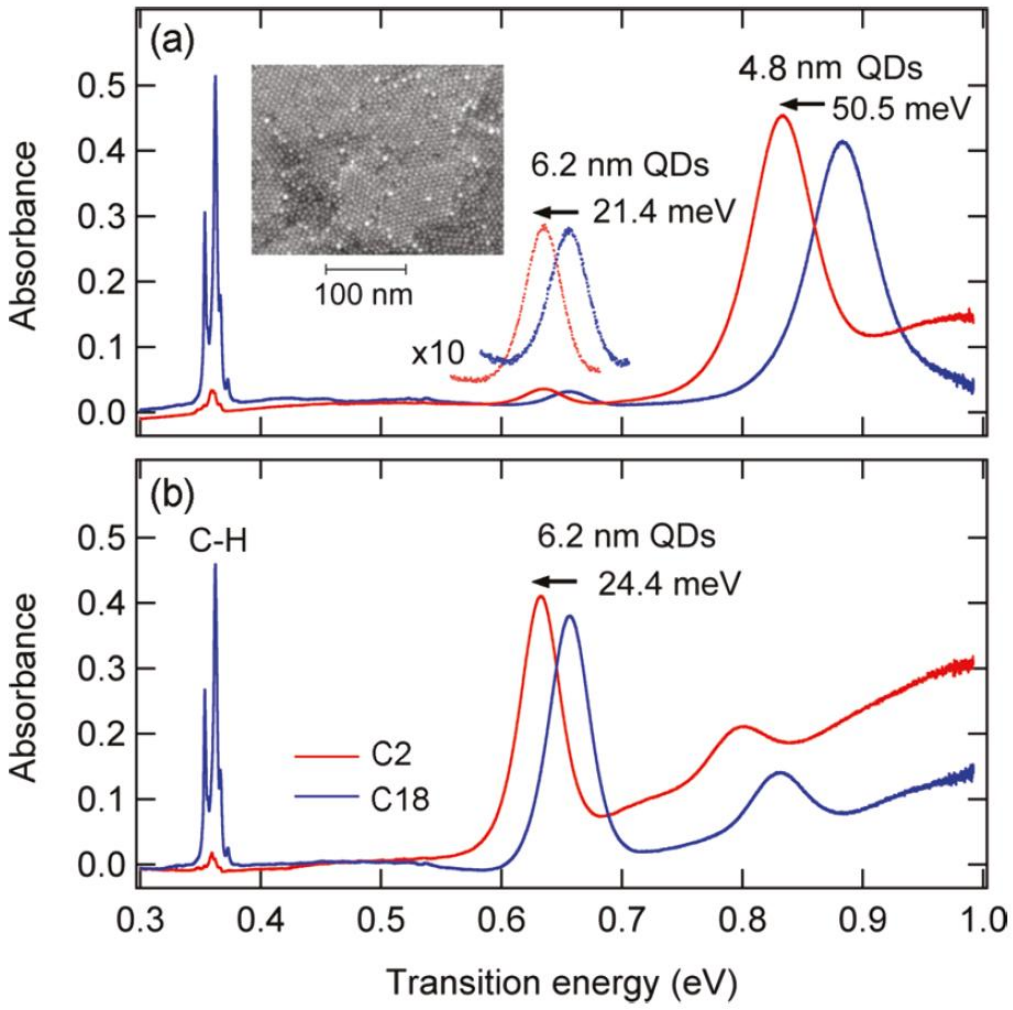

Figures 4.5 (a) Optical absorption spectra for C18- and C2-capped QD films (~2ML film) of large QDs (D = 6.2 nm) embedded in a matrix of smaller ones (D = 4.8 nm) at a number ratio of 1:35. The first exciton peak of the large QDs red shifts by -21.4±0.3 meV, while that of the small QDs red shifts by -50.5±0.5 meV. The inset shows the SEM image of the mixed QD film; the minority of large QDs (bright spots) are completely isolated in the matrix of small QDs. (b) Optical absorption spectra for a ~2 ML film of large QDs (D = 6.2 nm) before (blue) and after (red) ligand exchange reaction of C18 by C2. The first exciton red shifts by -21.4±0.3 meV after the ligand exchange reaction.

Contributions from electronic coupling, excitonic coupling (transition dipole-transition dipole coupling), and polarization effects are all expected to increase with

decreasing inter-QD distance. In order to distinguish contribution from these effects, the optical red shift for isolated QDs was measured in a non-resonant matrix of smaller QDs.

Figure 4.5a shows the optical absorption spectra for large QDs (D = 6.2 nm) embedded in a matrix of smaller ones (D = 4.8 nm) at a number ratio of 1:35 before and after the exchange reaction of OA by C2. Note that due to variations in QD growth time, the diameter of the large QDs used here is not the same as that in other figures. SEM imaging (inset to Figure 4.5a) of the film prepared from the cryo-evaporation procedure, which involves submerging sample in liquid N_2 and then putting under vacuum, clearly shows that the minority of large QDs are completely isolated in the majority of small QD matrix. While the optical red shift of -50.5±0.5 meV is expected upon ligand exchange for the small QD matrix, it is surprising that a large red shift of -21.4±0.3 meV is also seen for the large QDs that are completely isolated from each other. For comparison, the film of the same large QDs prepared in the pure form, Figure 4.5b, shows an optical red shift of Δ = -24.4±0.3 meV upon the ligand exchange reaction. SEM was also used to examine the bimodal QD solid after the C2 treatment to ensure QD isolation, as shown in Figure 4.6.

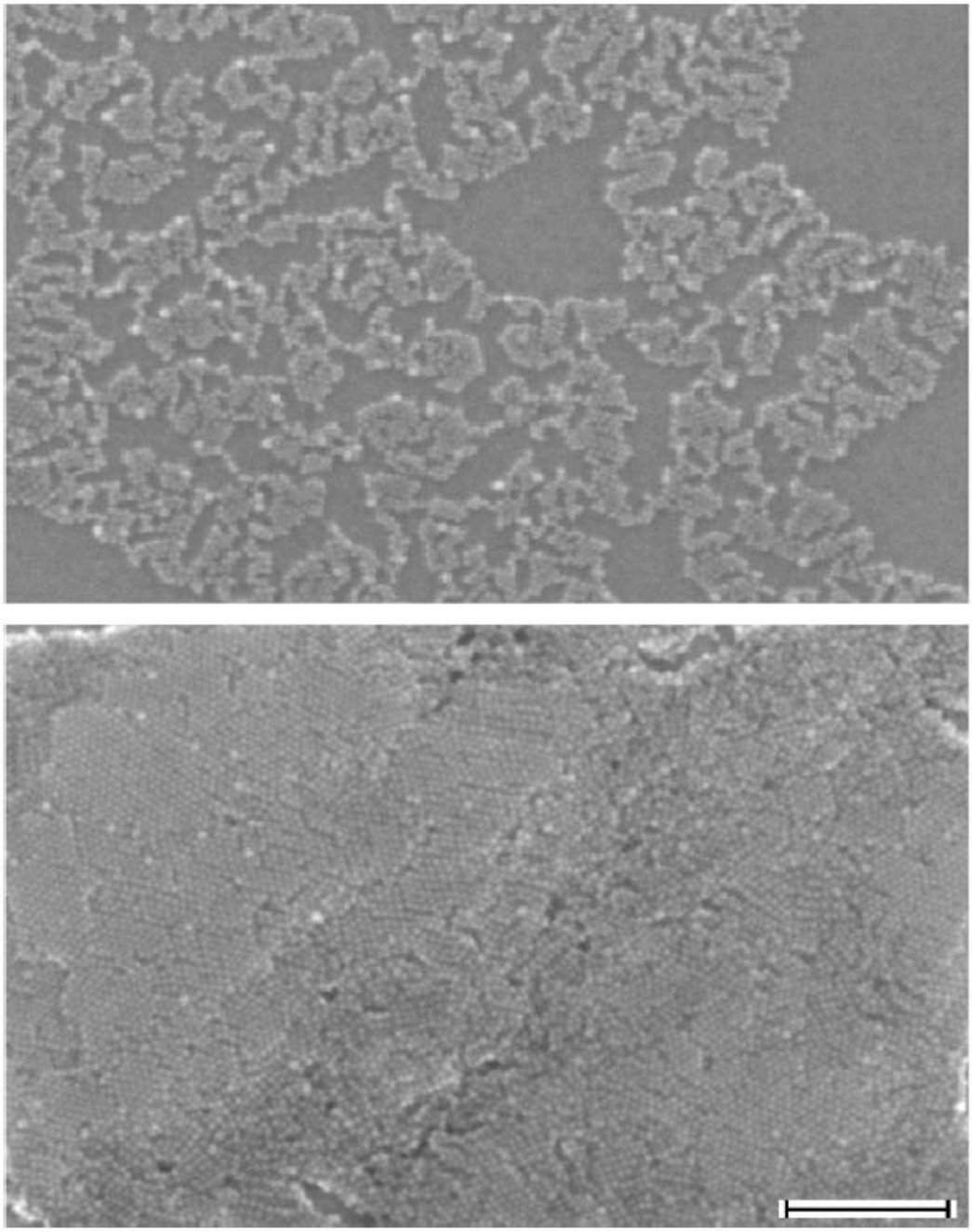

Figure 4.6 SEM images in sub-monolayer (upper) and multilayer (lower) region of a bimodal QD thin film consisting of large QDs (D = 6.2 nm) embedded in a matrix of smaller ones (D = 4.8 nm) at a number ratio of 1:35. The images were taken after the OA capping molecules were replaced by C2 dithiols. The bright spots in each image were the large QDs. The scale bar was 100 nm.

For each large QD embedded in a matrix of smaller ones, its $1S_e$ and $1S_h$ electronic energy levels are not in resonance with those of the smaller QDs in the matrix. The optical transition dipoles are also not in resonance with those of the matrix, as clearly shown by the large separation between the first exciton transitions of the two different size QDs (Figure 4.5a). Any off-resonance transition dipole-transition dipole coupling is weak due to the lack of oscillator strength of the smaller QDs at the transition energy of each larger QD. In addition, inherent disorder of the QDs in terms of size, shape, and transition dipole orientation also minimizes any coupling between transition dipole moments. Kagan et al. showed that for monodispersed CdSe QD solids, transition dipole-transition dipole interaction was responsible for long-range resonance energy transfer and red shifts in fluorescence spectra, but not in optical absorption spectra.[109][110]

The observed red shift of Δ = -21.4±0.3 meV for the large QDs (D = 6.2 nm) in a bimodal film cannot come from inter-QD electronic or transition dipole coupling. Therefore this red shift must be attributed to changes in polarization effect when the C18 ligands are replaced by C2. In view of this conclusion from the bimodal sample, the additional red shift of -3 meV in Figure 4.5b can be attributed to resonant electronic interaction and/or exciton delocalization (transition dipole-transition dipole coupling) in the nearly monodispersed sample (D = 6.2±0.4 nm). Thus, 88±2% (=21.4/ 24.4) of the total excitonic red shift (Δ = -24.4±0.3 meV) in Figure 4.5b is attributed to the polarization effect. The remaining 12±2% in red shift maybe attributed to inter-QD electronic coupling and/or transition dipole-transition dipole coupling.

4.2.2 Anomalously large polarization effect

The red shift in optical absorption from the polarization effect (solvatochromism) can be understood as follows. Within the two-band nearly free-electron model for a QD, the optical gap or the first exciton transition energy is given by[101][111]

$$E_{EX}^{1} += E_g^0 + E_e^{kin} + E_h^{kin} + E_{Coul}^{dir} + E_e^{Pol} + E_h^{Pol} + E_{e,h}^{Pol} \quad (1)$$

where E_g^0 is the bulk transport gap, $E_e^{kin}(E_h^{kin})$ is the kinetic energy of the electron in the conduction band (hole in the valence band) due to quantum confinement, E_{Coul}^{dir} is the Coulomb attraction between the electron and the hole within the QD, $E_e^{Pol}(E_h^{Pol})$ is the polarization stabilization energy, that is, the attraction between an electron (hole) in the QD and its image charge of opposite sign in the dielectric medium surrounding each QD, and $E_{e,h}^{Pol}$ is the polarization destabilization energy, that is, the repulsion between an electron (hole) and the image charge of the hole (electron). The first four terms are related only to the QD, while the last three terms are determined by the dielectric medium surrounding each QD. Previous studies have shown that the total polarization correction to the first exciton energy is given by[112]

$$\delta = \frac{\pi e^2}{2\varepsilon_1 \varepsilon_0 a} \sum_{l=1}^{\infty} a^{2l+1} A_l \int_0^1 [j_0(\pi x)]^2 x^{2l+2} dx \quad (2)$$

where j0(z) = sin(z)/z is the spherical Bessel function, a is the QD radius, ε_1 is the optical dielectric constant of the QD material, ε_0 is the vacuum permittivity, and e is the fundamental charge of the electron. For a QD surrounded by a dielectric shell of thickness b (equal to half of the inter-QD distance, d) of dielectric constant ε_2 and further embedded in a medium of dielectric constant ε_3, that is, the core/shell/medium (C/S/M) model, the term A_l is given by

$$A_l = \frac{(l+1)}{a^{2l+1}} \frac{a^{2l+1}(\varepsilon_2 - \varepsilon_3)[\varepsilon_1 + l(\varepsilon_1 + \varepsilon_2)] + b^{2l+1}(\varepsilon_1 - \varepsilon_2)[\varepsilon_3 + l(\varepsilon_2 + \varepsilon_3)]}{a^{2l+1}(\varepsilon_1 - \varepsilon_2)(\varepsilon_2 - \varepsilon_3)l(l+1) + b^{2l+1}[\varepsilon_2 + l(\varepsilon_1 + \varepsilon_2)][\varepsilon_3 + l(\varepsilon_2 + \varepsilon_3)]} \quad (3)$$

Here ε_2 is taken to be the optical dielectric constant of the capping molecules in the condensed phase; when *b* is set to zero, this reduces to the simpler core/medium (C/M) model of a QD core embedded in a medium with the effective dielectric constant, ε_3.[113] ε_3 can be calculated from the effective media approximation (EMA) assuming that the QD film is made of close-packed spheres, each consisting of a QD core (ε_1) covered with a capping molecular shell (ε_2) of thickness d/2. Either *fcc* close packing with space filling factor of *f* = 0.74 or random close packing with f = 0.63 can be used in calculating ε_3.[114] The ligand exchange of C18 capping molecules by the shorter C2 decreases *b* and increases ε_3, leading to a different stabilization energy. The shift in the first exciton transition is then given by $\Delta = \delta' - \delta$, where δ and δ' are values before and after ligand exchange, respectively.

Δ values are calculated from equations (2) & (3) using the inter-QD distances obtained from the fit to experiment data (solid line in Figure 4.3a) and fcc close packing based on the C/S/M and C/M models. The calculated optical red-shifts are compared with experimental results in Figure 4.3b. While both models qualitatively describe the trend in the optical red-shift as a function of inter-QD distance or capping molecule length, they fail to account for the magnitude of the optical redshifts. For example, the C/S/M model predicts optical redshifts that are ~35x smaller than experimental values; for the C/M model, the calculated values are ~20x smaller.

The calculated red-shifts from polarization model are an order of magnitude smaller than the observed excitonic red-shifts. An explanation is given in terms of the sensitivity of the polarization stabilization energy (i.e., the last three terms in equation 1) to the spatial distribution of the electron or hole wavefunction. For a point charge located from an interface between two phases with different dielectric constants, the polarization energy (charge-image interaction energy) scales inversely with distance to the interface; for a planar interface, the scaling factor is $(4z)^{-1}$ (z is distance to the interface).[115] The sensitivity of the polarization energy is also reflected in the calculated Δ as a function of QD size, Fig. 5. For the same capping molecule-shell thickness (or bare QDs with no molecular shell), the magnitude of the calculated first exciton red-shift increases nearly exponentially with decreasing QD size. As the QD becomes smaller, the spatial distribution of the electron (hole) wavefunction lies closer to the interface with the dielectric medium, leading to a larger polarization effect. The calculated |Δ| for bare dots at D = 5.4 nm is 5.9 meV, which is one order of magnitude smaller than the experimental

value obtained for thin films of PbSe QDs (D = 5.4 nm) with hydrazine treatment. Note that the insensitivity of the red-shift to QD film thickness (1-3 ML) and substrate material (SiO2 and TiO2) suggests little influence of the substrate polarizability on the observed red-shifts.

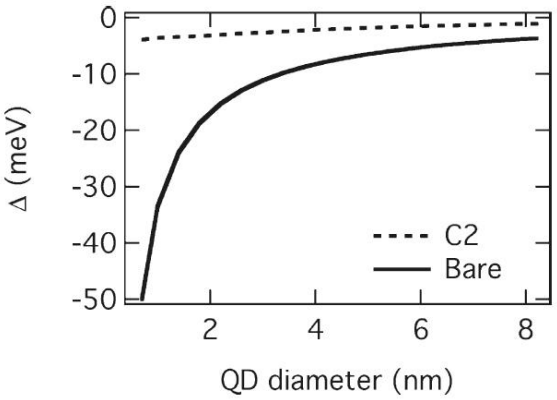

Figure 4.7 Red-shifts with respect to the OA capped QDs in the first exciton transition calculated as a function of the diameter of the QD core for C2 capped (dashed) and bare PbSe QDs in the C/M model.

There are a number of possible causes for $|\psi|^2$ of the electron (hole) to lie much closer to the QD surface than what is predicted by the spherical quantum well model. The first is that the actual boundary condition is much smoother than the step-like potential profile used in the model; in a different context, a smooth boundary condition is believed to be essential in explaining carrier dynamics in QDs.[116] The second cause may be the perturbation approach in deriving eqns (2) and (3); as an example, the magnitude of the optical red shift reaches almost 10% of the optical band gap for PbSe with hydrazine treatment, casting doubts on the adequacy of the perturbation treatment. The third cause may result from deviation of the QD shape from the spherical model, leading to partial

localization of the electron (hole) wave function to one part of the QD, as seen previously in scanning tunneling spectroscopy measurements.[117] All of these factors can lead to much larger polarization effects than what are predicted from the spherical quantum well approximation.

In PbSe QD solid thin films, the replacement of OA ligands by shorter alkanedithiols molecules leads to increasing red shifts in the exciton peak position as ligand length and inter-QD distance decrease. A dominant contribution (~88%) to the observed red shift is due to changes in polarization of the dielectric environment surrounding each QD, with only a minor effect (~12%) attributed to inter-QD electronic and/or exciton (transition dipole-transition dipole) coupling. The observed red shifts are more than 1 order of magnitude larger than theoretical predictions based on the dielectric polarization effect for spherical QDs. The failure of the idealized spherical quantum well model calls for more advanced theories in treating the QD polarization problem.

Chapter 5: Template assembly of quantum dot molecules

Reproduced with permission from

Lei, K. W.; West, T.; Zhu, X.-Y. *J. Phys. Chem. B* **2013**, *117*, 4582.

T. West helped with fabricating the PbSe QD molecule samples.

The magic of chemistry lies in the myriad possibility of achieving new and controlled physical properties from the assembly of a relatively small number of building blocks, i.e., atoms. This fundamental principle is now being explored in nanomaterials research. Semiconductor nanocrystals or quantum dots (QDs) have been referred to as artificial atoms because of their discrete energy levels near the band edges. An exciting prospect is to assemble them into artificial molecules[49] to achieve new and controlled electronic structures and charge/energy transfer dynamics for a wide range of applications, e.g., electronics and optoelectronics. Alivisatos and coworkers[50][51] and Buck et al.[52] have attempted the direct synthesis of QD molecules based on bonding of QDs with inorganic interconnections. A more general approach is to assemble artificial molecules from colloidal QDs. A number of studies reported the assembly of colloidal QDs into close packed QD films or superlattices.[45-47] To increase inter-QD electronic interaction, one can remove or replace the long and insulating capping molecules by shorter or conjugated ones,[27,44, 98] but this approach leads to QD solids or clusters with random size distributions. For clusters of colloidal QDs to behave as artificial molecules,

there must be not only inter-QD electronic interaction, but also well-defined and controlled size distribution.

In this study geometric templates and capillary force assembly is used to achieve large-scale synthesis of colloidal QD molecules. This assembly strategy is based on the presence of capillary force acting on nanoparticles when the solvent front of the colloidal solution is dragged across a surface with defined topographic features to provide geometrical confinement.[86] Capillary force assembly has been used to assemble polystyrene spheres, gold nanoparticles, and gold nanorods onto templates with array of trenches and holes,[84-85, 87, 118] but the sizes of particles demonstrated so far have been larger than the sizes of semiconductor QDs (≤ 10 nm) and forming ordered assemblies of sub-10 nm particles has been shown to be difficult.[54] To overcome this difficulty and achieve large-scale assembly of artificial molecules from QDs with diameter < 10 nm, we use block-copolymer templates and control the surface topographical features (heights) to the scale of the diameter of QDs. We find the latter to be essential to the successfully assembly of sub-10 nm QDs.

5.1 Experimental

5.1.1 Synthesis of PbSe capped with oleate

The protocol used to synthesize the PbSe quantum dots with oleate (OA) capping ligands is detailed in section 4.1.1. All chemicals and solvents were used as purchased without further purification unless otherwise stated. The general synthetic route followed the hot-injection method performed in a standard Schlenk line setup under N_2 flow.

Monodispersed QDs with diameter around 5 nm and the first exciton absorption peak at 768.5 ± 1 meV in tetrachloroethylene (TCE) solution were characterized on a Hitachi S5500 scanning electron microscope (SEM) in scanning-transmission electron microscopy (STEM) mode and a Cary 5000 UV-Vis-NIR spectrometer. Fig. 1 shows STEM image and absorption spectrum of PbSe-OA (dia. 5.0 ± 0.3 nm) in TCE.

5.1.2 Fabrication of polymer template

All polymer samples were purchased from Polymer Source (Montreal, Canada). Three polymers were used: two poly (styrene-b-methyl methacrylate) (PS-b-PMMA) block-copolymers, with number averaged molecular weight of 68000(PS)/33500(PMMA) and 37500(PS)/18000(PMMA), and a random copolymer, poly (styrene-co-methyl methacrylate) with hydroxyl termination (PS-r-PMMA) and 62 mole % PS content. A 1 wt % solution of PS-r-PMMA in toluene was spin-coated on a clean silicon substrate (500 μm thick p-type silicon substrate) to obtain neutral surface energy. The PS-r-PMMA film was thermally annealed in a vacuum oven at 180 ^{o}C for 72h and then rinsed with toluene. For the block-copolymer coating, a 1wt% solution of PSMMA in toluene was spin-coated on the PS-r-PMMA layer and thermally annealed in a vacuum oven at 180 ^{o}C for 24h. The morphology of annealed film was studied by atomic force microscope (AFM) in tapping mode. The AFM tip used was purchased from AppNano (Santa Clara, CA) with resonance frequency between 47-76 kHz. After thermal annealing, the PS-b-PMMA sample was exposed to 254 nm UV light for 9h to cross-link the styrene within the PS block and to degrade the PMMA block. The sample was rinsed with glacial acetic

acid and 18 MΩ ultrapure water to remove the PMMA domains, leaving the PS matrix on the substrate. To achieve a PS film thickness suitable for the assembly of QDs into small clusters, the acid etched SMMA film was etched by O_2 plasma in an Oxford Instruments Plasma Lab 80+ system (Oxford Instruments, UK) at 10 W RF power to remove part of the PS matrix and the PS-r-PMMA layer.

5.1.3 Assembly of QD clusters and ligand exchanges

The PbSe QDs were assembled inside a glovebox by dipping the polymer template into a 10 mg/mL hexane solution of PbSe QDs with a mechanical dip-coater and withdrawing at a speed of 1mm/s. The as-synthesized PbSe QDs have oleic acid as their capping ligands. Chemical treatment with 1,2-ethanedithiol (95%, Acros Organics) was performed by dipping the polymer template with assembled QD clusters in a 1M solution of 1,2-ethanedithiol in acetonitrile. The chemicals were used as received without further purification. The polymer template was then dipped in pure acetonitrile for 1 minute to wash away residual ligand molecules.

5.1.4 Absorption spectroscopy

We obtained the absorption spectra of assembled PbSe QDs clusters capped with OA or EDT using attenuated total reflectance Fourier transform infrared (ATR-FTIR) spectroscopy. Specifically, crystalline silicon ATR waveguides were cut and polished to the shape of a parallelogram with a 45° bevel on both ends (32 mm x 10 mm x 1 mm). After template formation and QD assembly, we carried out ATR-FTIR spectroscopy

measurements inside a glovebox using a Nicolet 6700 FTIR-NIR spectrometer equipped with a Mercury-Cadmium-Telluride detector.

5.2 Result and discussion

Oleic acid capped PbSe of two different sizes are assembled into QD molecules with two PS-b-PMMA templates made from PS:PMMA = 68K:33.5K and PS:PMMA = 37.5K:18K polymer ratio. The larger PbSe QD with lower 1st exciton energy is abbreviated as QD^A and the smaller PbSe QD is abbreviated as QD^B. For QD^A, the average number of QDs per molecule is 9 (QD^A_9) for PS:PMMA = 37.5K:18K and 17 (QD^A_{17}) for PS:PMMA = 68K:33.5K. For QD^B, the average number of QDs per molecule is 13 (QD^B_{13}) for PS:PMMA = 37.5K:18K and 19 (QD^B_{19}) for PS:PMMA = 68K:33.5K.

Having established the assembly of QD molecules, the next step is to study their properties. For clusters of QDs to behave like artificial molecules, there needs to be inter-QD electronic interaction. The as-synthesized PbSe QDs are capped with oleic acid molecules that prevent inter-QD electronic interactions. Enhanced electronic coupling between QDs are expected when the long and insulating OA molecules are replaced with much shorter ones, such as 1,2-ethanedithiol (EDT) used in this experiment. Indeed, such a ligand replacement process is known to result in much increased electric conductivity in thin films of PbSe QD solids, as well as significant red-shift in the first exciton peak.[44][27] Figures 5.1a & 5.1b show SEM images of the QD assemblies after the OA ligands have been replaced by EDT molecules in the ligand exchange reaction. The

hexagonally arranged QD clusters remain intact, with inter-QD distance within each cluster slightly decreased,[119] as also evident in the lower image resolution.

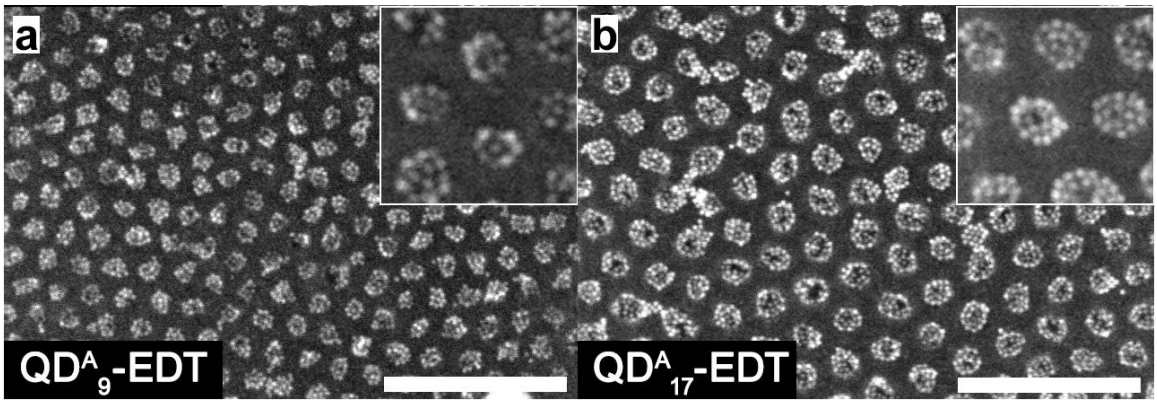

Figure 5.1 a) SEM images of PbSe QDs assembled in template with a) PS:PMMA = 37.5K:18K and b) PS:PMMA = 68K:33.5K polymer ratio after ligand exchange with EDT.

The bottom spectra in Fig. 5.2a show absorption spectra of a monolayer PbSe QD thin film before (blue) and after (red) the ligand exchange reaction (from OA to EDT). The first exciton peak is shifted by -31.6 ± 1 meV (from 764.0 ± 1 meV) following the ligand exchange reaction. While the red-shift is attributed entirely to enhanced inter-QD electronic coupling in an earlier study,[99] recently it was found that, in addition to inter-QD electronic coupling, a major contribution to the red-shift may come from an anomalously large polarization of the dielectric environment surrounding each QD.[119]

To explore the difference in electronic properties between a QD film and QD molecules, the excitonic red-shift in monolayer thin film is compared to those in the QD clusters of the two different size distributions (QD^{A}_{9} & QD^{A}_{17}) on the two block-copolymer templates. For clusters of OA capped QD^{A}s, the first exciton peak is at 769.0

± 1 meV, independent of cluster size. The slight blue-shift of the first exciton peak in OA capped clusters, as compared to that in the monolayer film, could be explained by the decrease in polarization of the dielectric environment in the former. For both QD^A_9 & QD^A_{17}, exchanging OA with EDT results in red-shifts of 40.0 ± 1 meV. The same ligand exchange from OA to EDT was carried out with QD^B to probe how the increased extent of quantum confinement affects the optical red-shift. As shown in figure 5.2b, a film of QD^B red shifted more than a film of QD^A, from 32 ± 1 meV to 40 ± 1 meV. This is in agreement with a previous study[119] that smaller QDs give a larger red shift. The same trend of larger red shift with clusters comparing to films is also observed with QD^B_{13} and QD^B_{19}. Within experiment uncertainty, there is not a significant difference in the red shift between the two cluster sizes for QD^A (9 ± 2 and 17 ± 3) and QD^B (13 ± 2 and 19 ± 3). However, comparison with the two different sizes of QDs confirms that there is a significant enhancement in red shift for clusters of smaller QDs. Note that replacement of OA ligands by EDT also leads consistently to a slight decrease in the width of the first exciton absorption peak, from 32 ± 1 meV to 30 ± 1 meV. This decrease in peak width is not understood and deserves further investigation.

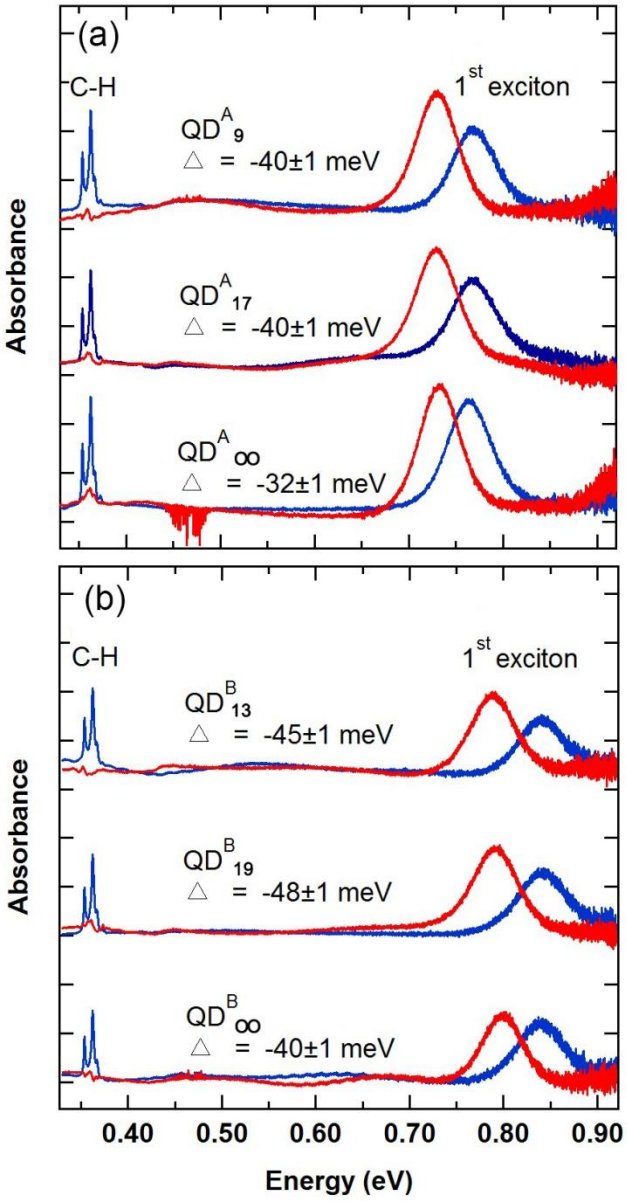

Figure 5.2 a) Absorption spectra of three PbSe QD^A samples: monolayer film (bottom), QD clusters with average sizes of 17±3 (middle) and 9±2 (top) with OA (blue) and EDT capping (red) molecules. The ligand exchange reaction (from OA to EDT) is characterized by a decrease in the absorbance of the C-H stretch vibrational peak and a red-shift in the first exciton transition. The three sets of spectra are scaled and shifted for clarity. b) The corresponding film and cluster samples for QD^B.

To investigate the dependence of this excitonic red shift on the coupling between neighboring QDs, a series of ligand exchange was done with QD^A and QD^B films and clusters as a function of inter-QD spacing. In addition to 1,2-ethanedithiol (EDT), we also use 1,4-butanedithiol (BDT) and 1,8-octanedithiol (ODT) to replace the oleic acid capping ligands. Using capping molecules with different lengths allows the control of inter-QD spacing.[119] Figure 5.3 summarizes the result, with each ligand represented by the respective number of carbon atoms between the thiol groups. The red shifts upon ligand exchange are consistently larger for the clusters (QD^A_9, QD^A_{17}, QD^B_{13}, QD^B_{19}) than for the respective 2D films (QD^A_{oo} and QD^B_{oo}). Moreover, a comparison of QD^B with QD^A shows larger red-shifts for smaller QDs with stronger quantum confinement.

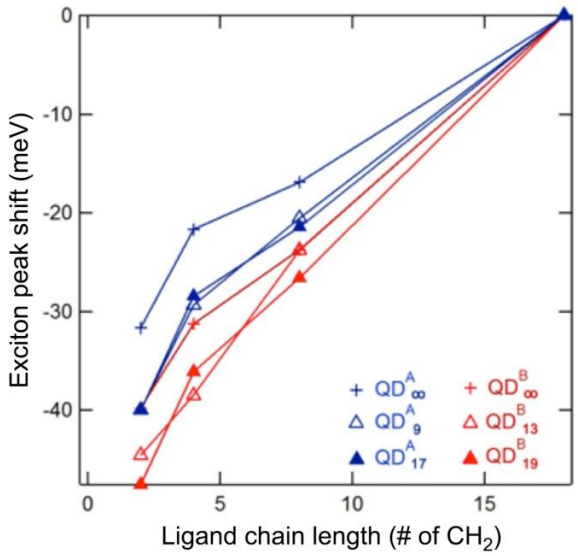

Figure 5.3 Redshifts in the first exciton transition as a function of the capping ligand length (in number of C atoms in the linking molecules). Blue and red symbols are for PbSe QDs with diameters of 5.0 nm and 4.5 nm, respectively.

Although the number of interacting particles in clusters containing a few to a few tens of QDs is expected to be much smaller than that in a monolayer film, the magnitude of the red-shift is actually 20% larger than that in the monolayer. The larger red-shift may be attributed to the shorter inter-QD distance following the ligand exchange reaction (from OA to EDT) in a cluster (QD_9 or QD_{17}) than that in a monolayer film, due to the presence of geometric frustration in the later. In a solid thin film consisting of a large number of interacting QDs, decreasing the inter-QD distance by exchanging long ligand molecules with shorter ones will inevitably build up strain, which counters the chemical bonding force that is bringing the QDs closer. The presence of strain build up is evident by the large number of cracks observed in the QD film following exchange reaction.[119] In contrast, this kind of strain is absent for a small QD cluster, thus allowing the inter-QD distance to decrease to the optimal value determined by chemical bonding (between the bi-functional EDT molecule and QD surfaces) and van der Waals interactions.

As mentioned earlier, the excitonic red-shift in PbSe QDs upon ligand exchange can be attributed to a local electronic effect, including enhanced inter-QD electronic interaction and an anomalously large polarization effect, which may result from the spatial localization of the exciton wavefunction to a part of the real nanocrystal, making it very sensitive to changes in local dielectric environment. Such a local electronic/polarization effect argues for the molecular characteristics of the QD clusters. This argument is supported by previous measurements as there was little excitonic red-shift upon ligand exchange reaction for isolated QDs (i.e., QD_1).[99] This result, along with findings on 2D QD clusters presented here, draws attention to such critical question:

what is the size limit of quantum dot molecules where such localized electronic/polarization effects are present? To answer this question experimentally, it is necessary to reduce the size of QD_n to, e.g., QD_2, QD_3, etc. There are significant experimental challenges in doing so because of the limitations of the block-copolymer approach in generating high quality patterns of much smaller cylinder sizes than those presented in this experiment. In addition, capillary force assembly becomes increasingly difficult as the size of the nano-wells decreases.[54]

The large-scale 2D assembly of artificial molecules with controlled sizes from 5 nm PbSe QDs is realized using capillary force assembly in nanoscale templates formed from block-copolymer patterns. A crucial factor in successful assembly is a low aspect ratio (depth to diameter) of the nano holes on the templates, with the depth comparable to the size of the QDs. The method developed here using capillary force assembly is generally applicable to nanoparticles with different sizes and shapes. Optical absorption spectra of the QD clusters with the short EDT capping molecules reveal enhanced and local inter-QD electronic interaction.

Chapter 6: Plasmonic enhancement of Förster Resonance Energy transfer (FRET) from plasmonic nanodisks

Localized surface plasmon resonance (LSPR), the collective oscillation of free electrons from noble metal nanoparticles, is finding applications in a wide range of fields, from biosensing to solar energy conversion. LSPR has enabled single-molecule level detection through techniques such as surface-enhanced Raman spectroscopy (SERS).[120] The presence of LSPR concentrates electromagnetic field to a length scale much smaller than the diffraction limit, thus allowing the transport and manipulation of electromagnetic fields at the nanometer scale, e.g., in devices like plasmonic nanolasers [121-123] and white light emitting nanoantennas.[124] In these applications, LSPR is coupled with a light emitter and non-radiative energy transfer (NRET) can occur between the emitter and LSPR. Another strongly distance-dependent energy transfer mechanism is Förster resonance energy transfer (FRET) between two quantum emitters. FRET is also a non-radiative energy transfer mechanism based on the dipole-dipole coupling between a FRET donor and an acceptor and FRET rate has $1/d^6$ distance (d) dependence. FRET has found applications in light harvesting and emitting systems,[125][126] and the strong distance dependence of FRET is utilized in biological to develop nano-scale rulers.[127] If the strongly distance-dependent plasmonic effect on emitters and intrinsic FRET between donor and acceptor can be combined in a synergistic way, it can enable new ways of enhancing and transporting electromagnetic radiation on the nano scale. To explore this possibility, the coupling of FRET between donor and acceptor to LSPR is investigated

with a model system obtained from template assisted assembly and nanosphere lithography.

Because of the strong distance dependence of both plasmonic effect and FRET, a major barrier to a reproducible and systematic study is fabricating a highly controllable system with well-defined and uniform separation between different components, down to a few nanometers or less. Previous studies[64,66, 68] on the subject of plasmonic effects on FRET have largely depended on layer-by-layer (LbL) assembly to successively deposit monolayers of metal nanoparticles as the plasmonic nanostructure and quantum dots (QDs) as FRET donors and acceptors. However, there is often a lack of clear structural characterization and it is not clear about the degree of homogeneity and order within each monolayer and at the interfaces of different layers. In order to accurately correlate experimental measurements with structural parameters of the LSPR-FRET system, a well controlled and well characterized sample is essential. To meet this challenge, a process is developed to fabricate highly ordered LSPR-FRET hybrid structure consisting of an array of Au nanodisks and a single layer of CdSe quantum dots (QDs) as donors and acceptors, separated by a thin layer of poly(methyl methacrylate) (PMMA). Each step of the fabrication is characterized using cross-sectional scanning electron microscopy (SEM) in order to correctly interpret experimental results from photoluminescence intensity and lifetime based on observed structure.

6.1 Experimental

The fabrication process of Au nanodisks on CdSe QDs with PMMA separation layer is summarized in figure 3.16 in section 3.2.1 and the experimental details is included below.

6.1.1 Fabrication of CdSe QD clusters using polymer template on fused silica substrate

A 1 wt % solution of PS-r-PMMA with 62 mole % PS content in toluene was spin-coated at 4000 rpm on a piranha-cleaned fused silica substrate (500 μm thickness). The substrate was thermally annealed in vacuum at 180 ^{o}C for 72 h. The PS-r-PMMA coated fused silica substrate was subsequently rinsed with toluene to remove excess PS-r-PMMA. To prepare the ordered nano-template, a 1 wt % solution of PS-b-PMMA block-copolymer in toluene, with number averaged molecular weight (M_n) of 68000(PS)/33500 (PMMA), was spin-coated onto the PS-r-PMMA covered fused silica substrate and annealed at 180 ^{o}C for 24 h to prepare a hexagonally ordered array of PMMA cylinders in the PS matrix (~20 nm cylinder diameter and ~40 nm inter-cylinder separation). To remove the PMMA block, the block copolymer film was exposed to 254 nm UV light (~8 watts) from a Spectroline UV lamp (Westbury, NY) for 7.5 h and was rinsed with glacial acetic acid and then DI water. The polymer film was further etched to form the nanohole array by oxygen plasma using an RF power of 10 W for 8 s to achieve the optimal depth to diameter ratio (~1:3) of holes for capillary assembly of QD clusters. The morphology of polymer template was characterized by atomic force microscopy (AFM).

To assemble QD clusters on the polymer template, polymer template was dipped into a hexane solution of CdSe QDs using a mechanical dip-coater. Two sizes of CdSe/ZnS core shell quantum dots (CdSe/ZnS QDs) capped with octadecyl amine (ODA) ligands were purchased from NN-Labs (Fayetteville, AR), with 1^{st} exciton absorption peaks at 540 nm (QD540) and 620 nm (QD620), respectively. The withdrawal speed was 1 mm/s and the concentration of QDs solutions was 5 mg/mL for both QD540 and QD620. The QD cluster assemblies were characterized using scanning electron microscope (SEM). The size of the QD clusters was controlled by the diameter of holes and was fairly uniform (9 ± 1 QD/cluster).

6.1.2 Fabrication of LSPR-FRET nanostructures

After QDs clusters were formed within the holes on the template, solutions of PMMA in ethyl acetate with various concentrations (0.5%, 1.0%, 1.5%,) was spin-coated at 4000 rpm to create a spacer layer with controlled thickness, in the range of 8 nm-20 nm. On top of the PMMA spacer layer, a thin film of gold (Au) was evaporated using an e-beam evaporator. To form an array of Au nanodisks, polystyrene (PS) nanospheres were used as a dry etch mask. The polymer template filled with CdSe QD clusters was successively immersed in three cationic and anionic polyelectrolyte solutions, poly(diallydimethylammonium chloride) (PDDA), Poly(sodium 4-styrenesulfonate (PSS), and aluminum chlorohydrate (ACH). The sample was rinsed with DI water after deposition of each polyelectrolyte. A sub-monolayer of negatively charged PS nanospheres (80 nm or 200 nm diameter) were deposited onto the polyelectrolyte coated

surface by immersing the sample in dilute solutions of PS nanospheres and then dried in the ambient. The areas not covered by PS nanospheres were etched by argon ions in a plasma etcher (Oxford Instruments Plasma Lab 80+ system) with 50 W RF power for 4 minutes to produce an ordered array of plasmonic Au nanodisks on QD clusters, separated by a PMMA spacer layer. The Au nanodisks fabricated after argon etching had thickness of about 20 nm and diameters of 212 ± 13 nm and 61 ± 3 nm for 200 nm and 80 nm PS spheres, respectively.

6.1.3 LSPR optical scattering and steady state photoluminescence measurement

The localized surface plasmon resonance (LSPR) of Au nanodisks was measured using white light with an optical microscope in bright field. The microscope was equipped with a monochromator and a spectrograph (Princeton Instruments, Acton). Au nanodisks on fused silica were formed by evaporating Au film on fused silica, followed by the same process of PS nanospheres deposition and argon ion etching. Background intensity (I_o) was obtained from the blank region of fused silica not covered by plasmonic nanodisks. White light from a xenon lamp passing through a bright field condenser and a 20X objective was absorbed or scattered by Au nanodisks and the transmitted light intensity (I) at each wavelength was recorded on the spectrometer. The extinction spectra was calculated from the equation $I(\lambda)=I_o(\lambda)e^{-\varepsilon(\lambda)x}$, and are plotted as ε versus λ, where ε is the extinction coefficient, λ is wavelength of incident light, and x is the fixed length of sample.

Steady state photoluminescence of all QD samples were collected using the same optical microscope. QDs were excited at around 400 nm using a 400±10 nm bandpass filter and a xenon lamp. Emission from QD passed through a 450 nm longpass filter before entering the monochromator and spectrograph.

6.1.4 Time correlated single photon counting (TCSPC)

Time correlated single photon counting (TCSPC) measurement was carried out with a Fluorolog3 (Horiba, Japan) fluorimeter. PL lifetime was collected at emission maxima of QD620 (636 nm) and QD540 (558 nm) using a NanoLED laser diode, emitting at 402 nm with a pulse width of ~300 ps and repetition rate of 1 MHz. PL decay curves were de-convoluted from the instrument response function (IRF) and fitted with a 3-exponential decay using the manufacturer supplied decay analysis software, DAS6.

6.2 Result and discussion

6.2.1 Surface plasmon peak of Au nanodisks

The Au nanodisks fabricated after argon etching had diameters of 212 ± 13 nm and 61 ± 3 nm for 200 nm and 80 nm PS spheres respectively. Figure 6.1a shows the extinction spectra of 61 ± 3 nm (lighter red) and 212 ± 13 nm (darker red) diameter Au nanodisks. The surface plasmon peaks are broad from Au nanodisks of both sizes. The peak positions are at ~640 nm and ≥ 710 nm, for Au nano-disks with diameters of 61 nm and 212 nm, respectively; these peak positions are comparable to values reported in a similar study.[10]

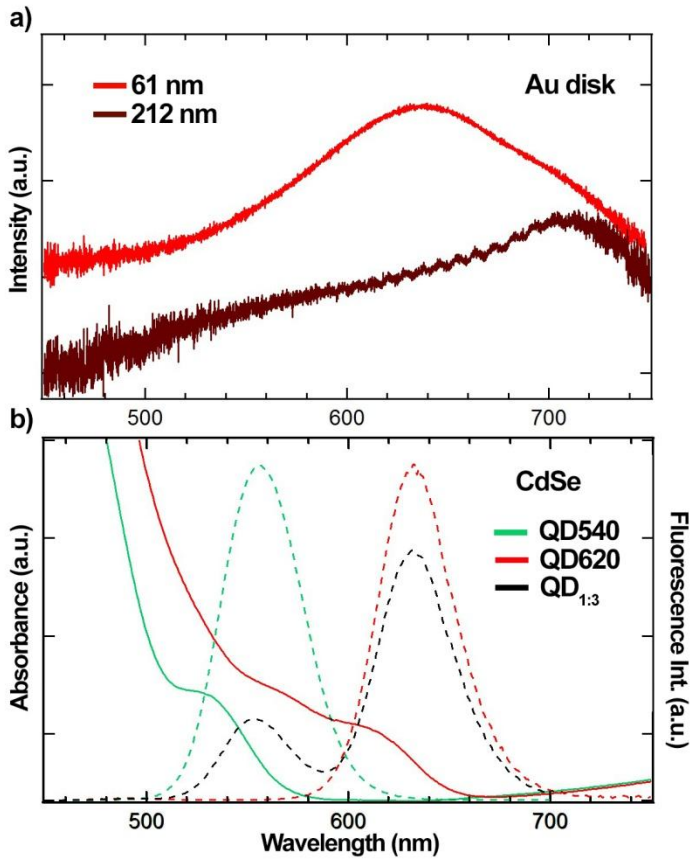

Figure 6.1 a) Scattering spectra of Au nanodisks made by 80 nm (lighter red) PS spheres and 200 nm (darker red) PS nanosphere masks. b) Absorption (solid) and emission (dotted) spectra of the two sizes of CdSe/ZnS QDs, QD540 (green) and QD620 (red) used in fabricating QD clusters. Black dotted curve is the emission spectra of $QD_{1:3}$ the 1:3 ratio mixture of QD540 to QD620, measured in solution.

While the wavelength of the surface plasmon peak decreases as the diameter of the Au nanodisk decreases, there is a limitation as to how far the surface plasmon peak of Au nanodisks can blue shift just by changing the diameter. It becomes an issue to fabricate Au disks with diameters smaller than 61 nm since it is more difficult to achieve a well-dispersed layer of PS nanospheres and the spheres would be etched away more

quickly as the size of the PS spheres decreases. Another noble metal like Ag would be required to move the plasmon peak to lower wavelength.[128]

6.2.2 LSPR coupled FRET nanostructures

A structurally well-controlled and tunable LSPR-FRET nanostructure provides the platform to study systematically how the position of surface plasmon peak affects energy transfer between plasmonic nanodisks and QDs given a defined separation distance. QD donor and acceptor are chosen based on the criteria that there needs to be strong overlap between the donor emission and acceptor absorption for efficient energy transfer. The donor and acceptor emission peaks also need to be clearly resolved for an accurate comparison of the emission peak area ratio. For this study, three sets of QD samples coupled with plasmonic nanodisks were examined. They consisted of having only QD540, only QD620, and a 1:3 ratio (by mass) mixed sample of QD540:QD620 ($QD_{1:3}$) within the holes of PS-b-PMMA template. Figure 6.1b shows the absorption and PL spectra of QD540 (green curves) and QD620 (red curves) in solution, as well as the PL spectrum of $QD_{1:3}$ in solution (black curve). As shown in figure 6.1, the surface plasmon peak from 212 nm Au nanodisks is at longer wavelength compared to the emission peak of the acceptor. The surface plasmon peak from 61 nm Au nanodisks is blue shifted by approximately 60 nm comparing with the 212 nm Au nanodisks, and it overlaps well with emission peak of acceptor. The stronger overlap with the emission of the donor and acceptor from 61 nm Au nanodisks is expected to lead to greater plasmonic coupling to the FRET process as well as to individual donors and acceptors.

6.2.3 Dependence of LSPR coupled FRET on spectral overlap

Figure 6.2a shows the steady state PL spectra of $QD_{1:3}$ without Au nanodisks, with 61 nm Au nanodisk, and with 212 nm Au nanodisks. All the spectra in figure 6.2a are normalized with respect to the donor peak so that the peak ratio between different samples can be compared by looking at the acceptor peak height. The two donor and acceptor peaks are fitted with an exponential modified Gaussian function to take into account the extra shoulder found in the lower energy side of the emission peak using Igor Pro, and the peak area ratio is calculated based on the fitted area of each peak. Peak ratio for $QD_{1:3}$ in solution (dotted black curve) is 3.2 and for $QD_{1:3}$ clusters in film (solid black curve) is 6.2. The peak ratio is distinctly higher for the samples with Au nanodisks than the sample without Au nanodisks. Among the Au nanodisks samples, 61 nm Au nanodisks (peak ratio = 11.2) shows a stronger enhancement of the acceptor emission than 212 nm Au nanodisk (peak ratio = 8.3).

Based on the known plasmonic effects of emission enhancement,[8] the increase in acceptor emission intensity can come from both intrinsic field enhancements from Au nanodisks and surface plasmon assisted FRET between donors and acceptors. Since the surface plasmon peak of 61 nm Au nanodisks overlaps more with the acceptor emission peak than that of 212 nm Au nanodisks, and both plasmon peaks overlap much more with acceptor than donor emission peak, field enhancement from 61nm Au nanodisks alone could qualitatively produce the trend of peak ratio observed in figure 6.2a. Another possible mechanism at work to explain the order of increase in peak ratio is the enhancement of FRET from donors to acceptors by Au nanodisks. As seen in figure 6.1,

the broad surface plasmon peak of 61 nm Au nanodisks has good spectral overlap with both donor and acceptor emission and therefore could play the role of assisting energy transfer between donors and acceptors. Time resolved PL measurement can provide further understanding on the nature of the plasmonic influence of Au nanodisks on $QD_{1:3}$.

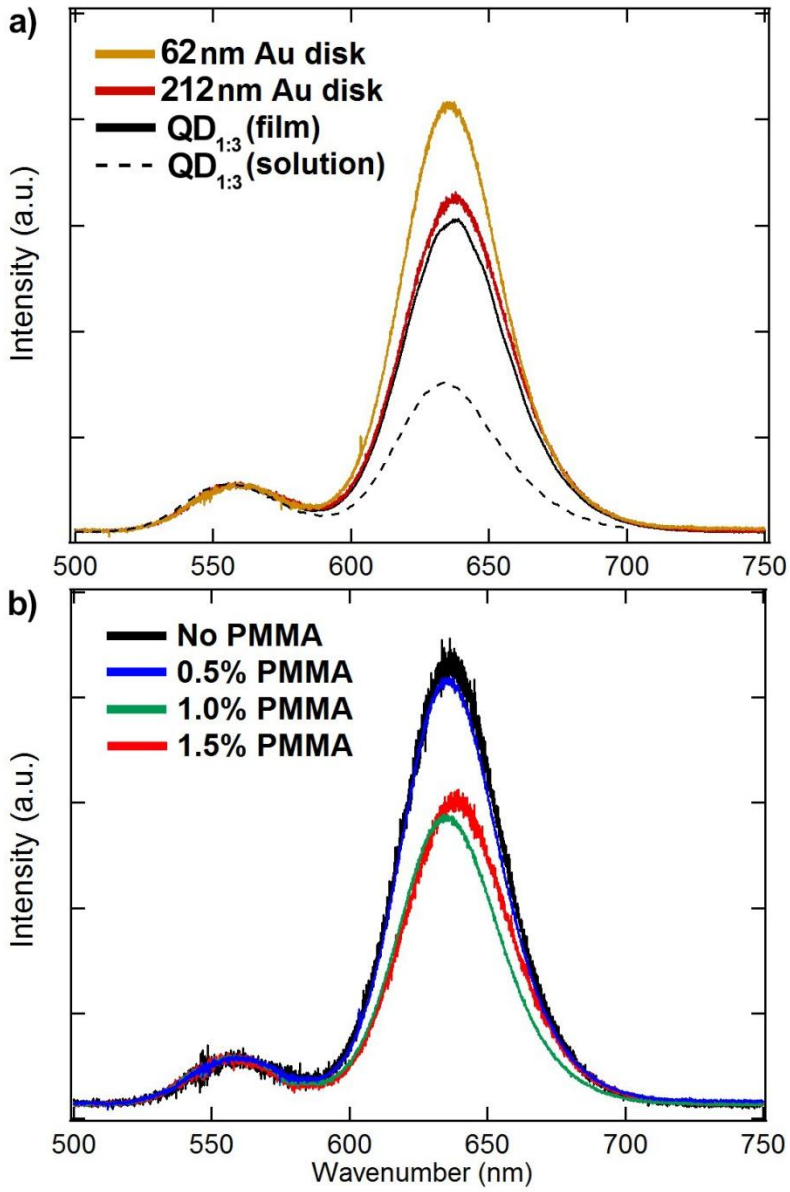

Figure 6.2 a) Steady state PL intensity of $QD_{1:3}$ mixed clusters in film (solid black), $QD_{1:3}$ mixed in solution (dotted black), 61 nm (yellow) and 212 nm (red) Au nanodisks. b) Steady state PL intensity of $QD_{1:3}$ mixed sample without PMMA (black), 0.5% PMMA (blue), 1.0% PMMA (green), and 1.5% PMMA (red). All curves are normalized with respect to the donor emission peak to better visualize donor to acceptor peak ratio.

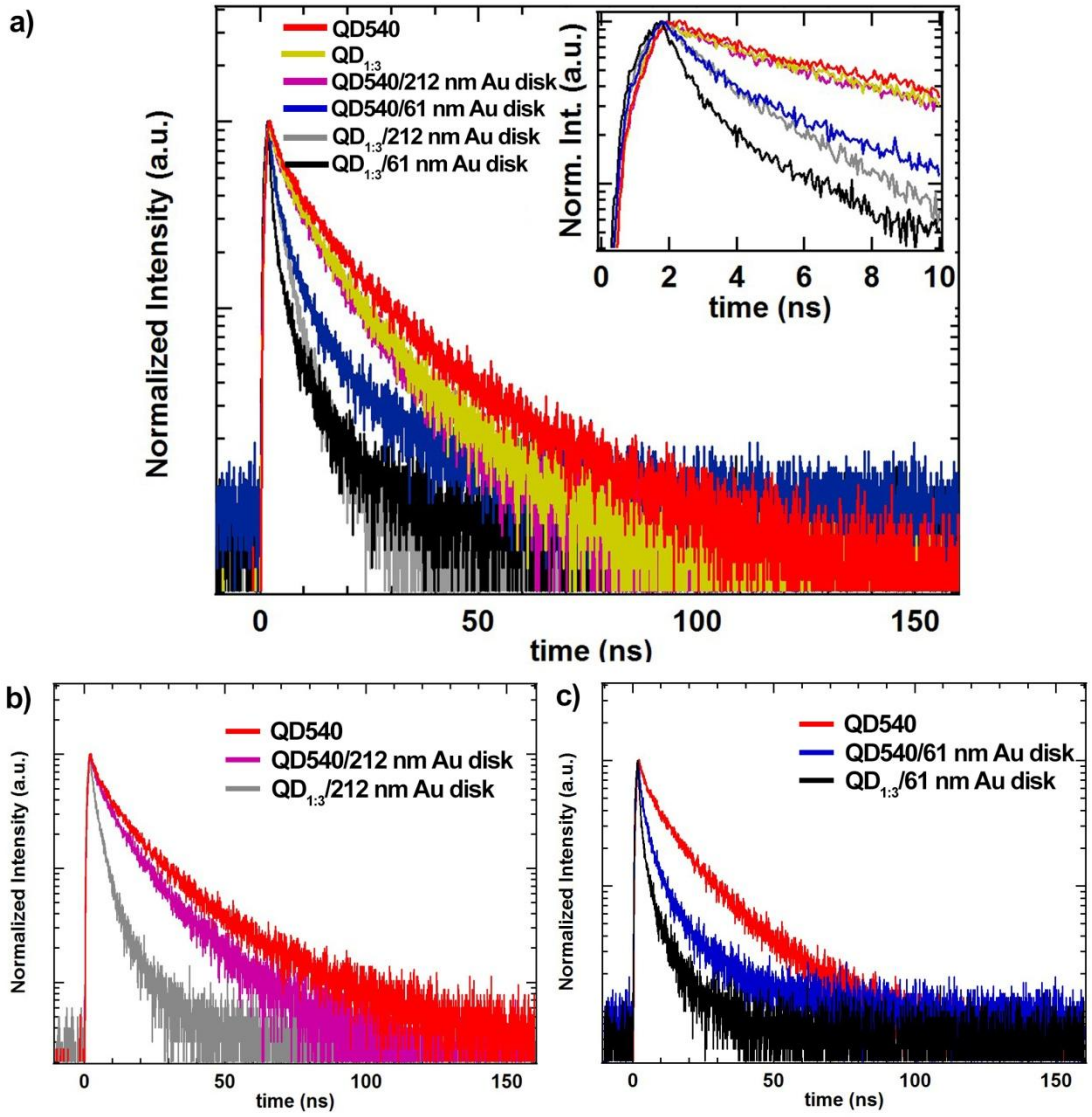

Figure 6.3 a) PL decay curves measured at emission maximum of QD540. Listed from longest to shortest lifetime: QD540 only, $QD_{1:3}$ only, QD540 with 212 nm Au disk, QD540 with 61 nm Au disks, $QD_{1:3}$ with 212 nm Au disks, and $QD_{1:3}$ with 61 nm Au disks. Inset shows the first 10 ns of the decay curves. b) PL decay curves showing the influence on donor lifetime from surface plasmon of 212 nm Au disks only (purple) and surface plasmon with acceptor (gray). c) PL decay curves showing the influence on donor lifetime from surface plasmon of 61 nm Au nanodisks only (blue) and surface plasmon with acceptor (black).

Figure 6.3a shows the decay curves collected at donor emission maximum for samples of QD540 only, QD540 coupled with 212 nm and 61 nm Au nanodisks, as well as samples of $QD_{1:3}$ only, and $QD_{1:3}$ coupled with 212 nm and 61 nm Au nanodisks. The QD only samples have distinctly slower decay than the Au nanodisks samples, except for QD540 with 212 nm Au nanodisks, which is comparable to decay of $QD_{1:3}$. This observation suggests that energy transfer between donors and acceptors is slower than energy transfer from QDs to Au nanodisks when surface plasmon and QD emission have good overlap. Inset from figure 6.3a shows the first 10 ns of the decay curves and highlights the fast component of the decay. The decay curves of QD540 (red) and $QD_{1:3}$ (yellow) are fairly similar in the first 10ns, suggesting that the more dominant process in the faster time scale is energy transfer from QDs to Au nanodisks. The decay curves of QD540 only and QD540 with 212 nm (purple) Au disks are also similar in the first 10 ns, while the decay curve of QD540 with 61 nm Au disks (blue) shows significant reduction in lifetime in the first 10 ns. This suggests that greater spectral overlap between surface plasmon and emission peak leads to more decrease in PL lifetime. This same relationship between spectral overlap and lifetime reduction is also demonstrated by $QD_{1:3}$ samples with 212 nm (gray) and 61 nm (black) Au nanodisks. However, with $QD_{1:3}$ in the presence of surface plasmon, the situation is more complicated since energy transfer is coupled between donor, acceptor and Au nanodisks.

A comparison of the decay curves in figure 6.3b of QD540 (red), QD540 with 212 nm Au disks (purple) and $QD_{1:3}$ with 212 nm Au disks (gray) shows that surface plasmons can enhance FRET between donors/acceptors and can lead to significant

lifetime reduction apart from the intrinsic plasmonic quenching effect between Au nanodisks and QDs. Comparing the red and purple decay curves in figure 6.3b, the presence of 212 nm Au nanodisks with QD540 does not lead to significant reduction in donor lifetime compared with QD540 only samples. This is attributed to poor overlap between surface plasmons from 212 nm Au nanodisks and the emission peaks of donor. However, the reduction in donor lifetime becomes very significant when acceptors are also present with 212 nm Au nanodisks and donor, as seen in the dramatic decrease in lifetime of $QD_{1:3}$ with 212 nm Au disks (gray) in figure 6.3b. This same trend is also observed with 61 nm Au nanodisks, as shown in figure 6.3c. The donor lifetime further deceases when acceptors are present, evidenced by the decay curves of QD540 with 61 nm Au disks (blue) and $QD_{1:3}$ with 61 nm Au disks (black).

Table 6.1 shows the weighted lifetimes of QD540 with and without FRET and plasmonic influence from 61 nm Au nanodisks. The quenching efficiency, Q_{LT}, is given as [64]

$$Q_{LT} = 1 - \frac{\tau_{Au}}{\tau_{QD}}$$

where $\tau_{QD}$and τ_{Au} are average lifetimes of sample with QD only and same sample with Au respectively.

With just QD540, the presence of 61 nm Au nanodisks leads to a quenching efficiency of 0.5. The quenching efficiency is 0.7 for $QD_{1:3}$ when coupled with 61 nm Au nanodisks. This quenching efficiency takes into account only the plasmonic effect as $QD_{1:3}$ with 61nm Au disks sample is compared with $QD_{1:3}$ only sample. This shows that

the presence of plasmonic nanodisks not only contributes to non-radiative energy transfer from QD540 to Au nanodisks, but also assists the FRET process (LSPR-FRET) between QD540 and QD620, leading to a higher Q_{LT}. Tables 6.2 shows Förster resonance energy transfer rate (k_{FRET}) and Förster radius (R_o) calculated based on FRET model with dipole-dipole approximation using the measured lifetimes.[66] The equations used for calculating k_{FRET} and R_o are:

$$k_{FRET} = \frac{1}{\tau_{DA}} - \frac{1}{\tau_D}$$

$$R_o = \sqrt[6]{\frac{2d^4\tau_D k_{FRET}}{C_{acc}\pi}}$$

where k_{FRET} is Förster resonance energy transfer rate, τ_{DA} and $\tau_D$are decay lifetime of $QD_{1:3}$ and QD540 samples respectively. $R_o, d,$ and C_{acc} are the Förster radius, center to center separation between donor/acceptor and concentration of acceptor QD per unit area respectively. Despite having the shortest lifetime from all samples, $QD_{1:3}$ with 61 nm Au disks sample shows smaller k_{FRET} and R_o than $QD_{1:3}$ with 212 nm Au disks. This observation can be explained by considering the relative contribution of intrinsic plasmonic effect and LSPR-FRET for $QD_{1:3}$ with 212 nm Au disks and $QD_{1:3}$ with 61 nm Au disks. Due to a better spectral overlap between surface plasmon of 61 nm Au disks and donor than surface plasmon of 212 nm Au disks, the intrinsic plasmonic effect is expected to be stronger for $QD_{1:3}$ with 61 nm Au disks. This intrinsic plasmonic effect contributes more in quenching the PL lifetime than LSPR-FRET for $QD_{1:3}$ with 61 nm Au disks compared to $QD_{1:3}$ with 212 nm Au disks. This explanation based on the

relative contribution of intrinsic plasmonic effect and LSPR-FRET is also consistent with the steady state PL intensities shown in figure 6.2a. $QD_{1:3}$ with 61 nm Au disks, having higher contribution from plasmonic effect than LSPR-FRET, shows a higher emission peak ratio than $QD_{1:3}$ with 212 nm Au disks due to stronger plasmonic field enhancement. It is important to note that the values of k_{FRET} and R_o calculated are based on a simple dipole-dipole approximation model, which may not be an accurate model for the system under investigation due to the coupling between surface plasmon, donor, and acceptor QDs. A more detailed model would be required to verify the trends observed in this study.

	QD540 only	$QD_{1:3}$	QD540 with 61 nm Au nanodisk	$QD_{1:3}$ with 61 nm Au nanodisks
weighted τ (ns)	**18.7**	**13.7**	**9.1**	**4.3**
quenching efficiency (Q_{LT})			**0.5**	**0.7**

Table 6.1 Weighted PL lifetimes and calculated quenching efficiency from 3-exponential decay fitting for QD540 (donor) under FRET and plasmonic influence from 61 nm Au nanodisk

	$QD_{1:3}$ only	$QD_{1:3}$ with 61 nm Au nanodisks	$QD_{1:3}$ with 212 nm Au nanodisks
$k_{FRET}(s^{-1})$	**$2.0x10^7$**	**$1.2x10^8$**	**$1.8x10^8$**
R_o (nm)	**10.2**	**12.3**	**13.9**

Table 6.2 Förster resonance energy transfer rate (k_{FRET}) and Förster radius (R_o) calculated based on FRET model with measured lifetimes.

6.2.4 Dependence of LSPR coupled FRET on separation distance

A separation dependence study of plasmonic effects on peak area ratio and lifetime was also conducted with tunable PMMA separation layer. Figure 6.2b shows the steady state PL spectra of $QD_{1:3}$ samples with 61 nm Au nanodisks, with a range of separation distance indicated by the concentration of PMMA used as spacer layer. Sample without PMMA spacer layer is expected to have the smallest peak area ratio since quenching effect should dominate when QDs are in direct contact with Au. However, sample with no PMMA has the highest peak area ratio compared to other samples with PMMA spacer layer. A closer examination at the structure of the Au layer deposited without PMMA spacer reveals that it has a very different interface than Au layer deposited on PMMA. Figure 6.4 shows the cross section of Au film deposited directly on PS-b-PMMA layer. Au deposited on samples with PMMA layer adopted the shape of the underlying layer and the resulting Au layer is flat. However, Au deposited on PS-b-PMMA template adopted the shape of the PS-b-PMMA template and formed a honeycomb like layer. The difference in structure makes the sample without PMMA layer not suitable to include in the separation distance dependence study with other samples with PMMA spacer layer, but it could explain why sample without PMMA has the highest peak area ratio.

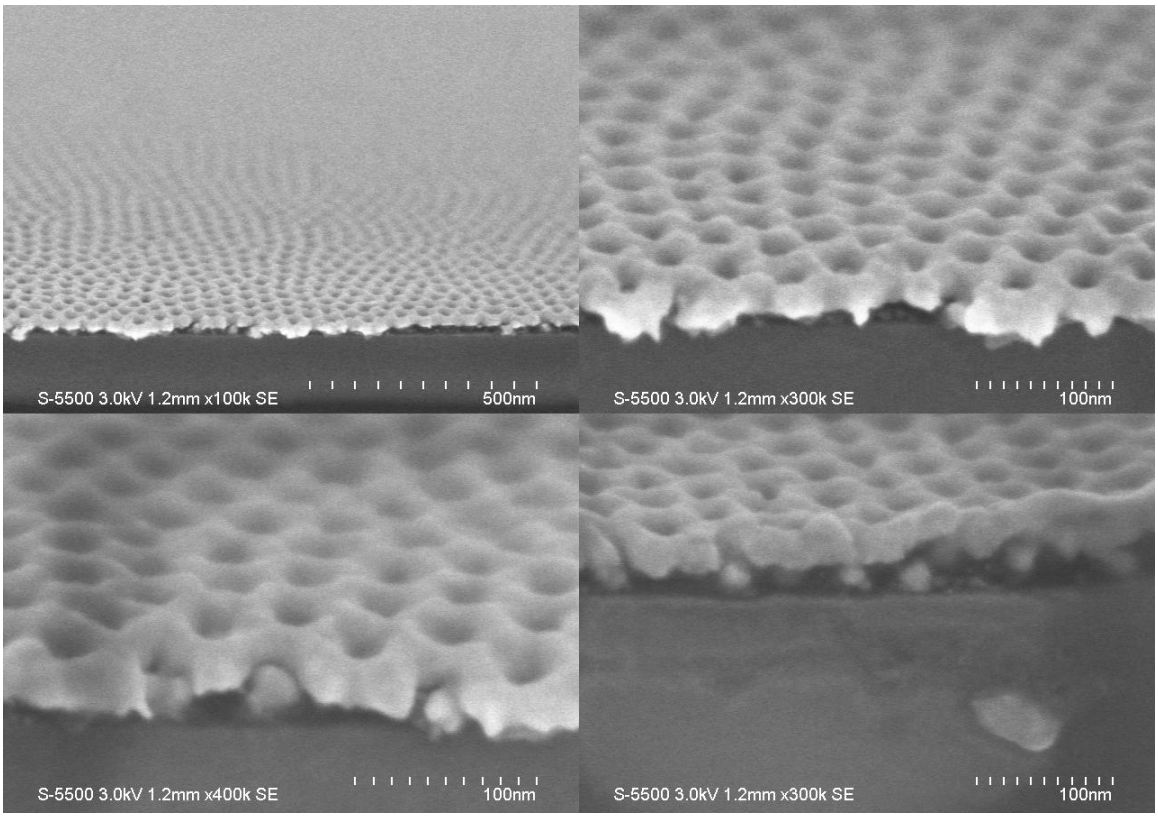

Figure 6.4 Cross sections of 20nm Au film deposited directly on PSPMMA template without PMMA spacer layer. Au nanoparticles can be seen deposited within the holes from the PSPMMA templates.

From figure 6.2b, the samples with PMMA show the general trend that the shortest separation (0.5% PMMA) leads to the highest peak area ratio. This is consistent with the understanding of plasmonic influence that at larger separation distance the effect of field enhancement would decrease. Comparison with lifetime data in figure 6.5 shows a consistent trend that surface plasmon coupling with QD clusters decreases with increasing distance. The lifetime is the shortest with 0.5% PMMA spacer layer and then increases with thicker PMMA layers.

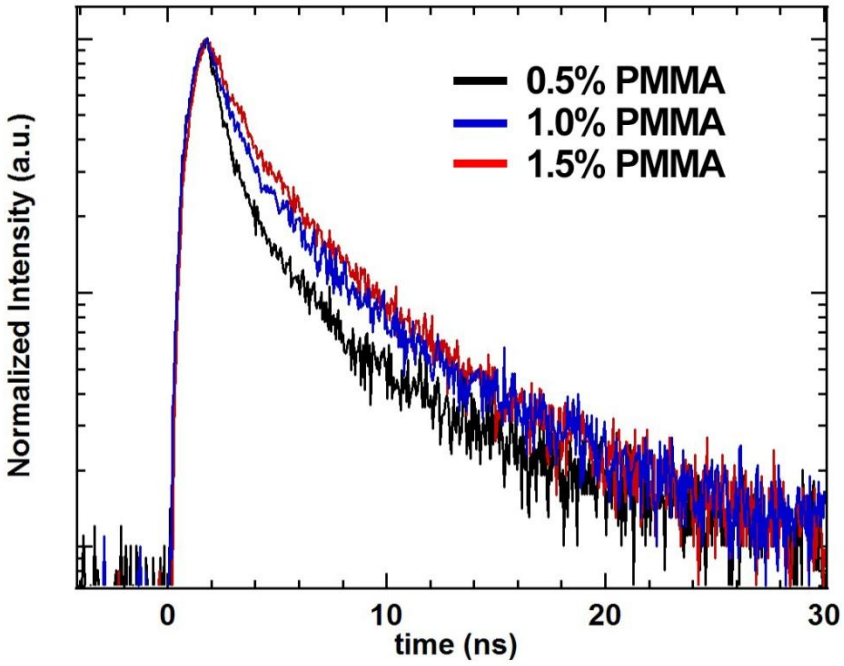

Figure 6.5 PL decay curves of $QD_{1:3}$ covered by 61 nm Au nanodisks, with 0.5% PMMA layer, 1.0% PMMA, and 1.5% PMMA separation layer.

The novel fabrication technique developed in this study leads to a uniform and well-characterized array of QD clusters coupled with Au plasmonic nanodisks. It was concluded that strong spectral overlap between the plasmon peak and the donor and acceptor emission peaks leads to a significant enhancement in acceptor emission and decrease in PL lifetime of the donor, far more than enhancement in acceptor emission and decrease in donor lifetime resulting from FRET alone. The role of surface plasmon in enhancing FRET between donor and acceptor QDs was demonstrated. As a result the lifetime of $QD_{1:3}$ is sensitive to changes to the coupling strength between surface plasmon and QD emission. Using the same system fabricated here, one potential application to utilize such coupling between surface plasmon and FRET is to construct an array of

lifetime-based biosensors that is sensitive to changes in dielectric constant when different molecules adsorb on the surface of Au nanodisks. The platform fabricated in this study can be adapted to study the coupling between other plasmonic structures or quantum emitters and assemble plasmonic/donor/acceptor units in a large array. This opens up many possibilities to develop more surface plasmon based applications.

Chapter 7: Conclusion and future work

7.1 Conclusion

Two advances in nanofabrication are discussed in details in this dissertation. The first advance is developing wafer scale assembly of quantum dot clusters using commercially available block copolymer template, PS-b-PMMA and capillary force assembly. The PS-b-PMMA template is especially advantageous for assembling small nanoparticles (i.e. 5 nm) into small clusters. By fine-tuning the diameter to depth aspect ratio of the holes on template with oxygen plasma etching, a PS-b-PMMA can be tuned to assemble particles of different sizes and achieve complete hole filling with the proper particle concentration in solution and substrate withdrawal speed from solution.

Template assembly of QDs into small clusters provides an ideal system to study the red shift of 1st exciton absorption of PbSe QDs after the long insulating ligands on QD are exchanged with shorter ligands. Previous studies have centered on the ligand exchange of a QD film deposited on a substrate. Using a system of large PbSe QDs embedded in a matrix of small PbSe QDs, it is concluded that electronic coupling only accounts for ~12% of the red shift of 1st exciton absorption. Majority of the red-shift is attributed to an anomaly large polarization effect. Using the PS-b-PMMA template, small clusters of PbSe QDs are formed within the holes of the template and a ligand exchange is done to investigate the degree of red-shift of PbSe QD clusters. Unexpectedly, the red-shift is stronger for QD clusters, which is opposite of what is expected from polarization effects. It is established that a local effect has caused the red-shift of 1st exciton

absorption of QD and the localized coupling between PbSe QDs is the basis to describe these coupled QD clusters as QD molecules.

Building upon the system of QD molecules assembled in PS-b-PMMA template, Förster resonance energy transfer (FRET) between QDs are studied and metal nanostructures are introduced to enhance interaction between QDs. Förster resonance energy transfer (FRET) is a well known process in which excited QDs with higher exciton energy non-radiatively transfer that energy to QDs with lower exciton energy. The template assembly can generate an array of donor-acceptor clusters, and the second advance in fabrication is the development of a technique that creates plasmonic nanodisks on donor-acceptor clusters while simultaneously eliminating clusters not directly coupled to the nanodisks. The fabrication technique developed in this study relies on polystyrene (PS) nanospheres as Argon reactive ion etching mask. This fabrication of plasmonic nanodisks is combined with template assembly of QD clusters to create a surface plasmon coupled FRET system involving donor and acceptor quantum dots. The degree of coupling between surface plasmon with the FRET process is studied by varying the spectral position of the surface plasmon peak and the separation distance between plasmonic nanodisks and QD clusters. It is demonstrated that the PL lifetime of donor QD decreases dramatically when both acceptor and plasmonic nanodisk are coupled to donor, which is not the case when only plasmonic nanodisk or only acceptor is coupled to the donor. The lifetime study demonstrates the role of surface plasmon in enhancing energy transfer between donor-acceptor clusters, especially for donor-acceptor pair that does not display strong degree of FRET.

7.2 Future Work

Only single layer plasmonic nanodisks are studied here but the fabrication technique can be easily adapted to create double layer nanodisks with different noble metals. More complex nanostructures can also be fabricated by using other kinds of etching masks (i.e. nanowires) beyond just nanospheres.

The sensitivity of donor lifetime to the degree of coupling between surface plasmon and QD clusters suggests that donor lifetime can be used as a sensing response to the surrounding environment. Since surface plasmon peak is sensitive to the dielectric environment surrounding the plasmonic structure, adsorption of molecules can alter the surface plasmon resonance, which in turn will affect the lifetime of donor. An array of plasmonic nanodisks/QD clusters functionalized with bio-moieties can potentially become a highly sensitive and tunable bio assay for biomoleucles detection. Surface plasmon resonance (SPR) spectroscopy is a well-developed technique to measure adsorption of molecules on a surface coupled with propagating surface plasmon from gold film.[129] Adsorption of molecules change the refractive index at the interface and the change in refractive index translates to a change in the coupling between surface plasmon and an incident light beam. Instead of an incident light beam, the lifetime based sensing involves the coupling between surface plasmon and QDs, which could prove to be a sensitive technique for biosensing.

References

[1] A. M. Smith, S. Nie, *Acc. Chem. Res.* **2009**, *43*, 190.

[2] C. B. Murray, D. J. Norris, M. G. Bawendi, *J. Am. Chem. Soc.* **1993**, *115*, 8706.

[3] S. Pokrant, K. B. Whaley, *Eur. Phys. J. D - At. Mol. Opt. Phys.* **1999**, *6*, 255.

[4] M. a. Hines, P. Guyot-Sionnest, *J. Phys. Chem.* **1996**, *100*, 468.

[5] B. O. Dabbousi, J. Rodriguez-Viejo, F. V Mikulec, J. R. Heine, H. Mattoussi, R. Ober, K. F. Jensen, M. G. Bawendi, *J. Phys. Chem. B* **1997**, *101*, 9463.

[6] S. Link, M. a El-Sayed, *Annu. Rev. Phys. Chem.* **2003**, *54*, 331.

[7] G. Mie, *Ann. Phys.* **1908**, *25*, 377.

[8] P. K. Jain, X. Huang, I. H. El-Sayed, M. a. El-Sayed, *Plasmonics* **2007**, *2*, 107.

[9] G. W. Bryant, F. J. Garcı, J. Aizpurua, P. Hanarp, D. S. Sutherland, M. Ka, *Phys. Rev. Lett.* **2003**, *90*, 057401.

[10] P. Hanarp, M. Käll, D. S. Sutherland, *J. Phys. Chem. B* **2003**, *107*, 5768.

[11] M. Hu, C. Novo, A. Funston, H. Wang, H. Staleva, S. Zou, P. Mulvaney, Y. Xia, G. V Hartland, *J. Mater. Chem.* **2008**, *18*, 1949.

[12] X. Michalet, F. F. Pinaud, L. a Bentolila, J. M. Tsay, S. Doose, J. J. Li, G. Sundaresan, a M. Wu, S. S. Gambhir, S. Weiss, *Science* **2005**, *307*, 538.

[13] X. Gao, Y. Cui, R. M. Levenson, L. W. K. Chung, S. Nie, *Nat Biotech* **2004**, *22*, 969.

[14] N. Hildebrandt, L. J. Charbonnière, H.-G. Löhmannsröben, *J. Biomed. Biotechnol.* **2007**, *2007*, 79169.

[15] I. L. Medintz, A. R. Clapp, H. Mattoussi, E. R. Goldman, B. Fisher, J. M. Mauro, *Nat. Mater.* **2003**, *2*, 630.

[16] U. O. S. Seker, T. Ozel, H. V. Demir, *Nano Lett.* **2011**, *11*, 1530.

[17] C. Sönnichsen, T. Franzl, T. Wilk, G. von Plessen, J. Feldmann, *Phys. Rev. Lett.* **2002**, *88*, 077402.

[18] I. H. El-Sayed, X. Huang, M. a El-Sayed, *Nano Lett.* **2005**, *5*, 829.

[19] L. R. Hirsch, R. J. Stafford, J. a Bankson, S. R. Sershen, B. Rivera, R. E. Price, J. D. Hazle, N. J. Halas, J. L. West, *Proc. Natl. Acad. Sci. U. S. A.* **2003**, *100*, 13549.

[20] A. J. Haes, R. P. Van Duyne, *J. Am. Chem. Soc.* **2002**, *124*, 10596.

[21] J. Hulteen, R. Van Duyne, *J. Vac. Sci. Technol. A* **1995**, *13*, 1553.

[22] K. Bosnick, M. Maillard, L. Brus, *J. Phys. Chem. B* **2003**, *107*, 9964.

[23] S. L. Kleinman, E. Ringe, N. Valley, K. L. Wustholz, E. Phillips, K. a Scheidt, G. C. Schatz, R. P. Van Duyne, *J. Am. Chem. Soc.* **2011**, *133*, 4115.

[24] H. Xu, *Appl. Phys. Lett.* **2004**, *85*, 5980.

[25] E. Jang, S. Jun, H. Jang, J. Lim, B. Kim, Y. Kim, *Adv. Mater.* **2010**, *22*, 3076.

[26] T.-H. Kim, K.-S. Cho, E. K. Lee, S. J. Lee, J. Chae, J. W. Kim, D. H. Kim, J.-Y. Kwon, G. Amaratunga, S. Y. Lee, B. L. Choi, Y. Kuk, J. M. Kim, K. Kim, *Nat Phot.* **2011**, *5*, 176.

[27] Y. Liu, M. Gibbs, J. Puthussery, S. Gaik, R. Ihly, H. W. Hillhouse, M. Law, *Nano Lett.* **2010**, *10*, 1960.

[28] M. Law, J. M. Luther, Q. Song, B. K. Hughes, C. L. Perkins, A. J. Nozik, *J. Am. Chem. Soc.* **2008**, *130*, 5974.

[29] W. Shockley, H. J. Queisser, *J. Appl. Phys.* **1961**, *32*, 510.

[30] P. Kamat, *J. Phys. Chem. Lett.* **2013**, *4*, 908.

[31] R. J. Ellingson, M. C. Beard, J. C. Johnson, P. Yu, O. I. Micic, A. J. Nozik, A. Shabaev, A. L. Efros, *Nano Lett.* **2005**, *5*, 865.

[32] C. B. Murray, S. Sun, W. Gaschler, H. Doyle, T. A. Betley, C. R. Kagan, *IBM J. Res. Dev.* **2001**, *45*, 47.

[33] J. Turkevich, P. C. Stevenson, J. Hillier, *Discuss. Faraday Soc.* **1951**, *11*, 55.

[34] T. Yonezawa, T. Kunitake, *Colloids Surfaces A Physicochem. Eng. Asp.* **1999**, *149*, 193.

[35] M. Brust, M. Walker, D. Bethell, D. J. Schiffrin, R. Whyman, *J. Chem. Soc., Chem. Commun.* **1994**, 801.

[36] A. Lattes, I. Rico, A. de Savignac, A. A.-Z. Samii, *Tetrahedron* **1987**, *43*, 1725.

[37] F. Chen, G.-Q. Xu, T. S. A. Hor, *Mater. Lett.* **2003**, *57*, 3282.

[38] B.-H. Sohn, J.-M. Choi, S. Il Yoo, S.-H. Yun, W.-C. Zin, J. C. Jung, M. Kanehara, T. Hirata, T. Teranishi, *J. Am. Chem. Soc.* **2003**, *125*, 6368.

[39] K. N. Thakkar, S. S. Mhatre, R. Y. Parikh, *Nanomedicine* **2010**, *6*, 257.

[40] J. C. Hulteen, C. R. Martin, *J. Mater. Chem.* **1997**, *7*, 1075.

[41] M. J. Banholzer, L. Qin, J. E. Millstone, K. D. Osberg, C. a Mirkin, *Nat. Protoc.* **2009**, *4*, 838.

[42] K. B. Blodgett, I. Langmuir, *Phys. Rev.* **1937**, *51*, 964.

[43] B. O. Dabbousi, C. B. Murray, M. F. Rubner, M. G. Bawendi, *Chem. Mater.* **1994**, *6*, 216.

[44] J. M. Luther, M. Law, Q. Song, C. L. Perkins, M. C. Beard, A. J. Nozik, *ACS Nano* **2008**, *2*, 271.

[45] C. B. Murray, C. R. Kagan, M. G. Bawendi, *Science (80-.).* **1995**, *270*, 1335.

[46] A. M. Kalsin, M. Fialkowski, M. Paszewski, S. K. Smoukov, K. J. M. Bishop, B. A. Grzybowski, *Science (80-.).* **2006**, *312*, 420.

[47] E. V Shevchenko, D. V Talapin, S. O'Brien, C. B. Murray, *J. Am. Chem. Soc.* **2005**, *127*, 8741.

[48] D. V Talapin, E. V Shevchenko, M. I. Bodnarchuk, X. Ye, J. Chen, C. B. Murray, *Nature* **2009**, *461*, 964.

[49] C. L. Choi, A. P. Alivisatos, *Annu. Rev. Phys. Chem.* **2010**, *61*, 369.

[50] L. Manna, E. C. Scher, A. P. Alivisatos, *J. Am. Chem. Soc.* **2000**, *122*, 12700.

[51] D. J. Milliron, S. M. Hughes, Y. Cui, L. Manna, J. Li, L.-W. Wang, A. Paul Alivisatos, *Nature* **2004**, *430*, 190.

[52] M. R. Buck, J. F. Bondi, R. E. Schaak, *Nat Chem* **2012**, *4*, 37.

[53] C. L. Choi, H. Li, A. C. K. Olson, P. K. Jain, S. Sivasankar, A. P. Alivisatos, *Nano Lett.* **2011**, *11*, 2358.

[54] Y. Cui, M. T. Björk, J. A. Liddle, C. Sönnichsen, B. Boussert, A. P. Alivisatos, *Nano Lett.* **2004**, *4*, 1093.

[55] H. Kitano, S. Akasaka, T. Inoue, F. Chen, M. Takenaka, H. Hasegawa, H. Yoshida, H. Nagano, *Langmuir* **2007**, *23*, 6404.

[56] K. W. Guarini, C. T. Black, S. H. I. Yeung, *Adv. Mater.* **2002**, *14*, 1290.

[57] S. Ham, C. Shin, E. Kim, D. Y. Ryu, U. Jeong, T. P. Russell, C. J. Hawker, *Macromolecules* **2008**, *41*, 6431.

[58] T. Thurn-Albrecht, R. Steiner, J. DeRouchey, C. M. Stafford, E. Huang, M. Bal, M. Tuominen, C. J. Hawker, T. P. Russell, *Adv. Mater.* **2000**, *12*, 787.

[59] T. Xu, H.-C. Kim, J. DeRouchey, C. Seney, C. Levesque, P. Martin, C. M. Stafford, T. P. Russell, *Polymer.* **2001**, *42*, 9091.

[60] M. J. Misner, H. Skaff, T. Emrick, T. P. Russell, *Adv. Mater.* **2003**, *15*, 221.

[61] J. P. Camden, J. a Dieringer, Y. Wang, D. J. Masiello, L. D. Marks, G. C. Schatz, R. P. Van Duyne, *J. Am. Chem. Soc.* **2008**, *130*, 12616.

[62] E. Purcell, *Phys. Rev.* **1946**, *69*, 674.

[63] V. K. Komarala, Y. P. Rakovich, A. L. Bradley, S. J. Byrne, Y. K. Gun'ko, N. Gaponik, A. Eychmüller, *Appl. Phys. Lett.* **2006**, *89*.

[64] X. Zhang, C. A. Marocico, M. Lunz, V. A. Gerard, Y. K. Gun, V. Lesnyak, N. Gaponik, A. S. Susha, A. L. Rogach, A. L. Bradley, *ACS Nano,* **2012**, *6*, 9283.

[65] D. Ratchford, F. Sha, S. Kim, S. K. Gray, X. Li, *Nano Lett.* **2011**, 1049.

[66] M. Lunz, V. A. Gerard, Y. K. Gun'ko, V. Lesnyak, N. Gaponik, A. S. Susha, A. L. Rogach, A. L. Bradley, *Nano Lett.* **2011**, *11*, 3341.

[67] X.-R. Su, W. Zhang, L. Zhou, X.-N. Peng, Q.-Q. Wang, *Opt. Express* **2010**, *18*, 6516.

[68] T. Ozel, P. L. Hernandez Martinez, E. Mutlugun, O. Akin, S. Nizamoglu, I. O. Ozel, Q. Zhang, Q. Xiong, H. V. Demir, *Nano Lett.* **2013**, *13*, 3065.

[69] X. Zhang, C. a Marocico, M. Lunz, V. a Gerard, Y. K. Gun'ko, V. Lesnyak, N. Gaponik, A. S. Susha, A. L. Rogach, a L. Bradley, *ACS Nano* **2014**, *8*, 1273.

[70] G. Binnig, C. F. Quate, C. Gerber, *Phys. Rev. Lett.* **1986**, *56*, 930.

[71] D. Johnson, N. Hilal, W. R. Bowen, in *At. Force Microsc. Process Eng.* (Eds.: W.R. Bowen, N. Hilal), Elsevier Ltd, **2009**, pp. 1–24.

[72] R. Bennewitz, *Mater. Today* **2005**, *8*, 42.

[73] B. D. Terris, *J. Vac. Sci. Technol. A Vacuum, Surfaces, Film.* **1990**, *8*, 374.

[74] U. Hartmann, *Annu. Rev. Mater. Sci.* **1999**, *29*, 53.

[75] M. Nonnenmacher, M. P. O'Boyle, H. K. Wickramasinghe, *Appl. Phys. Lett.* **1991**, *58*, 2921.

[76] J. Goldstein, D. E. Newbury, D. C. Joy, C. E. Lyman, P. Echlin, E. LIfshin, L. Sawyer, J. R. Michael., *Scanning Electron Microscopy and X-Ray Microanalysis*, Springer New York, New York, **2003**.

[77] I. W. Levin, R. Bhargava, *Annu. Rev. Phys. Chem.* **2005**, *56*, 429.

[78] M. Shearn, X. Sun, M. D. Henry, A. Yariv, A. Scherer, in *Semicond. Technol.* (Ed.: J. Grym), InTech, **2010**, pp. 79–104.

[79] A. J. Alpert, *J. Chromatogr. A* **1990**, *499*, 177.

[80] R. D. Deegan, O. Bakajin, T. F. Dupont, G. Huber, S. R. Nagel, T. A. Witten, *Nature* **1997**, *389*, 827.

[81] P. Mansky, Y. Liu, E. Huang, T. P. Russell, C. Hawker, *Science (80-.).* **1997**, *275*, 1458.

[82] S. H. Kim, M. J. Misner, T. P. Russell, *Adv. Mater.* **2008**, *20*, 4851.

[83] E. Huang, L. Rockford, T. P. Russell, C. J. Hawker, *Nature* **1998**, *395*, 757.

[84] M. J. Gordon, D. Peyrade, *Appl. Phys. Lett.* **2006**, *89*, 53112.

[85] L. Malaquin, T. Kraus, H. Schmid, E. Delamarche, H. Wolf, *Langmuir* **2007**, *23*, 11513.

[86] T. Kraus, L. Malaquin, H. Schmid, W. Riess, N. D. Spencer, H. Wolf, *Nat Nano* **2007**, *2*, 570.

[87] C. Kuemin, R. Stutz, N. D. Spencer, H. Wolf, *Langmuir* **2011**, *27*, 6305.

[88] K. W. Lei, T. West, X.-Y. Zhu, *J. Phys. Chem. B* **2013**, *117*, 4582.

[89] S. W. Hong, J. Xia, M. Byun, Q. Zou, Z. Lin, *Macromolecules* **2007**, *40*, 2831.

[90] N. Ueno, S. Konishi, K. Tanimoto, K. Sugita, *Jpn. J. Appl. Phys.* **1981**, *20*, L709.

[91] S. Asakura, A. Hozumi, A. Fuwa, *J. Vac. Sci. Technol. A* **2005**, *23*, 1137.

[92] S. C. Clear, P. F. Nealey, *J. Colloid Interface Sci.* **1999**, *213*, 238.

[93] Y.-H. Ting, S.-M. Park, C.-C. Liu, X. Liu, F. J. Himpsel, P. F. Nealey, A. E. Wendt, *J. Vac. Sci. Technol. B* **2008**, *26*, 1684.

[94] L. Lianos, D. Parrat, T. Q. Hoc, T. M. Duc, *J. Vac. Sci. Technol. A* **1994**, *12*, 2491.

[95] M. Wang, M. Zhang, C. Siegers, G. D. Scholes, M. A. Winnik, *Langmuir* **2009**, *25*, 13703.

[96] K. R. Williams, K. Gupta, M. Wasilik, *Microelectromechanical Syst. J.* **2003**, *12*, 761.

[97] F. Iacona, G. Ceriola, F. La Via, *Mater. Sci. Semicond. Process.* **2001**, *4*, 43.

[98] D. V Talapin, C. B. Murray, *Science (80-.).* **2005**, *310*, 86.

[99] K. J. Williams, W. A. Tisdale, K. S. Leschkies, G. Haugstad, D. J. Norris, E. S. Aydil, X. Y. Zhu, *ACS Nano* **2009**, *3*, 1532.

[100] J. J. Choi, J. Luria, B.-R. Hyun, A. C. Bartnik, L. Sun, Y.-F. Lim, J. A. Marohn, F. W. Wise, T. Hanrath, *Nano Lett.* **2010**, DOI 10.1021/nl100498e.

[101] L. E. Brus, *J. Chem. Phys.* **1984**, *80*, 4403.

[102] A. Franceschetti, H. Fu, L. W. Wang, A. Zunger, *Phys. Rev. B* **1999**, *60*, 1819.

[103] H. Mirafzal, D. F. Kelley, *J. Phys. Chem. C* **2009**, *113*, 7139.

[104] E. E. Jelly, *Nature* **1937**, *139*, 631.

[105] T. Kobayashi, Ed., *J-Aggregates*, World Scientific, Singapore, **1996**.

[106] C. A. Leatherdale, M. G. Bawendi, *Phys. Rev. B* **2001**, *63*, 165315.

[107] M. T. Frederick, E. a Weiss, *ACS Nano* **2010**, *4*, 3195.

[108] K. S. Leschkies, T. J. Beatty, M. S. Kang, D. J. Norris, E. S. Aydil, *ACS Nano* **2009**, *3*, 3638.

[109] C. R. Kagan, C. B. Murray, M. G. Bawendi, *Phys. Rev. B* **1996**, *54*, 8633.

[110] C. R. Kagan, C. B. Murray, M. Nirmal, M. G. Bawendi, *Phys. Rev. Lett.* **1996**, *76*, 1517.

[111] D. Babic, R. Tsu, R. F. Greene, *Phys. Rev. B* **1992**, *45*, 14150.

[112] G. Allan, C. Delerue, M. Lannoo, E. Martin, *Phys. Rev. B* **1995**, *52*, 11982.

[113] M. Iwamatsu, M. Fujiwara, N. Happo, K. Horii, *J. Phys. Condens. Matter* **1997**, *9*, 9881.

[114] J. E. Spanier, I. P. Herman, *Phys. Rev. B* **2000**, *61*, 10437.

[115] P. M. Echenique, J. B. Pendry, *J. Phys. C Solid State Phys.* **1978**, *11*, 2065.

[116] G. E. Cragg, A. L. Efros, *Nano Lett.* **2010**, *10*, 313.

[117] O. Millo, D. Katz, Y. Cao, U. Banin, *Phys. Rev. Lett.* **2001**, *86*, 5751.

[118] Y. Yin, Y. Lu, B. Gates, Y. Xia, *J. Am. Chem. Soc.* **2001**, *123*, 8718.

[119] A. Wolcott, V. Doyeux, C. A. Nelson, R. Gearba, K. W. Lei, K. G. Yager, A. D. Dolocan, K. Williams, D. Nguyen, X. Y. Zhu, *J. Phys. Chem. Lett.* **2011**, *2*, 795.

[120] X. Xu, K. Kim, H. Li, D. L. Fan, *Adv. Mater.* **2012**, *24*, 5457.

[121] M. T. Hill, Y.-S. Oei, B. Smalbrugge, Y. Zhu, T. de Vries, P. J. van Veldhoven, F. W. M. van Otten, T. J. Eijkemans, J. P. Turkiewicz, H. de Waardt, E. J. Geluk, S.-H. Kwon, Y.-H. Lee, R. Notzel, M. K. Smit, *Nat Phot.* **2007**, *1*, 589.

[122] J. Y. Suh, C. H. Kim, W. Zhou, M. D. Huntington, D. T. Co, M. R. Wasielewski, T. W. Odom, *Nano Lett.* **2012**, *12*, 5769.

[123] R. F. Oulton, V. J. Sorger, T. Zentgraf, R.-M. Ma, C. Gladden, L. Dai, G. Bartal, X. Zhang, *Nature* **2009**, *461*, 629.

[124] P. Mühlschlegel, H.-J. Eisler, O. J. F. Martin, B. Hecht, D. W. Pohl, *Science (80-.).* **2005**, *308*, 1607.

[125] D. J. Farrell, N. J. Ekins-Daukes, *Nat. Photonics* **2009**, *3*, 373.

[126] N. Cicek, S. Nizamoglu, T. Ozel, E. Mutlugun, D. U. Karatay, V. Lesnyak, T. Otto, N. Gaponik, A. Eychmüller, H. V. Demir, *Appl. Phys. Lett.* **2009**, *94*, 061105.

[127] A. Yildiz, J. N. Forkey, S. a McKinney, T. Ha, Y. E. Goldman, P. R. Selvin, *Science* **2003**, *300*, 2061.

[128] T. R. Jensen, M. D. Malinsky, C. L. Haynes, R. P. Van Duyne, *J. Phys. Chem. B* **2000**, *104*, 10549.

[129] J. Homola, *Chem. Rev.* **2008**, *108*, 462.